JPL D-11532, Rev. D

Earth Observing System

Multi-angle Imaging Spectro-Radiometer

Level 1 Georectification and Registration Algorithm Theoretical Basis

Veljko M. Jovanovic[1]
Scott A. Lewicki[1]
Michael M. Smyth[1]
Jia Zong[1]
Robert P. Korechoff[1]

[1]Jet Propulsion Laboratory, California Institute of Technology

Jet Propulsion Laboratory
California Institute of Technology

Novenber 30, 1999

JPL D-11532, Rev. D

Multi-angle Imaging SpectroRadiometer (MISR)

Level 1 Georectification and Registration Algorithm Theoretical Basis

November 30, 1999

APPROVALS:

David J. Diner

MISR Principal Investigator

Graham W. Bothwell

MISR Science Data System Manager

Approval signatures are on file with the MISR Project.
To determine the latest released version of this document, consult the MISR web site (http://www-misr.jpl.nasa.gov)

Jet Propulsion Laboratory
California Institute of Technology

1.0 INTRODUCTION

1.1 IDENTIFICATION AND PURPOSE

This Algorithm Theoretical Basis (ATB) document describes the algorithms used to generate the Multi-angle Imaging SpectroRadiometer (MISR) Level 1B2 Georectified Radiance Product (GRP). The GRP is generated routinely at the Distributed Active Archive Center (DAAC). In particular, this document identifies sources of input data, both MISR and non-MISR, which are required for geometric processing; provides the physical theory and mathematical background underlying the usage of this information in deriving parameters; describes practical considerations which must be factored into the algorithm development; and outlines a test and validation approach.

1.2 SCOPE

This document presents the theoretical basis of the MISR Level 1B2 geometric algorithms, of which there are three, that deal with the geometric tasks needed to satisfy the registration and geolocation requirements on the data for subsequent input to Level 2 science retrievals. Section 1 provides the identification, purpose, and scope for the document and lists MISR Project documents and other EOS reference documents which are relevant to the Level 1B2 algorithms. Section 2 gives an overview of the MISR experiment and instrument and of the concept of the three algorithms. The three algorithms are for terrain-projected radiance, ellipsoid-projected radiance, and geometric parameters; and sections 4, 5, and 6 respectively describe these. Section 7 describes practical considerations related to the development and implementation of the algorithms. Section 8 describes the algorithm test and validation approach. Section 9 gives a list of assumptions and limitations. Section 10 gives a list of literature references. Appendix A contains the definitions of the coordinate transformations used throughout this document.

The exact structure of the data input to this processing from Level 1B1 and the output from this processing is detailed in the MISR Data Product Description (DPD) document. The individual requirements governing the processing algorithms described in this document are derived from the MISR Instrument Science Requirements (ISR) and Data System Science Requirements (DSSR) documents.

1.3 APPLICABLE MISR DOCUMENTS

Please refer to the MISR web page (http://www-misr.jpl.nasa.gov) for the latest versions of the applicable documents.

1.3.1 Controlling Project Documents

[M-1] MISR Experiment Implementation Plan (EIP), vols. 1 and 2 (Instrument), JPL D-8796.

[M-2] MISR Experiment Implementation Plan (EIP), vols. 3 and 4 (Science, Data Processing, and Instrument Operations), JPL D-11520.

[M-3] MISR Instrument Science Requirements (ISR), JPL D-9090.

[M-4] MISR Instrument Functional and Design Requirements (IFDR), JPL D-9988.

[M-5] MISR Data System Science Requirements (DSSR), JPL D-11398.

[M-6] MISR Data Product Description (DPD), JPL D-11103.

1.3.2 Reference Project Documents

[M-7] MISR Level 1 Radiance Scaling and Conditioning Algorithm Theoretical Basis: JPL D-11507.

[M-8] MISR Level 1 Ancillary Geometric Product Algorithm Theoretical Basis: JPL D-13400.

[M-9] MISR Level 1 Cloud Detection Algorithm Theoretical Basis: JPL D-13397.

[M-10] MISR Level 1 In-flight Geometric Calibration Algorithm Theoretical Basis: JPL D-13399.

[M-11] MISR Level 2 Cloud Detection and Classification Algorithm Theoretical Basis: JPL D-11399.

[M-12] MISR Level 2 Top-of-Atmosphere Albedo Algorithm Theoretical Basis: JPL D-13401.

[M-13] MISR Level 2 Aerosol Retrieval Algorithm Theoretical Basis: JPL D-11400.

[M-14] MISR Level 2 Surface Retrieval Algorithm Theoretical Basis: JPL D-11401.

[M-15] MISR Algorithm Development Plan, JPL D-11220.

[M-16] MISR Experiment Overview, JPL D-13407.

1.3.3 Other Reference Documents

[M-17] General Instrument Interface Specification (GIIS), GSFC 420-03-02, 1 Dec. 1992.

[M-18] Unique Instrument Interface Document (UIID): MISR Instrument, EOS-AM Project, GSFC 421-12-13-02.

[M-19] (PGS Toolkit Users Guide for the ECS Project, EOSDIS Core System Project, 333-CD-003-002, August 1995.

[M-20] Requirements Document for the EOS-AM Spacecraft, GSFC 421-10-01.

2.0 MISR OVERVIEW

2.1 MISR EXPERIMENT SCOPE

2.1.1 Purpose

The Multi-angle Imaging SpectroRadiometer (MISR) instrument is part of NASA's Earth Observing System (EOS). Its purpose is to study the ecology and climate of the Earth through the acquisition of systematic, global multi-angle imagery in reflected sunlight.

2.1.2 EOS AM-1 orbit characteristics

In 1998, MISR will be launched aboard the EOS AM-1 spacecraft. The baseline orbit used in defining the MISR instrument imaging capabilities has been selected by the EOS project to be sun-synchronous, with an inclination of 98.186°. The latitude of the sub-spacecraft point ranges between ±81.8°. The orbit period of 5933 sec (98.88 min) and orbit precession rate of 0.986°/day imply a ground repeat cycle of the spacecraft nadir point of exactly 16 days. This orbit is referred to as the "705-km" orbit, although the actual altitude varies from a minimum of about 704 km to a maximum of 730 km. The orbit will have an equatorial crossing time of 10:30 a.m.

2.1.3 MISR instrument characteristics

The MISR instrument consists of nine pushbroom cameras, capable of global coverage every nine days. A schematic of the EOS AM-1 orbit and the MISR instrument viewing geometry is shown in Figure 1. The cameras are arranged with one camera pointing toward the nadir (designated An), one bank of four cameras pointing in the forward direction (designated Af, Bf, Cf, and Df in order of increasing off-nadir angle), and one bank of four cameras pointing in the aftward direction (using the same convention but designated Aa, Ba, Ca, and Da). Images are acquired with nominal view angles, relative to the surface reference ellipsoid normal, of 0°, ±26.1°, ±45.6°, ±60.0°, and ±70.5° for An, Af/Aa, Bf/Ba, Cf/Ca, and Df/Da, respectively. From the EOS AM-1 orbit, it takes about 7 minutes of flight time for MISR to observe any given region at all nine view angles. Note that the instantaneous displacement in the along-track direction between the Df and Da views is about 2800 km.

Each camera uses four Charge-Coupled Device (CCD) line arrays in a single focal plane. The line arrays consist of 1504 photoactive pixels plus 16 light-shielded pixels per array, each 21 μm x 18 μm. Each line array is filtered to provide one of four MISR spectral bands. The spectral band shapes are approximately gaussian, centered at 443, 555, 670, and 865 nm, respectively. Because of the physical displacement of the four line arrays within the focal plane of each camera, there is an along-track displacement in the Earth views at the four spectral bands. This is corrected for within the Level 1B2 processing algorithm.

.

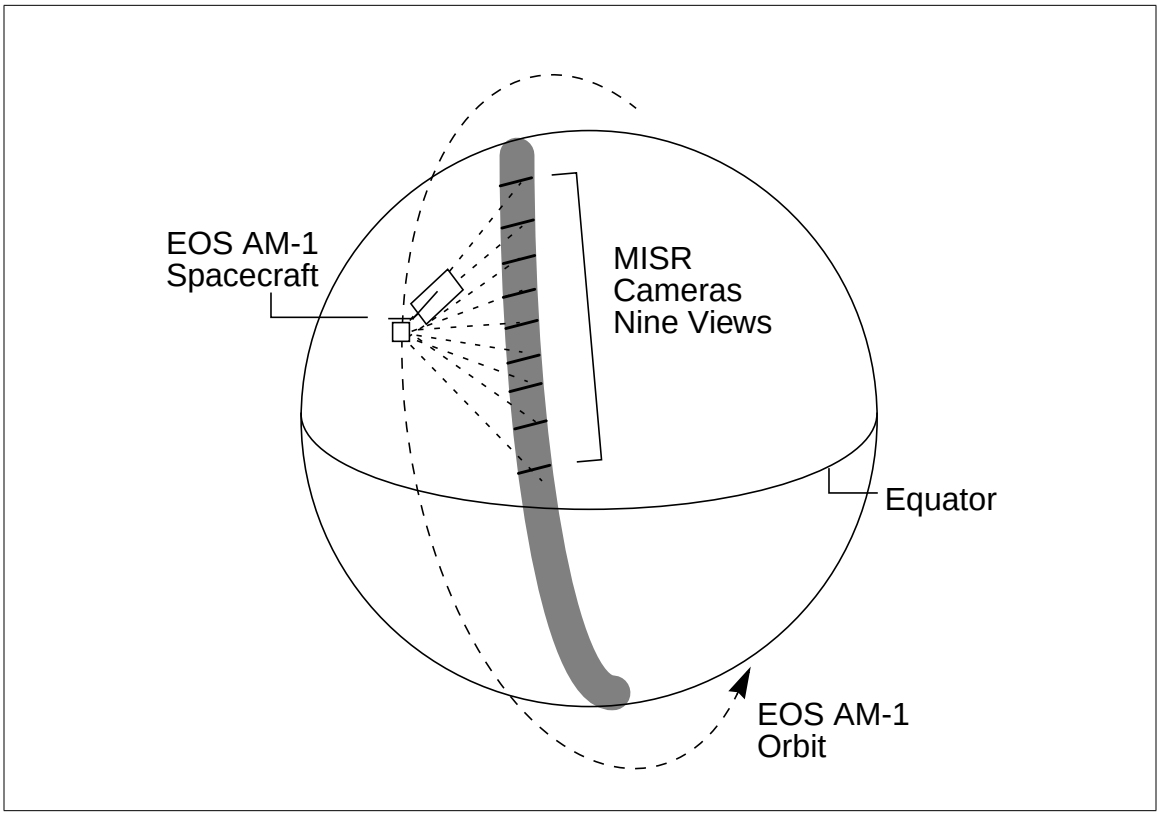

Figure 1: Schematic of EOS AM-1 orbit and MISR camera views

MISR contains 36 parallel signal chains corresponding to the four spectral bands in each of the nine cameras. Each signal chain contains the output from the 1520 pixels (1504 photo-active plus 8 of the light-shielded plus 8 "overclock" samples for the CCD serial registers) in each detector array. The zonal overlap swath width of the MISR imaging data (that is, the swath seen in common by all nine cameras along a line of constant latitude) is ≥360 km, which provides global multi-angle coverage of the entire Earth in 9 days at the equator, and 2 days near the poles. The cross-track Instantaneous Field of View (IFOV) and sample spacing of each pixel is 275 m for all of the off-nadir cameras, and 250 m for the nadir camera. Along-track IFOV's depend on view angle, ranging from 214 m in the nadir to 707 m at the most oblique angle. Sample spacing in the along-track direction is 275 m in all cameras. The instrument is capable of buffering the data to provide 2 sample x 2 line, 4 sample x 4 line, or 1 sample x 4 line averages, in addition to the mode in which pixels are sent with no averaging. The averaging capability is individually selectable within each of the 36 channels.

2.1.4 Observational modes

There are several observational modes of the MISR instrument. The two modes relevant to Level 1B2 algorithms are called Global Mode and Local Mode. Global Mode refers to continuous oper-

ation with no limitation on swath length. Global coverage in a particular spectral band of one camera is provided by operating the corresponding signal chain continuously in a selected resolution mode. Any choice of averaging modes among the nine cameras that is consistent with the instrument power and data rate allocation is suitable for Global Mode. Additionally, Local Mode provides high resolution images in all 4 bands of all 9 cameras for selected Earth targets. This is accomplished by inhibiting pixel averaging in all bands of each of the cameras in sequence, one at a time, beginning with the first camera to acquire the target and ending with the last camera to view the target. The instrument geometry limits the along-track length of Local Mode targets to about 300 km.

2.1.5 MISR science objectives

MISR multi-angle imagery will be used to monitor global and regional trends in radiatively important optical properties (optical depth, single scattering albedo, and size distribution) and amounts (mass loading) of natural and anthropogenic aerosols. Coupled with MISR's determinations of top-of-atmosphere and surface hemispherical reflectances, these data will provide a measure of the global aerosol forcing of the shortwave planetary radiation budget.

Land surface processes are important components of the terrestrial climate system. Models describing the interaction of surface and atmospheric processes require the ability to obtain quantitative information on fluxes of energy (radiation transfer), mass (water vapor and CO_2), heat (sensible and latent), and momentum (shear stress). These fluxes are directly influenced by the spectral, structural, geomorphological, and, in the case of vegetated landscapes, physiological properties of the surface. It is anticipated that estimates of surface hemispherical reflectance of vegetated sites can yield relatively accurate information about rates of evapotranspiration, photosynthesis, respiration, and radiation absorption.

Clouds play a major role in governing the Earth's energy balance. Many theoretical studies have established the inadequacies of plane-parallel representations of cloud fields in climate models, since diffusion of radiation through the cloud sides and side illumination causes the directional reflectances of cumuliform cloud fields to differ markedly from those of stratiform fields. Regional studies of the impact of clouds on the energy balance require measurements of the radiation budgets as a function of scene type. Since reflected solar fluxes cannot be directly measured on a regional scale from satellite altitudes, radiances from the same scene, measured more or less coincidentally at several different angles, must be observed and then integrated to yield the flux. Bidirectional reflectances of clear and cloudy regions obtained by MISR will be used to develop anisotropic reflectance models classified by cloud type, determine the spatial and temporal variability of cloud albedo, and validate coarse spatial resolution angular reflectance models generated by other instruments. Automated stereo matching of multi-angle imagery will be used to estimate cloud elevations. Additional information about these science objectives can be found in the MISR Experiment Overview [M-16].

2.2 MISR SCIENCE DATA PROCESSING OVERVIEW

2.2.1 MISR Science Data Processing

MISR Science Data System (SDS) generates science data products from MISR instrument data. The MISR Science Computing Facility (SCF) and Distributed Active Archive Center (DAAC) represent the primary entities in which the functions of MISR science data processing will be deployed. The MISR SCF will support the development of MISR science algorithms, as well as provide quality control and data validation services with respect to MISR science data processing. This will include production of data and coefficients used to augment and improve the performance of the science algorithms that operate at the DAAC. The MISR DAAC, which is shared with several other EOS instruments, will be the facility at which MISR science algorithms will operate in a high volume, near real-time mode to produce the standard science data products.

2.2.2 Standard data products generation

The generation of standard science data products at the DAAC can be divided into five production steps. Each step has at least one primary output product, but may have other secondary output products. It is convenient to think of these five steps as occurring in sequence, with the predecessor producing at least one complete product, a portion of which is the primary input for the successor. The five steps are 1) Instrument Data Reformatting and Annotation, 2) Radiometric Scaling and Conditioning, 3) Geometric Rectification and Registration, 4) Science Retrievals, and 5) Global Gridding. Each of these steps correspond to processing levels of a product generation flow, as shown in Figure 2. These levels conform generally to the EOS scheme from Level 1 to Level 3.

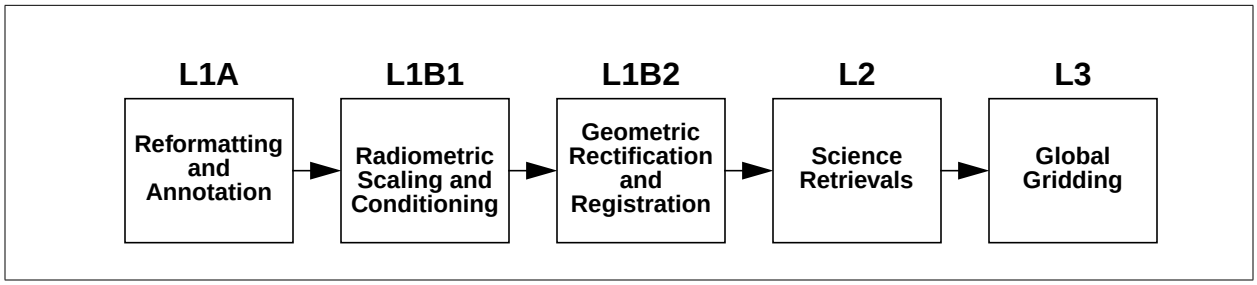

Figure 2: MISR Product Generation Flow

Production of standard products at the DAAC cannot operate independently of the rest of the MISR SDS. For example, it has critical dependence on calibration parameters and lookup data which must be produced at the SCF, such as threshold datasets, climatologies, model datasets or the like. These functions are separated from DAAC activities because they require much closer scrutiny by the MISR science team than the MISR DAAC could provide. Updates to these data structures occur infrequently compared to the rate of standard product generation, and therefore fit into the more limited processing capabilities of the SCF. Other essential functions of the SDS that have activities at the SCF include quality assessment, algorithm validation, software development,

and instrument operations, but these functions are not discussed further in this document.

2.2.3 Standard processing prior to Level 1B2

2.2.3.1 Level 1A

The Level 1A processing is defined to be the depacketizing, reformatting, and decommutating of Level 0 raw data to create the Level 1A Reformatted Annotated Product. The Level 1A product will also provide additional datasets containing platform ancillary data and pointers to coefficient files associated with MISR processing at the time of the Level 1A product construction. The reformatting will include a reversal of the square-root encoding performed in-flight. The data numbers (DNs) will be commuted from 12-bit numbers to 16-bit, byte-aligned half-words. Verification of packet sequencing, formats, and sizes will also be executed and reported. Other components of the Level 1A product will be pointers to calibration coefficient files provided for Level 1B processing, data quality indicators. The Level 1A product is the primary archive of the MISR instrument data. Each major Level 1A product granule represents a full orbit of data. The objective of the Level 1A product is to provide an easily accessible, standardized data format for subsequent product generation. It will represent a comprehensive depiction of all the raw MISR instrument data. The Level 1A product will consist of the MISR CCD, engineering, and calibration data. It will also include ancillary data representing platform timing, navigation and attitude data and metadata information.

2.2.3.2 Level 1B1

The only directly measured physical parameters observed by MISR are camera incident radiances. Higher level datasets, such as aerosol optical depth, bidirectional reflectance factor (BRF), or bihemispherical reflectance (BHR), are derived from these data. Yet, the DN transmitted by MISR only provide a measure of these radiances once a series of processing steps, called radiance scaling and conditioning, have been performed. During Level 1B1 processing (see the Level 1B1 ATB), MISR digital data are converted into a measure of the incident radiant field, weighted over the spectral response of the camera and output in the form of a Level 1B1 Radiometric Product. Inputs to the processing algorithm are Level 1A data, as well as the Ancillary Radiometric Product (ARP). The latter is a product describing the instrument characterization and calibration. Included in the ARP are sensor radiometric calibration coefficients, uncertainty in calibration, detector quality flags, spectral band parameters, field-of-view pixel parameters, and passband-weighted solar irradiance values.

2.2.4 Level 1B2 standard data processing overview

The Level 1B2 standard data processing is the automated process during which all of the parameters of the Level 1B2 Georectified Radiance Product are computed on an orbit-by-orbit basis. The Level 1B2 data flow paths relative to input from Level 1B1 and output to Level 2 are represented by Figure 3. This figure is the center portion of Figure 2 blown up to focus on Level 1B2. Both of

the Level 2 processing steps require MISR input that have been co-registered and projected to a common Space-Oblique Mercator (SOM) reference grid.

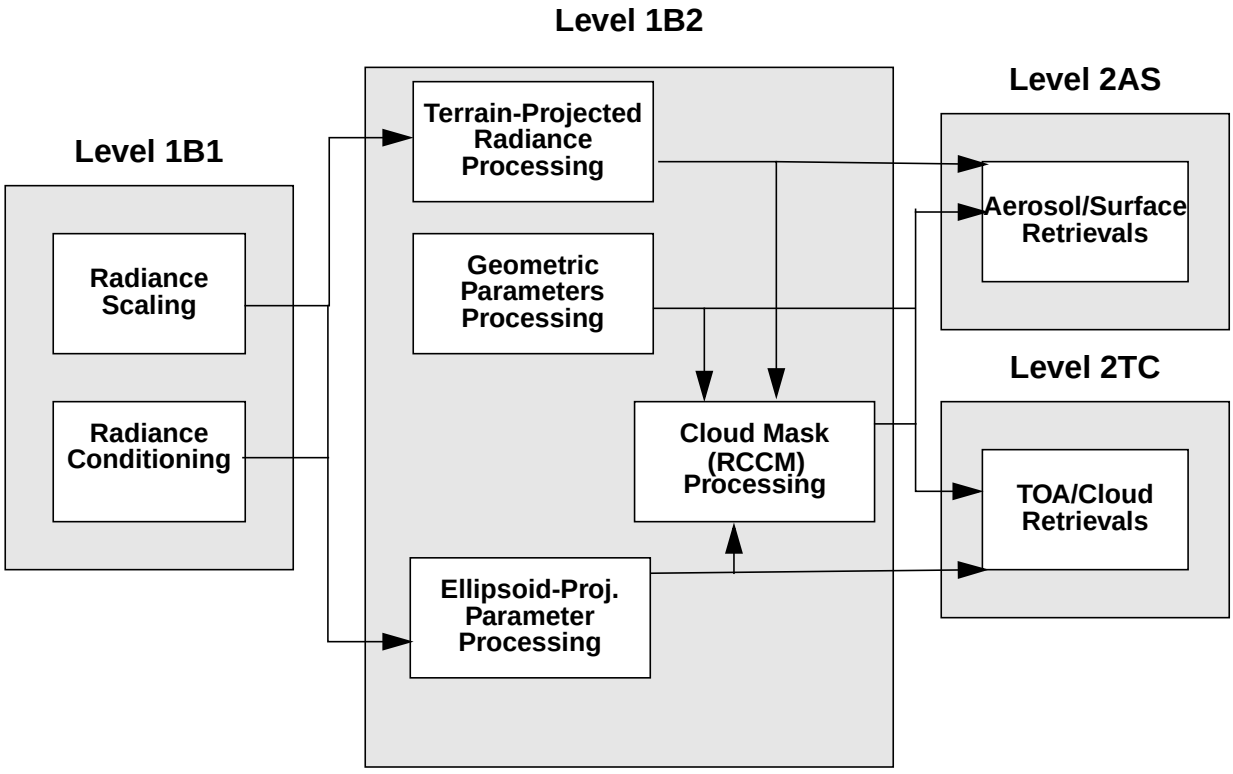

Figure 3: Product Generation Flow (Focused on Level 1B2)

What is not represented by the figure is input coming from supporting datasets. The supporting datasets created during in-flight geometric calibration will be staged at the DAAC as needed. An overview of the creation of these datasets is described in §3.5. The algorithm behind the production of Radiometric Camera-by-Camera Cloud Mask (RCCM) is described in a separate document titled MISR Level 1 Cloud Detection ATB [M-9].

2.2.4.1 Global Mode processing

The above flows describe the standard processing of *Global Mode* data. Global Mode (see §2.1.4) is the continual operation of the instrument in any camera configuration, consistent with constraints on the instrument power and data rate, in order to provide global observations. The output of Global Mode processing are the Georectified Radiance Product parameters summarized in

Table 1.

Table 1: Level 1B2 Geo-rectified Radiance Product (Global Mode parameters)

Parameter name	Units	Sampling
Terrain-Projected TOA Radiance	W m^{-2} sr^{-1} μm^{-1}	275 m - 1.1 km
Ellipsoid-Projected TOA Radiance	W m^{-2} sr^{-1} μm^{-1}	275 m - 1.1 km
Radiometric Data Quality Indicator (RDQI)	none	275m - 1.1km
Geometric Parameters (ellipsoid-referenced)	deg	17.6 km

2.2.4.2 Local Mode processing

As described in §2.1.4, the MISR instrument can also acquire data in what is referred to as *Local Mode* which provides high resolution (i.e., unaveraged) images in all 4 bands of all 9 cameras for selected Earth targets. This is accomplished by cycling through the cameras in sequence, beginning with Df, followed by Cf, Bf, Af, An, Aa, Ba, Ca, and finally Da. Data obtained from Local Mode sites will be used for new algorithm development, specialized research, calibration, field validation, instrument intercomparisons, or other purposes at the MISR SCF.

The algorithm objectives during Local Mode processing are identical to those during Global processing in terms of the algorithms used. The only difference is that the output is segregated to be available as a separate deliverable parameter as shown in Table 2. This parameter is the same as the surface-projected TOA radiance parameter of Global Mode processing except that radiances from all 4 bands of all 9 cameras are now projected to a high-resolution (275 m) sampling on the SOM grid.

Table 2: Level 1B2 Geo-rectified Radiance Product (Local Mode parameters)

Parameter name	Units	Sampling
Terrain-Projected TOA Radiance (Single Local Mode Scene)	W m^{-2} sr^{-1} μm^{-1}	275 m (Regional)
Ellipsoid-Projected TOA Radiance	W m^{-2} sr^{-1} μm^{-1}	275 m (Regional)
Radiometric Data Quality Indicator (RDQI)	none	275m (Regional)

3.0 GEOMETRIC PROCESSING (L1B2) ALGORITHM CONCEPT

3.1 INTRODUCTION

In order to derive geophysical parameters such as aerosol optical depth, bidirectional reflectance factor, and hemispheric reflectance, measured incident radiances from the multi-camera instrument must be coregistered. Furthermore, the coregistered image data must be geolocated in order to meet the following experiment objectives: a) produce a data set of value to long-term monitoring programs and allow intercomparassions of data on time scales exceeding that of an individual satellite, and b) provide Earth Observing System (EOS) synergism.

In order to provide coregistered and geolocated data, the ground data processing system is designed to geometrically process multi-angle multispectral data, so that they all conform to a common map projection. This is the first time an attempt has been made to rectify and map project remotely sensed data on-line, as it comes from the instrument. We define this segment of continuous and autonomous ground processing as “georectification”, and the derived product as the Georectified Radiance Product (GRP). There are two basic parameters of the Georectified Radiance Product depending on the definition of the reflecting surface: a) ellipsoid-projected radiance, and b) terrain-projected radiance. The ellipsoid-projected radiance is referenced to the surface of the WGS84 ellipsoid (no terrain elevation included) and the terrain-projected radiance is referenced to the same datum including a DEM over land and inland water.

In general, the georectification processing segment must deal with the pointing error composed of: a) camera internal geometric errors and b) errors in the supplied spacecraft ephemeris and attitude data. In addition, the processing related to the terrain-projected radiance must remove the distortion introduced by the topography that occurs when imaging with multiple viewing angles.

Besides the georectified radiance, certain parameters describing the sun-camera geometry at the time of imaging are required by the science retrieval algorithms. These parameters, called geometric parameters, are included as an additional part of the GRP. The geometric parameters consist of: a) sun zenith and azimuth angle and b) camera-view zenith and azimuth angle.

In this section we provide an overview of the theoretical concepts underlying the design of the science data processing system responsible for the georectification of MISR imagery and computation of the geometric parameters. In particular, we first relate geometry of the MISR imaging event to the georectification concept. Then we present algorithm design considerations including overlapping issues between the terrain and ellipsoid projections. An overview of the terrain-projection algorithm is given, followed by an overview of the ellipsoid-projection algorithm and an introduction to the creation of the ancillary datasets. At the end of this section, a brief description of the geometric parameters computation is given, followed by issues related to the map projection selected as the common grid for the Georectified Radiance Product.

3.2 GEORECTIFICATION - FROM PHYSICAL TO “VIRTUAL” MISR

In regards to the science algorithms requirements, the physical MISR (see Figure 4) is the closest practicable but not a sufficient approximation to the desired instrument. In this design 9 multiangle views observe widely spread points on the surface. For science processing algorithms, we design the output to appear as is from a “virtual” instrument (see Figure 5) in which the images are coregistered. From the practical standpoint, the desired (i.e perfect) instrument cannot be created relying exclusively on hardware. Therefore, the limitations of the MISR hardware prevail over the design of the software of the MISR Science Data Processing System. For example, the coregistration and geolocation limitations of the physical MISR are overcome utilizing the georectification software. This software converts actual MISR imaging events to the imagery which would be collected by the ideal “virtual” MISR.

3.2.1 Geometry of MISR imaging event

The EOS AM-1 orbit parameters and MISR instrument characteristics are given in §2.1.2 and §2.1.3 respectively. The nominal geometry of a MISR imaging event (Figure 4) can be derived from the orbit parameters and instrument characteristics. Some of the derived geometric attributes relevant to the georectification are: a) the maximum instantaneous displacement in the along-track direction is about 2800 km, b) an along-track displacement between four spectral bands within a single camera is between 2 km and 12 km depending on the camera type, c) the cross-track instantenous field of view (IFOV) and sample spacing of each pixel is 275 m for all of the off-nadir cameras, and 250 m for the nadir cameras, d) along-track IFOV’s depend on view angle ranging from 250 m in the nadir to 707 m at the most oblique angle, and sample spacing in the along-track direction is 275 m in all cameras.

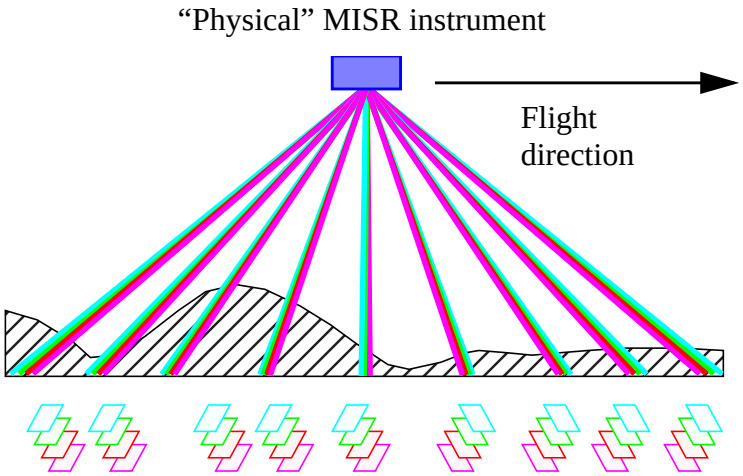

Figure 4: MISR imaging event

In order to find the geolocation corresponding to a pixel's field of view, the pixel pointing direction is expressed in the geocentric coordinates system, as follows:

$$\hat{\rho} = T_1 T_2 \hat{r} \tag{1}$$

where $\hat{r}$ is the pixel pointing direction relative to the instrument coordinate system defined by the observable image coordinates and the set of constants representing the instrument interior orientation parameters. In the following text, this set of constants is called the Camera Geometric Model (CGM) dataset. T_2 represents the transformation between the instrument and spacecraft coordinate axes. T_1, defined by the ephemeris and attitude data at the time of imaging, represents the transformation between the spacecraft and geocentric coordinate system. Equation (1) is an often-used photogrammetric model suitable for various image-ground point determinations, and provides a basis for our georectification algorithm.

3.2.2 Georectified Radiance Product (GRP)

The GRP is created primarily in response to the co-registration and geolocation requirements of MISR science algorithms. Effectively, it represents a continuously superimposed set of multi-angle multi-spectral data. In an abstract world the terrain-projected radiance and ellipsoid-projected radiance may be looked upon as the data collected by a "virtual" MISR, Figure 5.

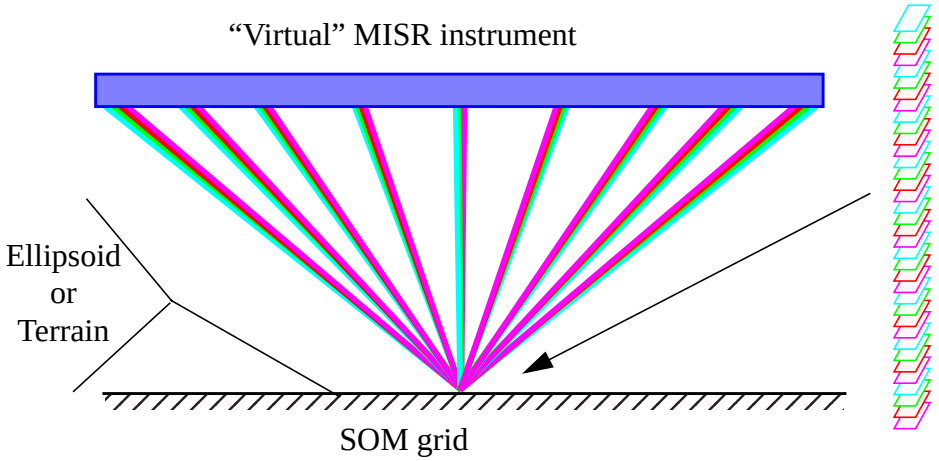

Figure 5: Georectified Radiance Product: output from a "virtual" MISR.

For all practical purposes the terrain-projected radiance and ellipsoid-projected products are a col-

lection of global orthorectified digital image maps obtained during the period of 6 years (based on the 16-day orbit repeat cycle). These digital maps cover the globe between ±81° latitudes, due to the inclination of the AM-1 orbit. Each map contains
radiances from four spectral bands. We have selected Space Oblique Mercator [35] as the reference map projection grid because it is designed specifically to suit continuous mapping of satellite imagery. The chosen ground resolution of the map grid is 275 m.

3.2.3 Georectification algorithm design consideration

The two most important factors driving the design of the georectification algorithm are: 1) product requirements, and 2) processing constraints. Theses factors are presented in Figure 6 along with the derived algorithm design goals.

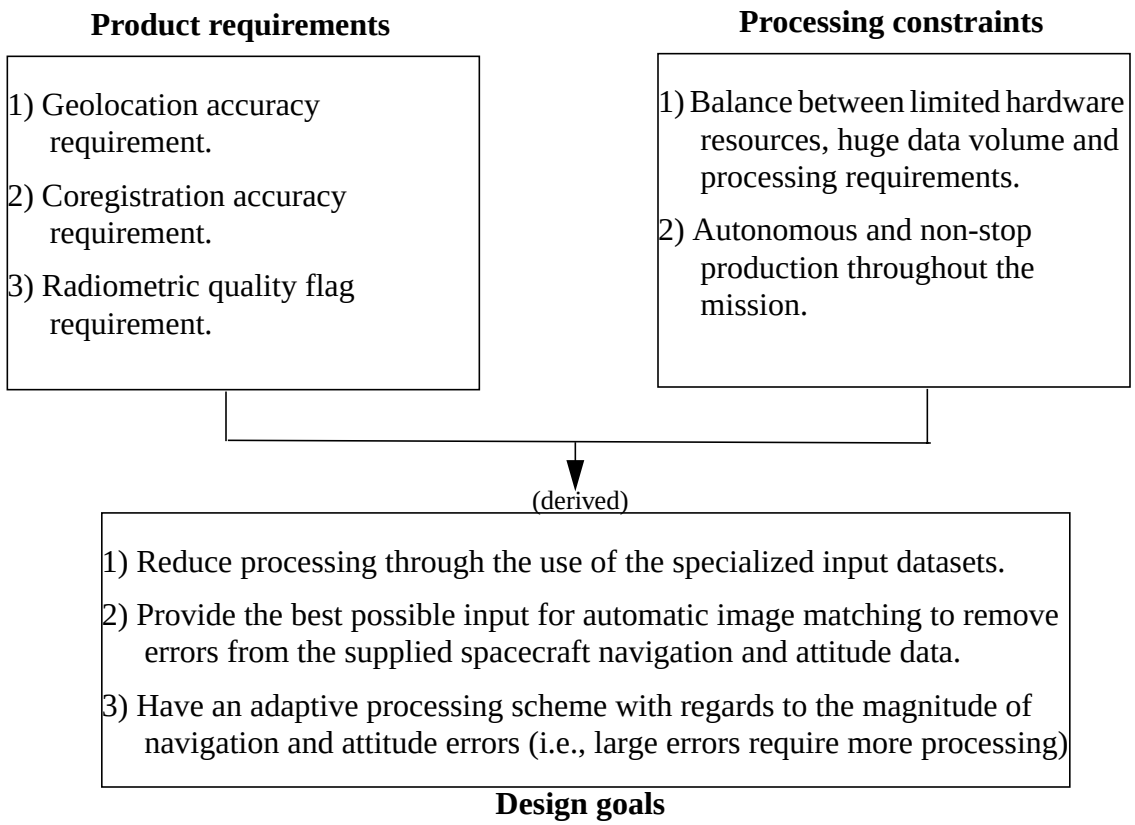

Figure 6: Algorithm design consideration

The GRP accuracy requirements are specified in the MISR Data System Science Requirements [M-5] (DSSR) and will be summarized here for completeness.

The first product requirement is for imagery in each spectral band of the MISR nadir camera to be geolocated to ±250 m in both the cross-track and along-track directions for radiances projected to the smooth surface of reference ellipsoid WGS84, and ±275 m for radiances projected to the surface terrain (including topographic relief effects). These are specified at a confidence level of 95%. The geolocation requirement insures accurate placement of MISR data products on a geographical grid and co-registration of MISR imagery of a particular target acquired on multiple orbits, thereby insuring the ability to separate actual temporal changes on the Earth from misregistration errors.

The second product requirement is for imagery of a particular target from all bands of the nine MISR cameras to be spatially co-registered with an uncertainty of ±250 m cross-track and ±500 m along-track at a confidence level of 95%, for the ellipsoid-projected radiances; these values become ±275 m cross-track and ±550 m along-track for the surface projections. Registration of the data at these levels is driven primarily by the aerosol and surface retrievals, but is also necessary for the TOA/cloud retrievals in order to provide input of high geometric fidelity into the retrievals.

The above specified accuracies require accurate knowledge of surface elevation while producing the terrain-projected radiance. In addition, the accuracy specification for the supplied navigation and attitude suggest the possibility of horizontal error of about 2 km excluding topography. However, the spacecraft and instrument pointing are expected to be stable within a single orbit. A specification of 20 arcsec (peak-to-peak, 3σ), over a 7 minute period, in each of the pitch, roll, and yaw axes is given in the MISR UIID. In addition, the sun-synchronous nature of the orbit is expected to result in small orbit-to-orbit variations at the same location within the orbit. This high degree of stability and repeatability is factored into the Level 1B2 processing algorithm strategy, and helps reduce the number of computationally expensive calculations which need to be performed at the DAAC.

The third product requirement (listed in the Figure 6) is related to the radiometric quality of the GRP which is basically once-resampled radiance acquired by MISR instrument. The requirement is to propagate MISR radiometric data quality information into the GRP.

Our processing scenarios has been shaped by the above-described requirements in conjunction with the production hardware and the autonomous and non-stop aspect of the production system. Overviews of the algorithms which will meet the above specified design goals will be given in the next two sections. Although there are overlapping issues between terrain-projection and ellipsoid-projection processing, these two algorithms are treated separately.

3.2.4 Terrain-projection algorithm

Both the Level 2 Aerosol/Surface retrievals and the cloud mask generation within the Level 2 TOA/Cloud retrievals (see the Level 2 ATBs) need radiances from all nine cameras of MISR to be coregistered and projected to a surface of the Earth using a common projection system, which

ensures that the same surface boundary condition applies to each of the nine views.

The corrections for topographic distortions, removal of band displacement, and removal of errors in the supplied navigation and attitude data must be continuous and autonomous during the 6 year period of the mission. Considering the algorithm design goals (see Figure 6), our process is streamlined to a recursive image-to-image registration algorithm. The underlying idea is to derive information which does not change significantly during the course of the mission once, saving it for future use as ancillary data. For example, the topographic distortions are going to be very similar for all MISR imagery from the same orbit path due to the high repeatability specification on the EOS-AM1 spacecraft. So, the ancillary datasets created prior to and at the beginning of the mission, and then used throughout the mission are an important part of the overall algorithm. These datasets are:

1) Paired Reference Orbit Imagery (ROI) and Projection Parameters (PP) along with the Camera Geometric Model (CGM) which together constitute the Geometric Calibration Dataset (GCD)

2) Ancillary Geographic Product (AGP)

3) Paired Radiometric Camera-by-camera (RC) Threshold Dataset and Cloud Screening Surface Classification (CSSC) Dataset.

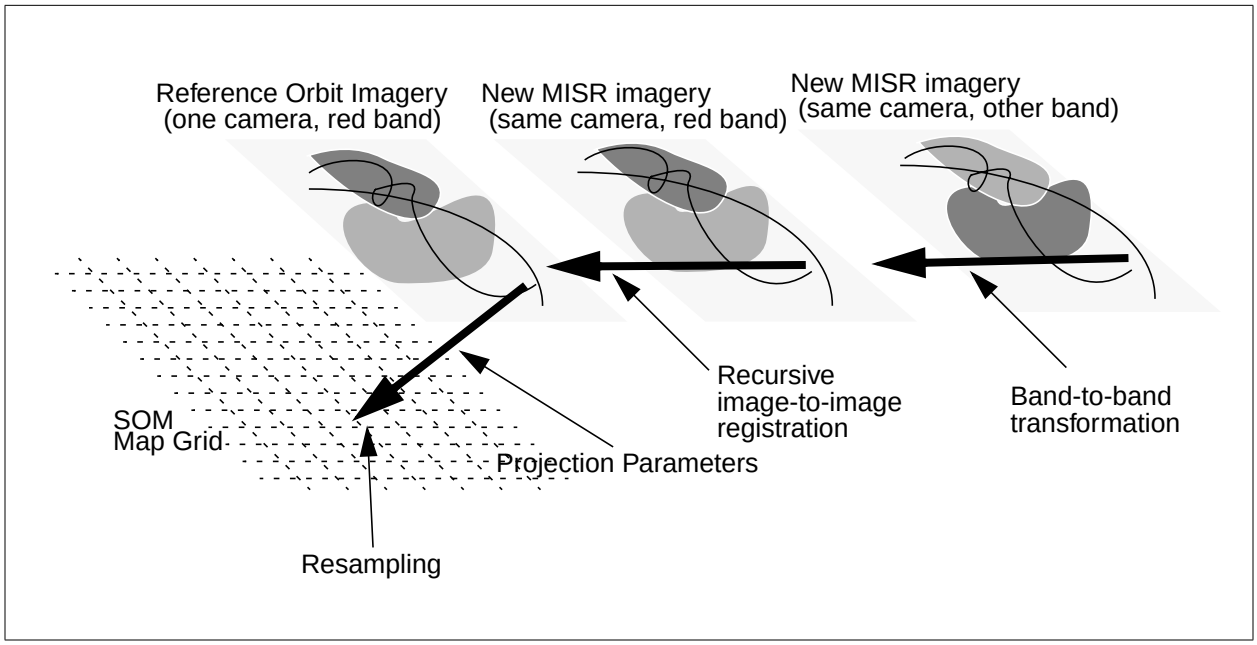

Figure 7: Implementation of terrain-projected parameter algorithm

The paired ROI and PP indirectly contain the error free navigation and attitude data as well as the topographic distortions relative to the various geometry of the nine MISR cameras. This information is routinely exploited through a hybrid image registration between new MISR imagery and

the ROI. The CGM defines pointing of MISR pixels internal to the instrument and independent of the outside elements (e.g., navigation and attitude). The AGP provides definition of the selected map grid (i.e., georeference) and a coarse resolution Digital Elevation Model (DEM). The paired RC Threshold Dataset and the CSSC Dataset are used to determine whether a particular area is to classified as cloudy or clear, for the purpose of determining suitability for image matching.

The ancillary datasets are created during specialized activities at the MISR SCF, and will be supplied to the DAAC for standard processing. In §3.5 we give a brief overview of the creation of the ancillary datasets. Also reference documents [M-8], [M-9] and [M-10] describe the algorithms behind the production of the ancillary dataset.

The entire terrain-projection algorithm (see Figure 7) can be divide into three parts: 1) band-to-band transformation, 2) recursive image-to-image registration (Figure 8), and 3) bilinear resampling. Parts 1 and 3 are relatively simple processes which will be described in §4.3.3 and §4.3.6. The real heart of the algorithm is registration between new MISR images and the ROI using the red band data. The red band is used for all cameras for two reasons: a) global imagery at the highest resolution (275 m) will be obtained in the red band, b) the red band is the best in regards to the image matching, which is a part of registration, as it is expected to have the largest contrast. The major components of the registration algorithm are:

a) Image Point Intersection (IPI): a backward projection function used to provide an initial location of the conjugate points (see §4.3.4).
b) Image matching for the precise identification of the conjugate points (see §4.3.5).
c) Transformation (mapping) function between two images (see §4.3.2.2).

The registration method is adaptive with regard to the character and size of misregistration, in order to minimize the size of the processing load. The adaptive nature of the algorithm is attained by recursively dividing images into subregions until the required registration accuracy is achieved. Due to the push-broom nature of the MISR cameras, subregions are rectangles extending over the image in the cross-track direction. The mapping function associated with a subregion is a modification of the affine transform which includes known geometric characteristics of the MISR imaging event. Once the mapping between the two images is established, the last processing step is the assignment of the appropriate radiance value to the grid points of the SOM map.

This is done by one of the standard (e.g., bilinear) resampling methods.

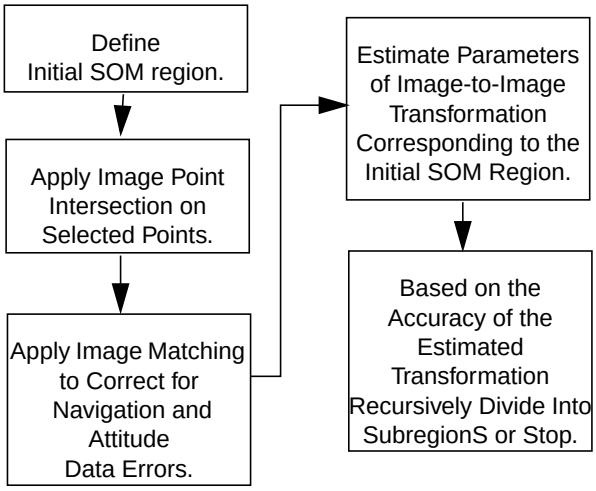

Figure 8: Recursive Image-to-Image Registration

Additional techniques are required so that autonomous production runs are unaffected by the more challenging aspects of the input data. Some of the more obvious examples are the presence of cloudy regions, water bodies, and deserts. These types of conditions significantly reduce the number of conjugate points available to determine the transformation function. In such cases additional techniques must be implemented. In some cases, searching for cloud-free land in the local neighborhood may be sufficient (see §4.3.2.3). In other cases, where a large region of data is without conjugate points, use of information obtained through the registration of the closest subregion is applied. The idea is to correct for slowly varying parameters through the use of a Kalman filter built while processing previous subregions.

Also included in the algorithm is a blunder detection technique (§4.3.2.5) aimed at removing possible blunders coming from the image matching. This utilizes statistical results obtained from the least-square estimation of the transformation function.

3.2.5 Ellipsoid-projection algorithm

Level 2 TOA/Cloud retrievals (see [M-11]) need the radiances from all nine cameras of MISR to be additionally projected to a surface defined by the reference World Geodetic System 1984 (WGS84) ellipsoid. This surface is where camera-to-camera stereo matching will be performed to determine cloud altitude.

The ellipsoid-projection is a less complicated algorithm than terrain-projection for two reasons: 1) there are no topographic distortions, and 2) corrections due to errors in the supplied navigation and attitude data are obtained during terrain-projection and only applied here; there is no need for

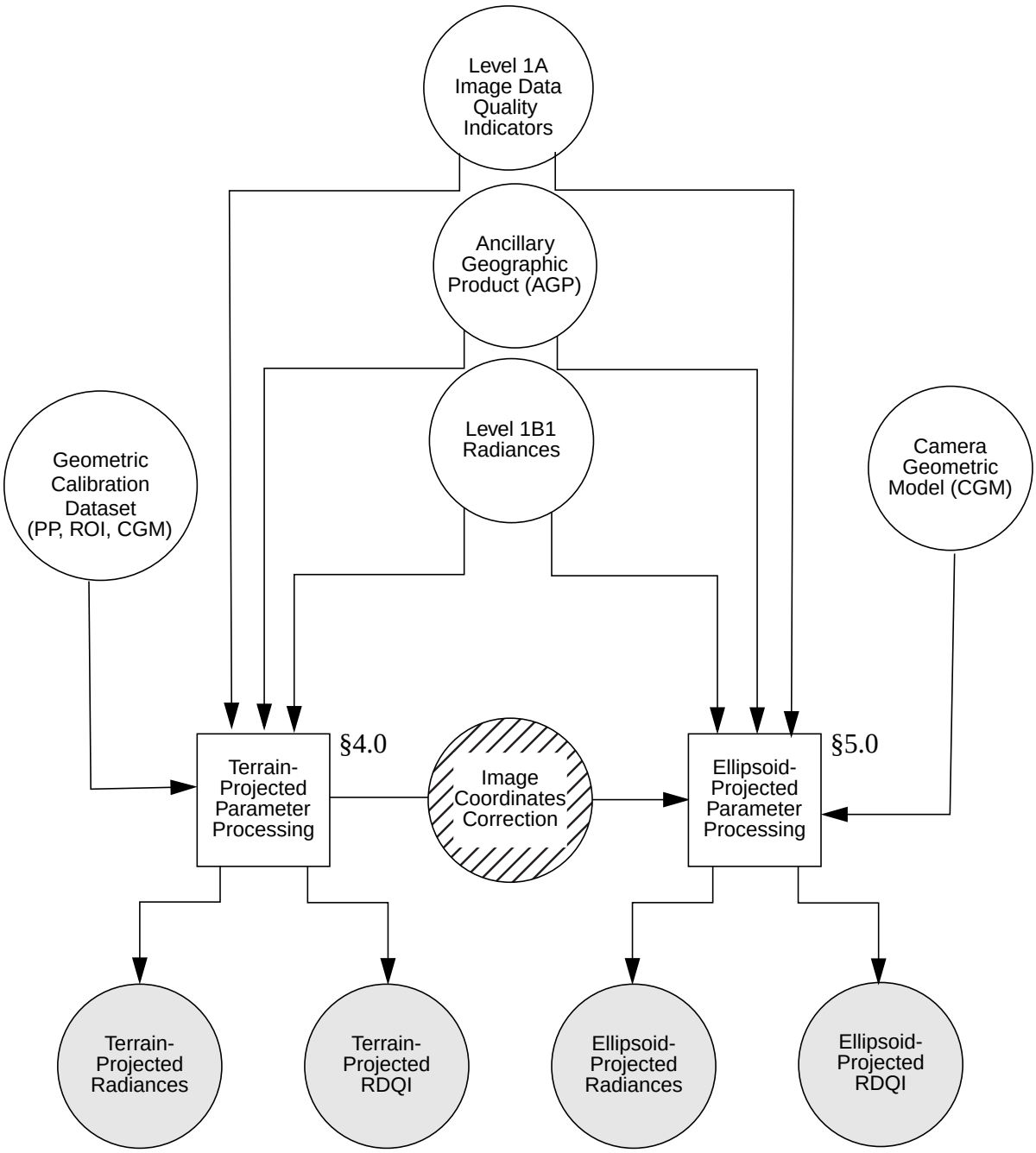

Figure 9: Level 1B2 CCD science processing flow

image matching. The Ancillary Geographic Product (AGP), Ancillary Radiometric Product (ARP), and Camera Geometric Model are used as supporting datasets. There is no need for Reference Orbit Imagery (ROI) or the Projection Parameters (PP) file. Instead of doing image-to-image registration and georeferencing via PP, the new MISR imagery is directly related to the map projection. For more detail on this algorithm see §5.3.1.

The terrain-projection and ellipsoid-projection together are looked upon as the georectification part of the L1B2 processing. Since there are overlapping issues and shared datasets between these two segments, the processing flow can be shown on a single diagram (Figure 9).

3.3 GEOMETRIC PARAMETERS ALGORITHM

Needed by all Level 2 science algorithms for several types of retrievals as well as Level 1 Cloud detection are the *geometric parameters* which supply the sun and view zenith angles on the WGS84 ellipsoid relative to a normal to that surface, as well as azimuth angles relative to local North. These angles are reported on a grid with 17.6 km spacings. The sun zenith and azimuth angles are determined from Earth and Sun ephemerides at the time of viewing. The view zenith and azimuth angles are based upon the reported spacecraft attitude and position and the calibrated camera model. The Ancillary Geographic Product is used to defined the map grid. The geometric parameters algorithm is described in detail in §6.0

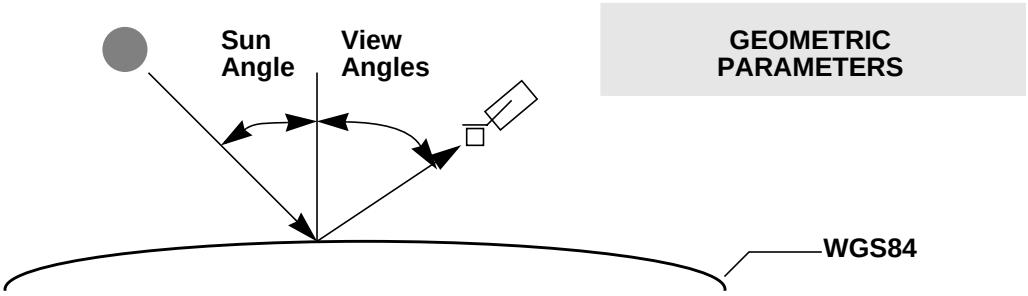

Figure 10: Geometric parameters

.

3.4 MAP PROJECTION GRID

MISR Level 2 science algorithms require all Level 1B2 data to be resampled to a common map projection. This projection must precede the Level 2 processing, as Level 2 processing requires that all 36 channels are viewing the same geographic location within each sample.

Ideally there should be a minimum of errors introduced into the image dataset, prior to the retrieval of geophysical parameters at Level 2. The coregistration process requires topographic corrections, which dictates that ground locations are known. The multiple datasets are all acquired at different time and hence an intermediate data gridding scheme is necessary, one that must be ground located. Space-Oblique Mercator (SOM) is a means of achieving this while introducing minimal distortions into datasets as a result of the projection itself. SOM, in which the projection meridian nominally follows the spacecraft ground track, has the following attributes:

1) The grid is uniform from equator to pole, and is thus operationally simple for single orbit processing.

2) There is negligible equator-to-pole shape and scale distortion in the cross-track direction, none along-track.

3) There is small (at most a few degrees) rotation between the CCD image elements and the SOM grid.

4) Projected imagery closely matches CCD data in geometric characteristics, which is beneficial for Level 2 algorithms.

5) Distortion and resampling effects are minimized.

The map resolution of the projection will be matched to the horizontal sampling mode of each camera channel. A separate projection will be established for each of the paths of the 233 repeat orbits of the EOS 16-day cycle. The horizontal datum for each projection has been chosen to be the WGS84 ellipsoid.

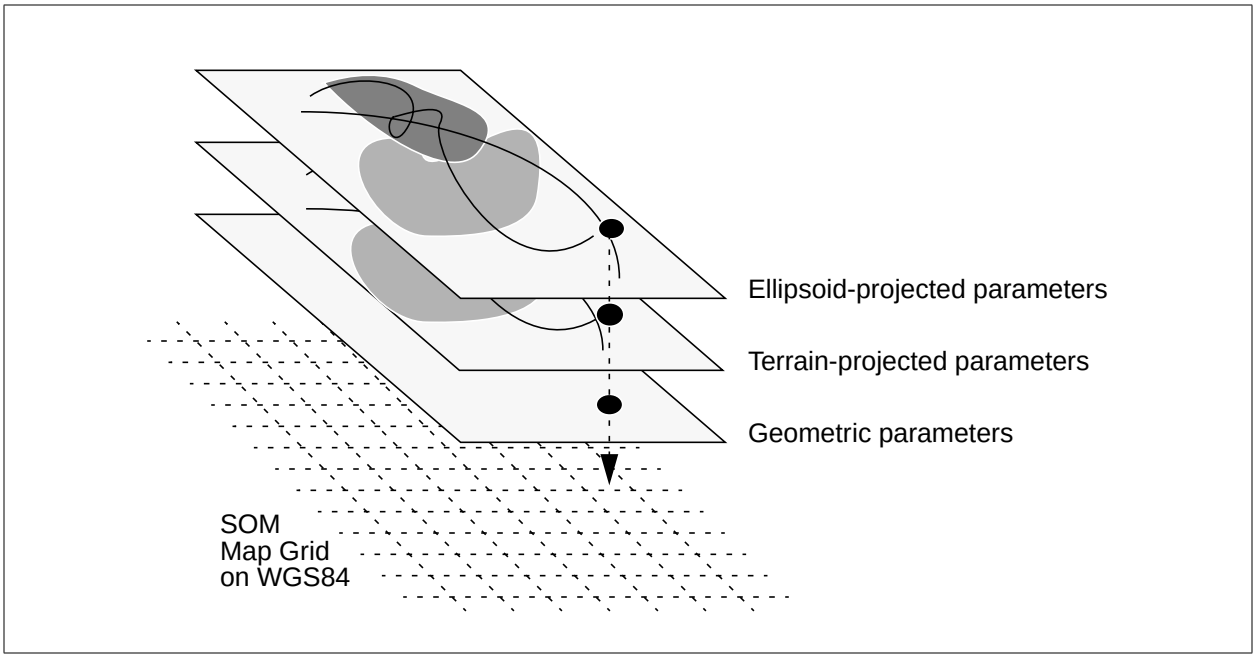

Figure 11: The gridded L1B2 products

Since each of the orbit paths repeat, the projection grid for each path can be calculated after the orbit is determined, that is, very early in the mission. The projection grid can then be stored and used routinely for all successive cycles. This grid will be established by the Ancillary Geographic Product (see §3.5.1 and MISR reference document [M-8]), which exists as a separate, archived, supporting dataset.

By establishing a common map projection for the Level 1B2 parameters, a basis for Level 2 science algorithms is formed, as required to account for the manner in which the instrument acquires the data and the algorithms need to utilize these data. In addition, the map projection allows direct cross-comparison with geolocated data from other instruments and simplifies global mapping at Level 3, since the data has already been geolocated. The predetermined SOM grid is thereby an intermediate step on the way to the Earth-based map projections of Level 3. Because the SOM projection minimizes distortions and resampling effects, it permits the greatest flexibility in the choice of the Earth-based projections to be used at Level 3.

3.5 SUPPORTING DATASETS

There are two supporting datasets that are constructed prior to standard processing. These are the Ancillary Geographic Product (AGP) and Geometric Calibration Dataset. The latter consists of a Camera Geometric Model (CGM), and paired Reference Orbit Imagery (ROI), and Projection Parameters (PP) files. These datasets are generated at the SCF and then delivered to the DAAC for use in routine processing. Table 3 summarizes information in and intended use of each dataset, relative to the geometric processing. The construction of each of these datasets is described in detail in the corresponding Algorithm Theoretical Basis documents. In this section, only a brief overview on the creation and use of the supporting datasets is given.

Table 3: Information and use provided by the ancillary datasets
(relative to the geometric processing)

Dataset	Information Provided	Use
Ancillary Geometric Product (AGP)	1. Map grid definition. 2. Coarse surface elevation. 3. Land/water identifier.	1. To obtain initial tie points for registration. 2. Guide for image matching.
Radiometric Camera-by-camera (RC) Threshold Dataset	1. Nominal thresholds used in cloud detection algorithm	1. In-line detection of clouds prior to matching

Table 3: Information and use provided by the ancillary datasets
(relative to the geometric processing)

Dataset	Information Provided	Use
Cloud Screening Surface Classification (CSSC) Dataset.	1. 59 ecosystem classes mapped onto a 10-arc-min grid over globe.	1. In-line detection of clouds prior to matching.
Geometric Calibration Dataset (GCD)		
Camera Geometric Model	1. Geometric camera parameters describing internal MISR camera viewing geometry.	1. To obtain accurate MISR pointing vectors prior to associating imagery with the navigation and attitude data.
Reference Orbit Imagery (ROI)	1. Unresampled MISR imagery. Global land.	1. To do image matching during registration in order to correct for errors in the navigation and attitude data.
Projection Parameters (PP)	1. Georeference 2. Topography	1. To obtain tie points during registration 2. To georeference new MISR image registered to ROI

3.5.1 Ancillary Geographic Product

The Ancillary Geographic Product (AGP), parameters of which are shown in Table 4, is utilized in the creation of all MISR Level 1B2 and Level 2 products throughout the mission, and needs to be a deliverable to allow interpretation of the products. The shaded row represent the parameters specifically used for L1B2 geometric processing. All of the parameters in this product are generated at the MISR SCF and delivered to the DAAC for use in standard processing. The AGP itself consists of 233 files, corresponding to the 233 repeat orbits of the EOS spacecraft. The parameters in this product are reported in a Space-Oblique Mercator (SOM) map projection. The map scale of the projection is 1.1 km; this defines the horizontal sampling for each of the parameters. The horizontal datum, or surface-basis, for the projection is the WGS84 ellipsoid. This map projection

and surface-basis is identical to what will be used for all the Level 1B2 and Level 2 parameters.

Table 4: Level 1 Ancillary Geographic Product Description By Parameter

Parameter name	Units	Horizontal Sampling and (Coverage)	Comments
Geographic latitude	deg	1.1 km (Global)	• Relative to WGS84 ellipsoid
Geographic longitude	deg	1.1 km (Global)	• Relative to WGS84 ellipsoid
Average scene elevation	m	1.1 km (Global)	• Relative to WGS84 ellipsoid
Point elevation	m	1.1 km (Global)	• Relative to WGS84 ellipsoid
Standard deviation of scene elevation	m	1.1 km (Global)	• Calculated from sub-1.1 km data • If sub-1.1 km data not present, a flag will indicate source.
Regional average scene elevation	m	17.6 km (Global)	• Relative to WGS84 ellipsoid
Regional standard deviation of scene elevation	m	17.6 km (Global)	• Calculated from 1.1 km data
Average surface-normal zenith angle	deg	1.1 km (Global)	• Relative to WGS84 ellipsoid-normal at surface
Standard deviation of scene elevation relative to mean slope	m	1.1 km (Global)	• Calculated from values used to establish the surface and slope
Average surface-normal azimuth angle	deg	1.1 km (Global)	• Relative to local North at WGS84 ellipsoid
Land/water identifier	none	1.1 km (Global)	• Land/ocean/inland water/ephemeral water/coastline mask
Dark water algorithm suitability mask	none	1.1 km (Global)	• Corresponds to ocean or inland water areas which are 5 km from a shoreline and >50m deep

3.5.2 Geometric Calibration Dataset

In-flight geometric calibration essentially consists of two parts: the calculation of a calibrated camera model for the MISR instrument and the creation of MISR reference orbit imagery and their associated projection parameters.

3.5.2.1 Camera Geometric Model

The output of the first part of in-flight geometric calibration is a calibrated camera model which describes the interior (instrument-related) and exterior (viewing geometry) orientation of the instrument. This calibration is to correct for any alignment changes which may have occurred during launch and to account for repeatable, thermally-induced pointing variations affecting the instrument and which may occur during each orbit, but which are not possible to simulate pre-flight. A number of Ground Control Points (GCPs) image chips are used during this calibration.

The calibrated camera model is supplied to the DAAC for standard processing. During the mission, the calibrated camera model may be recalculated depending upon analysis of the stability of the EOS AM-1 spacecraft and the MISR instrument over time.

3.5.2.2 Reference Orbit Imagery and Projection Parameters

The second part of in-flight geometric calibration involves the creation of MISR Reference Orbit Imagery (ROI) corresponding to the 233 unique EOS AM-1 orbits, and the calculation of Projection Parameters (PP) associated with each of these orbits, during the first several months of the mission. The work involved in the creation of these datasets is directly related to the design goals (see Figure 6) 1 and 2 of our production system.

As related to objective 1, the expensive computation required for topography displacement will be performed only once, off-line. The information obtained will be saved into a file (i.e. PP file) and utilized during on-line processing throughout the mission. This is possible due to the small orbit-to-orbit variations at the same location within an orbit path.

With regards to objective 2, we use unresampled but geolocated MISR imagery (i.e. ROI) as the ground control information. The concept is that only MISR imagery with the same viewing geometry will provide a high success rate during least-square area based image matching.

The ROI consists of unresampled MISR imagery which will be matched to new MISR orbits, during standard processing of the surface-projection parameter algorithms. The ROI has the following characteristics: 1) since image matching can only be performed between images which have sufficient texture, ocean images (and other areas of little texture) can not be used. Over oceans, the improvement of the supplied spacecraft position and pointing is based on the results of the matches over nearby land. 2) Multiple coverage of single orbits will be utilized and mosaicked, whenever possible, to provide for cloud-free land images and to compensate for the areas affected by seasonal variations and the ground-contrast reduction expected for the highly oblique views.

A set of PP files corresponding to the ROI is produced using rigorous photogrammetric reduction methods. The PP file provide geolocation information for as-acquired MISR imagery on a pixel by pixel basis. This geolocation information is referenced to a selected Space Oblique Mercator map projection grid.

The process of creating ROI and PP files is similar to the regular orthorectification of time dependent sensor imagery. The major differences are: a) acquired imagery is geolocated but not resampled, and b) a global DEM of sufficient resolution is available for MISR's internal use. In particular, a simultaneous bundle adjustment utilizing multi-angle imagery and ground control information (global DEM and ground control point chips) is used to model errors in the navigation and attitude data for a single set of ROI prior to geolocation. The detail description of the algorithm behind production of the PP and ROI is given in the In-flight Geometric Calibration ATB [M-10].

3.5.2.3 RC Threshold and Cloud Screening Surface Classification Datasets

A version of the Radiometric Camera-by-camera (RC) Threshold Dataset created prior to launch and the Cloud Screening Surface Classification Dataset will be used in order to identify cloudy regions during the registration of ROI to the new MISR image. Detected cloudy regions will not be used as the input to image-matching. However, the cloud detection algorithm uses a statistical approach with the confidence levels depending on the selected threshold. In particular, every MISR pixel may be classified into one of the four categories: 1) cloud with the high confidence (CloudHC), 2) cloud with low confidence (CloudLC), 3) clear with the low confidence (ClearLC), and 4) clear with the high confidence (ClearHC). In order to meet our goal, i.e., avoid cloudy regions during image matching, but also not give up too much of the area that can be suitable for matching we will rely on the set of thresholds that eliminate CloudHC regions. More detail about this cloud detection algorithm and related datasets can be found in references [M-9] and [4]. A version of this algorithm used prior to image-to-image registration is described in §4.3.2.4.

4.0 TERRAIN-PROJECTION ALGORITHM

4.1 ALGORITHM SUMMARY

MISR terrain-projection (i.e., orthorectification) algorithm is based on the following approach: 1) The output map-projection grid is predefined. 2) For each ground point corresponding to the map grid centers, obtain its location in the relevant MISR image. 3) Resample radiances of the pixels surrounding the image location of the map grid centers and obtain the radiance value which is assigned to the map grid. The complex part of this approach is step 2, which can be reduced to image-to-image registration with the use of the paired Projection Parameters (PP) file and Reference Orbit Imagery (ROI). The PP file provides locations of the map grid centers in the selected MISR imagery within the ROI. Through the registration between the new MISR image and the ROI a transformation between coordinate systems of these two images is obtained. The transformation is used to obtain locations of map grid centers in the newly acquired MISR image. Registration between new MISR images and ROI is done using the red band because of its availability in the highest resolution and favorable characteristics in regards to image matching. Therefore, a transformation between the other three MISR bands and the red band must be computed in order to terrain-project the other three bands. The resampling of the acquired MISR imagery uses the Image Data Quality Indicators (IDQI) (see [M-7]) as an input in order to produce radiometric quality indicators of the terrain-projected product. The geometric quality indicators are based on the image registration. A side product of this algorithm are the Image Coordinate Corrections which will be used during ellipsoid-projection in order to account for errors in the navigation data.

4.2 ALGORITHM INPUTS

4.2.1 MISR data

4.2.1.1 MISR radiance imagery

MISR radiance imagery is derived at Level 1B1 and consists of calibrated radiances in all 9 cameras x 4 channels of the instrument. These radiances have not had any atmospheric correction applied and include both surface and atmospheric contributions to the signal. Also, Image Data Quality Indicators are associated with the radiance values and are part of the LB1 product.

The process for calibrating the radiance values is described in the MISR Level 1 Radiance Scaling and Conditioning Product ATB, JPL D-11507, Rev B. The content of the Level 1B1 product containing radiance values and IDQI is described in the MISR Data Product Description, JPL D-11103.

4.2.2 Datasets generated at the SCF and supplied to the DAAC for staging

The Geometric Calibration Dataset and two ancillary products (i.e. AGP, ARP) are generated at the SCF and supplied to the DAAC to be staged for standard processing, and are summarized in

Table 5. A high level description of these datasets is given in Section 3.5. Some further information on the elements of the GCD, which is designed specifically for the geometric processing, are given below.

Table 5: Datasets generated at the SCF and supplied to the DAAC

Dataset	Source of data
Ancillary Geographic Product	Various DEM's and other sources
Projection Parameters	MISR In-flight geometric calibration
Reference Orbit Imagery	MISR In-flight geometric calibration
Calibrated Camera Model	MISR In-flight geometric calibration
Radiometric Camera Threshold Dataset	MISR Science Team
Cloud Screening Surface Classification Dataset	MISR Science Team

4.2.2.1 Projection Parameters

The projection parameters created during in-flight geometric calibration define image positions in the MISR Reference Orbit Imagery of the georeferenced location defined by the Space Oblique Mercator map projection grid centers. This set of projection parameters maps the predefined SOM grid of the Ancillary Geographic Product (AGP) to the MISR reference orbit nadir and off-nadir imagery. The calculation of this mapping during in-flight calibration will involve simultaneous bundle adjustment of nine MISR cameras. There are 233 PP files for each of the nine MISR cameras. The number 233 corresponds to the number of AM-1 spacecraft orbital revolutions for one repeat cycle.The creation of the projection parameters is described in the MISR L1 In-flight Geometric Calibration ATB, JPL-D 13399.

4.2.2.2 Reference Orbit Imagery

The reference orbit imagery will consist of full swaths of MISR images which have been geolocated according to projection parameters determined during in-flight calibration. This imagery will be used for matching to newly acquired MISR imagery. Each reference orbit may consist of mosaicked sections of several overlapping orbits in order to obtain reference imagery which is relatively free of clouds. There are 233 ROI for each of the MISR nine cameras. The construction of the reference orbit imagery is described in the MISR L1 In-flight Geometric Calibration ATB, JPL-D 13399.

4.2.2.3 Camera Geometric Model

This is a model of each MISR camera that allows us to determine in what direction a particular CCD element is looking relative to the spacecraft coordinate system. This model includes the

effect of thermal variations which may cause a systematic variation of camera pointing during the course of an orbit. The creation of the calibrated camera model is described in the MISR L1 Geometric Calibration ATB, JPL-D 13399.

4.2.2.4 Radiometric Camera-by-camera (RC) Threshold Dataset

This dataset is used for in-line cloud detection during terrain-projection processing in order to avoid image-matching over the cloudy region. A version of this dataset will be created at the MISR Science Computing Facility (SCF) prior to flight and then delivered to the DAAC. This first version of the dataset contains nominal values fro the static thresholds to be used early in the mission. During the first several months of the mission, MISR data will be used to revise the static values of the thresholds, and a new version of the RC Threshold Dataset will be delivered from the SCF to the DAAC. The detail information on the context of the RC Threshold Dataset is given in reference document [M-9].

4.2.2.5 Cloud Screening Surface Classification (CSSC)Dataset

This dataset is used for in-line cloud detection during terrain-projection processing in order to avoid image-matching over the cloudy region. It is used in conjuction with the RC Threshold Dataset. A pre-launch version of the CSSC will be derived from the WE1.4D version of the Olson's global ecosystem database [22]. Version WE1.4D contains 59 ecosytems classes mapped onto 10-arcmin grid over the globe. The detail information on the context of the RC Threshold Dataset is given in reference document [M-9].

4.2.3 Other inputs

4.2.3.1 Navigation and attitude data

In order to georeference viewing directions of the CCD elements defined by the Camera Geometric Model (CGM), the spacecraft navigation and attitude data must be known. In particular, the navigation and attitude data will complement the CGM in order to find initial tie points, prior to image matching, during registration of new imagery to ROI.

The navigation data of special interest to the georeference are spacecraft position and velocity vectors. The navigation system uses a high accuracy output based on the TDRSS Onboard Navigation System (TONS) as the primary method of producing navigation data. The second (backup) means of navigation is a coarse accuracy output based on propagating a set of uplinked Brouwer-Lyddane mean orbit elements. In the spacecraft "Normal Mode" primary and backup navigation operate in parallel in order to facilitate the execution of fault detection, isolation, and recovery logic. The TONS navigation filter provides near real-time estimates of EOS-AM position and velocity every 10.24 seconds. The Guidance, Navigation and Control Subsystem (GN&CS), which provides position and velocity every 1.024 seconds, uses a second order Taylor series intergrator to do estimation between TONS measurements. The position and velocity vectors are

reported relative to the Geocentric Inertial Coordinate System of the mean Equator and Equinox of J2000.

The attitude data are produced through an attitude determination algorithm based on Kalman filtering theory. This algorithm receives measurements of stars or Sun and provides a 6-element state correction vector consisting of 3 small angle attitude errors and 3 gyro bias compensation errors. Calls are made to the Kalman update filter every 10 seconds, if stellar or solar measurements are available. At other times the attitude is propagated using gyros. The GN&CS provides attitude angles relative to the Orbital Coordinate System, and attitude rates relative to the Spacecraft Coordinate System every 1.024 seconds.

The spacecraft navigation and attitude dataset is provided by GN&CS through the spacecraft ancillary data message. During standard processing the spacecraft ancillary data message will be accessed using the PGS toolkit routines. These routines interpolate between the ancillary data to provide data at the time of interest.

The TONS accuracy estimates and attitude determination accuracy estimates combined with the accuracy of the interpolation routines must fall within MISR navigation and attitude accuracy and knowledge requirements. Navigation requirements as stated in the EOS-AM Spacecraft Pointing Study PDR Update of August 31, 1993, are:

1) Position accuracy: 150 meters, (3σ), per axis.

2) Velocity accuracy: 0.160 meters/second, (3σ), per axis.

Requirements related to the attitude determination are stated in reference document [M-18].

3) Pointing accuracy: 150 arc-sec, (3σ), per axis.

4) Pointing knowledge: 90 arc-sec, (3σ), per axis.

5) Pointing stability: 14/420 arc-sec per second, (3σ), (peak-to-peak), in roll and pitch.

6) Pointing stability: 17.7/420 arc-sec per second, (3σ), (peak-to-peak), in yaw.

7) Pointing jitter: 5/1 arc-sec per second, (3σ), (peak-to-peak), per axis.

4.3 ALGORITHM DESCRIPTION

4.3.1 Introduction

As mentioned in section Section 4.1, with the use of paired PP file and ROI the terrain-projection problem is basically reduced to an image-to-image registration method. Once the registration is achieved, and image-to-image transformation parameters obtained, the last processing step is a standard resampling (i.e. bilinear interpolation) of the acquired MISR imagery. Image-to-image registration is done first for the red band in a different manner than for the other three bands due to

its availability in the highest resolution for all nine cameras. In the following subsections image registration of the red band will be described first, and then the description of the terrain-projection for the other bands will be given. Once the transformation parameters are obtained, the resampling of all four bands is identical and will be described in section Section 4.3.3.

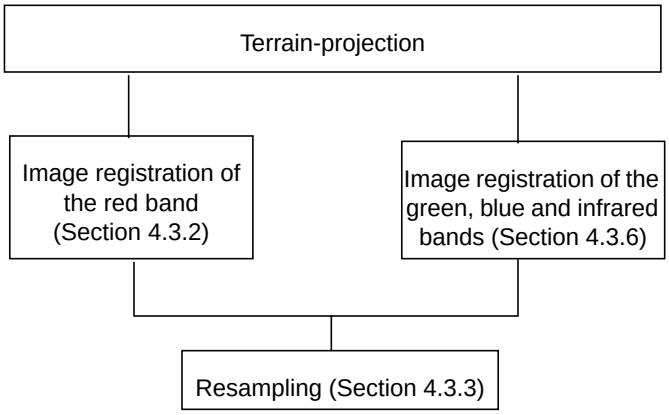

Figure 12: Elements of the terrain-projection algorithm

4.3.2 Red band image-to-image registration algorithm

Image registration between the red band of new imagery and the ROI is a process of determining the positions of corresponding points in the respective images. The first level of processing consists of two steps: 1) selection of the points in the two images and determination of the correspondence between them and 2) determination of the parameters of the transformation function using image positions of the corresponding tie points.

The accuracy of the registration depends on the following factors: a) accuracy of the corresponding tie points positions, b) type of transformation function, c) number and distribution of the tie points used to determine parameters of the transformation function, and d) size of the local geometric distortion for the region where a set of transformation parameters is applied. The accuracy of MISR tie point positions is assumed to be defined by the accuracy of the area based least-square image matching method. In general, if there is a successful match, the accuracy is better than 1/10 of the pixel for images with the same viewing angle as the case of new MISR data and ROI. The transformation function is derived by looking at the physical characteristics of the MISR pushbroom camera. The number and definition of the tie points depend on factors which are unpredictable before the new MISR image is obtained, for example, cloud cover. The size of the local geometric distortions depends not only on the local 3D structure of the scene but also on the perturbation of the navigation data.

In the second level of processing, which is initialized only when necessary, we deal with unfavor-

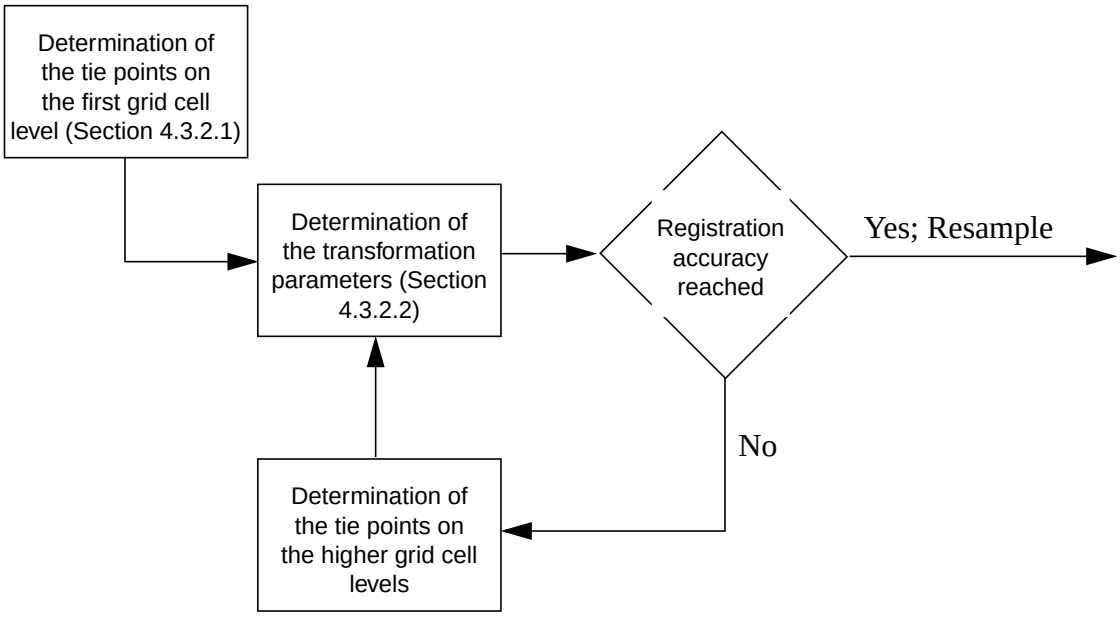

Figure 13: Process diagram for the image registration of ROI and MISR new imagery (red band)

able conditions in a adaptive manner to the point where the desired accuracy is reached. The processed image will be divided recursively into subregions (i.e. grid cells) of varying sizes depending on the magnitude of local misregistration. The determination of tie points for the first grid cell level is different than the determination of tie points on the higher grid cell (subregion) level.

The determination of the transformation parameters through the use of the tie points positions is the same at every subregion level (Section 4.3.2.2).The decision of whether the desired accuracy has been reached is made independently for each subregion.

It should be pointed out that the use of image matching during determination of the tie points for the first subregion level allows computation of the so-called Image Coordinate Corrections. These ICC are used to account for errors in the navigation data during ellipsoid-projection (Section 5.0) and, when processing neighboring subregion with very few tie points.

4.3.2.1 Determination of the tie points

First grid cell level

The geometric processing of MISR imagery is done separately for each camera on a orbit-by-orbit

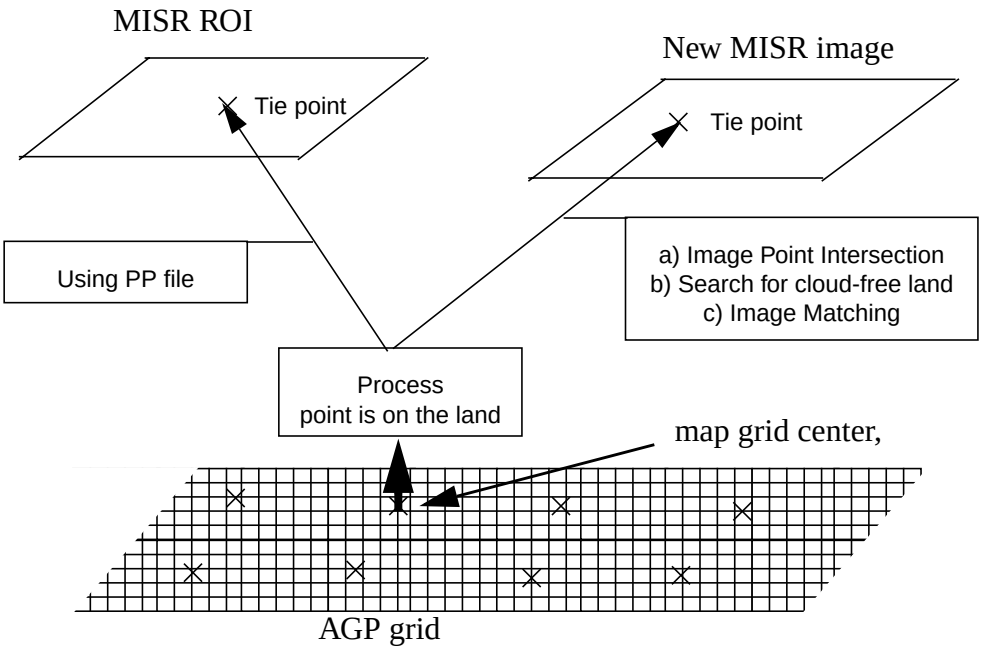

Figure 14: Determination of tie points for the first grid cell level

basis. Each of the new MISR images will have a set of associated PP, ROI and AGP files.

The AGP defined SOM map projection grid will be used as the roadmap for the image registration. In particular, the projections of the ground locations, corresponding to the map grid centers, back to the images are used as the tie points. The entire AGP grid is divided into initial subregions, called grid cells. The length of the initial grid cell is 256 MISR nominal lines and this choice is based on the prediction of orbit perturbations together with prototype results. The width of the initial grid cell is about 2048 MISR nominal nadir pixels, somewhat larger than the MISR FOV, to allow for possible displacement of the AM-1 repeat orbits. Determination of the tie points and image registration (as well as later resampling) is done on a grid cell by grid cell basis.

An initial grid cell may have many map grid centers which can serve as candidates for tie point determination. A rectangular network (5 x 10) of grid center points is selected with points being equally distributed across the grid cell. The operations done on each of these points are:

1) Using information from the AGP file, find out if the point belongs to an ocean or land region. If it is ocean, flag it and search in the vicinity for the closest land point. If it is land originally or land is found in the neighborhood, continue to the next step. The goal of this operation is to recognize, early in the processing, points which are not suitable to become tie points. Ocean regions will be processed only with the ellipsoid-projection algorithm.

2) For the selected ground point (i.e. map grid center) find the coordinates in the ROI using the PP file. This is accomplished due to the fact that the PP file and the AGP are in the same SOM map grid and the PP contains the needed information. The result of this operation is the position of the tie point in the ROI.

3) For the selected ground point (i.e map grid center) find the corresponding coordinates in the new MISR image using the Image Point Intersection (IPI) algorithm, a backward projection described in Section 4.3.4.

Once steps 1, 2 and 3 are completed for all points in the original 5x10 grid, an initial set of the transformation parameters for the first subregion level is computed using the algorithm described in Section 4.3.2.2. However, this transformation is not as accurate as it might be due to the inaccuracy of the tie points in the new MISR image obtained using only IPI. The IPI propagates back to the image space all of the errors contained in the navigation data. Therefore, an area-based image matching algorithm will be applied at points in suitable areas (e.g., cloud-free land) in order to get accurate coordinates of the tie points. The matching algorithm is described in Section 4.3.5. The search for cloud-free land regions is described in Section 4.3.2.3. After the matching of all suitable points is completed, a more accurate set of transformation parameters is computed. The statistics obtained during the estimation of the transformation parameters can be used to detect eventual tie point outliers introduced by the erroneous image-matching result. A blunder detection algorithm is implemented (Section 4.3.2.5) in order to prevent propagation of the errors into transformation parameters.

Accuracy of the transformation

The last step prior to going to resampling is to determine if the transformation parameters are accurate enough for the entire subregion at the first level. In particular, newly obtained transformation parameters are used to locate certain grid points which did not participate as the tie points (i.e., check points) in the new imagery. The locations of these points are tested via image-matching. The discrepancies are compared to the assigned threshold. In the case of large discrepancies this subregion will be divided in half, and new sets of tie points corresponding to the newly defined subregions will be obtained.

Second and higher subgrid cell levels

The new set of candidate tie points represents the TiePointsRow x TiePointsColumn (i.e., 5x10) grid of map grid centers equally distributed over the newly defined subregion. The location of these tie points in the ROI is obtained through the Projection Parameters. The determination of the tie point locations in the ROI at this level and higher does not require the use of the Image Point

Intersection function. Instead, the transformation parameters defined at the previous level are used. However, implementation of the grid point selection, image-matching and blunder detection will be the same at every grid cell level. The ultimate goal is to obtain desired accuracy by recursively subdividing to the higher cell levels. Due to the subdivision, size of the grid cell, available for transform, will reduced at each subsequent level. There is a limit on the size of the grid cell beyond which the grid cell would be inappropriate to use. This limit is equal TiePointsRow squared (25) in the along track direction and TiePointsColumn squared (100) in the across track direction.

4.3.2.2 Determination of the transformation parameters

Introduction

The form of the image-to-image transformation was derived by looking at the physical characteristics of a push-broom camera. We built a model that describes how a scan line of the reference image maps to the new image. We then assumed that the mapping for nearby scan lines should be nearly identical. Although the model was derived for a single scan line, we apply it to a larger area (nominally 256 lines of data).

The physical aspects that were included are a) linear optics, b) Earth curvature, and c) effect of ground topography.

Mathematical description of the algorithm

If we ignore for a moment the effect of (b) and (c), then we have the situation pictured in Figure

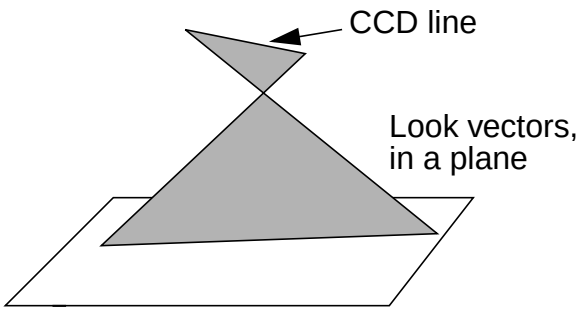

Figure 15: Scan line

15. In this approximation, all the look vectors for a single scan line lie in a plane. The ground is a plane, so the intersection of the scan plane with the surface is a straight line. This is true for both the reference and the new image. This means that lines in the reference image get mapped to lines

in the new image. The most general transformation that takes a line to a line is:

$$s_{new} = k_1(l_{ref} - l_0) + k_2(s_{ref} - s_0) + k_3 \quad (2)$$

$$l_{new} = k_4(l_{ref} - l_0) + k_5(s_{ref} - s_0) + k_6 \quad (3)$$

This is simply the affine model. l_0 and s_0 are the coordinates of the center of the line, e.g. l_0 is l_{ref} and s_0 is 1503 / 2 = 751.5.

We can include (b), the effect of the Earth's curvature, by looking at the disparity between the new and reference image due to topography. Looking at Figure 16, we see that

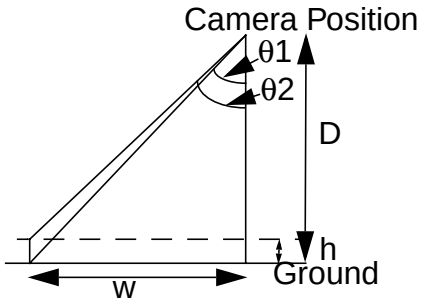

Figure 16: Finding effect of height change

$$\tan\theta_1 = \frac{w}{D} \quad (4)$$

$$\theta_2 - \theta_1 = \frac{w}{D^2 - w^2}h + O\left(\frac{wh^2}{D^3}\right) \quad (5)$$

In the linear optic approximation, we have

$$\theta = \theta_0 + \frac{(s - s_0)}{f}p \quad (6)$$

where *f* is the focal length and *p* is the pitch. Using equations (6) and (5) we have

$$\Delta s_{new} - \Delta s_{ref} = \frac{p}{f}\left(\frac{w_{new}}{D_{new}^2 - w_{new}^2} - \frac{w_{ref}}{D_{ref}^2 - w_{ref}^2}\right)h \quad (7)$$

For a spherical model of the earth, simple geometry gives:

$$h = \sqrt{R_{earth}^2 - w_{new}^2} - h_0 \tag{8}$$

If we plug equation (6) into (4), then (4) into (8) and (7), and finally (8) into (7), we get an expression for $s_{new} - \Delta s_{re}$ in terms of s_{new} and s_{ref}. We can then do a series expansion, to get an expression of the form:

$$\begin{aligned} \Delta s_{new} - \Delta s_{ref} &= k_7 + k_8 s_{new} + k_9 s_{ref} + k_{10} s_{new}^2 \\ &+ k_{11} s_{ref} s_{new} + k_{12} s_{ref}^2 + \text{Higher Order} \end{aligned} \tag{9}$$

The explicit form of the constant terms can be calculated, but they are unimportant for our use. What is important is that the quadratic coefficients are not zero, and that if we calculate the next order term we find that it is less than 10% of the quadratic terms.

Using a similar argument, we see that we can include (c), the effect of ground topography, by adding a term proportional to $h_{surface}$.

This gives a modification to (2) and (3) of

$$\begin{aligned} s_{new} &= k_{14}(l_{ref} - l_0) + k_{15}(s_{ref} - s_0) + k_{16}(s_{ref} - s_0)^2 \\ &+ k_{17} h_{surface} + k_{18} \end{aligned} \tag{10}$$

$$\begin{aligned} l_{new} &= k_{19}(l_{ref} - l_0) + k_{20}(s_{ref} - s_0) + k_{21}(s_{ref} - s_0)^2 \\ &+ k_{22} h_{surface} + k_{23} \end{aligned} \tag{11}$$

Testing shows that the corrections we have derived to the affine model are important. The quadratic term at the edges of the swath can be as large as 2 pixels.

4.3.2.3 Grid Point Selection

Introduction

After the set of transformation parameters is obtained using the tie points determined by the Image Point Intersection (IPI) algorithm only, a refinement of the tie points locations will be done via area based image-matching. The goal of this algorithm is to locate a number of points in the SOM map grid which can be used as tie points suitable for image-matching. Areas such as cloud-free land are considered to be good choices. Prior to grid point selection an in-line cloud detec-

tion algorithm must be implemented in order to define cloudy regions in new MISR imagery. This algorithm called “Image navigation clear sky mask” is described in Section 4.3.2.4. The selected grid points need to satisfy the following requirements:

1. Grid points are to be well distributed over the grid cell.
2. Each grid point needs to have a projection parameter defined for it. This means that:
   a. The grid point must be within the area that projection parameters are defined.
   b. The grid point must not be in a location that is not seen by the given camera (e.g., an obscured location).
3. If possible, each grid point should be in an area suitable for doing image matching between the ROI and the new imagery (this is not always achievable). This means that:
   a. The grid point should be on land (as opposed to ocean or inland water).
   b. The grid point should be in an area where the ROI is available.
   c. The grid point should be in a cloud free area large enough to accommodate the area based image matching search windows.
4. If possible, grid points that have already been used in other grid cells should be used. This reduces the computational load of L1B2 terrain-projected processing.

Note that requirement 3c leads to a serious complication. In order to determine if a point in the map grid is in a cloud free area, it is necessary to relate the map grid (which is in a ground based coordinate system) to the cloud mask (which is in image based coordinates). However, this relationship has not yet been made at this stage of processing. Indeed, the entire point of this algorithm is to enable us to relate the map grid to the MISR imagery. In order to find grid points that are cloud free, it is necessary to first construct an approximate image-to-image transform based on navigation data only. This approximate transform is then used to select cloud free grid points, which in turn are used to generate a better image-to-image transform based on both navigation data and image matching. More details on this dynamic cloud screening can be found in Section 4.3.2.4.

Algorithm Description

The following algorithm was developed to find grid points meeting the above requirements (see Figure 17):

1. Select a starting location for each grid point by equally distributing the grid points over the grid cell. Determine the area that the grid point will be allowed to move in, such that the grid point stays within the grid cell and the search areas are disjoint.
2. Shift the grid points within the allowed search areas so that each grid point is on land and is seen by the given camera (e.g., not obscured by topography). Note that may not be possible for all grid points (e.g., a grid point in the center of a large lake). If a grid point cannot be shifted to land, then mark the grid point as unusable and ignore it in future calculations. Use the resulting grid points to generate an approximate image-to-image transform by locating a conjugate point in the ROI through the PP and in the new imagery by using the IPI.

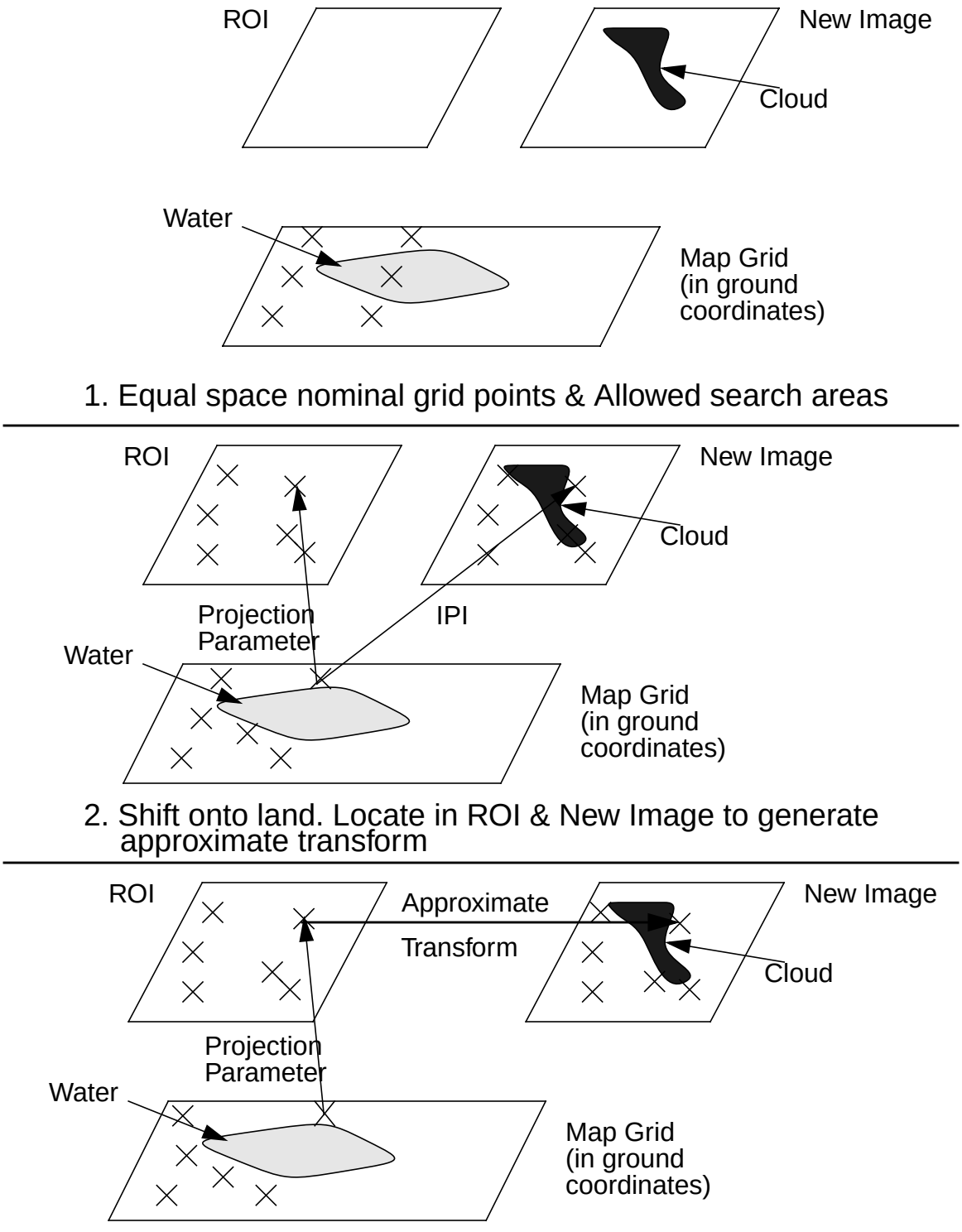

Figure 17: Grid Point Selection Algorithm

3. Use the approximate transform to shift the grid points out of cloudy areas in the new image, still keeping the grid point on land and out of obscured areas. Note that this may not be possible for all grid points (e.g., a grid point in the center of a large cloud). If a grid point cannot be shifted out of a cloudy area, it can still be used. Instead of determining the location of the conjugate point in the new image through image matching, an IPI is used.

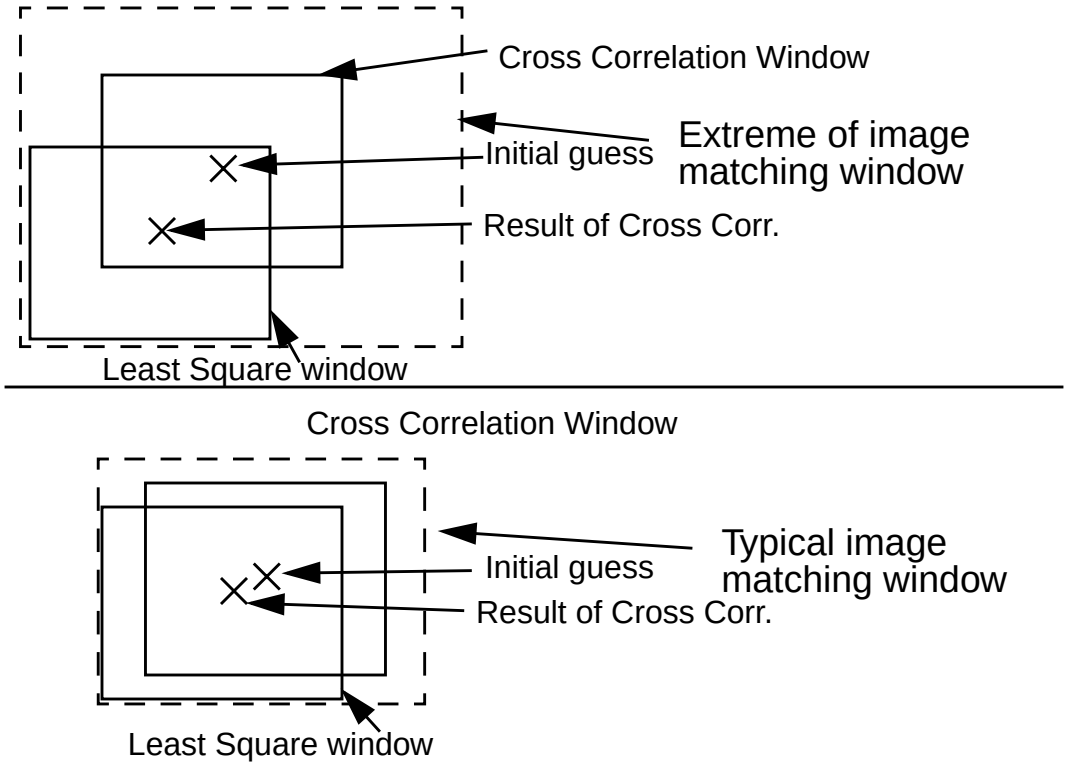

Figure 18: Range of Image Matching Windows

This algorithm can find grid points suitable for building the final image-to-image transform. However, a couple of refinements have been made to this algorithm to improve its performance:

1. Whenever possible, grid points are reused from neighboring and/or lower level grid cells. A grid point is used if it falls within the search area of one of the nominal grid points produced in step 1. This helps reduce the computational load of L1B2 terrain processing.
2. There is some uncertainty in exactly how much cloud free area needs to surround a point in the new image in order for image matching to be done successfully on it. The necessary win-

dow size is a combination of the results of cross correlation with the needed window size of least squares matching (see Figure 18). A window size that accounts for the maximum allowed error in the initial guess of image matching (~10 pixels) can be checked. However, much of the time a much smaller window is suitable (one allowing for ~1 pixel error in image matching). What we have done is modify the algorithm as follows:

a. The entire search area for a grid point is searched to see if a cloud free area allowing the maximum allowed error in the initial guess can be found. If it can, then that location is used as a grid point.
b. If no such area can be found, then a search is made to see if a cloud free area allowing the more typical error in the initial guess can be found. Note that it may turn out that this point is actually not suitable for doing image matching. After the cross correlation is done, a check must be made to ensure that there is enough cloud free imagery to do a least squares matching. If there is not, then the location of the conjugate point in the new imagery is found by cross correlation alone, without doing a least squares match. However, most of the time the point will have enough cloud free imagery to do matching

4.3.2.4 Image navigation clear sky mask

Introduction

Before performing image matching on a tie point it needs to be sufficiently free of clouds. This is achieved by generating a clear sky mask that is input to the grid point selection procedure. This mask is of the same dimension and coordinate system as the red band imagery segment. Cloud detection requires knowledge of the surface type over which the cloud is seen by the camera. But the clear sky mask is needed as an input to the algorithm that produces geolocation. A well defined cloud detection algorithm is performed on geolocated MISR data, but cannot be used for the clear sky mask because it relies on accurate determination of surface classification. Therefore a modified cloud detection algorithm was developed that only requires crude geolocation and is insensitive to land/water misclassification [4]. In order to perform this algorithm the red and infrared imagery need to be coregistered and crude geolocation needs to be determined. This is achieved by forward projecting a set of regular spaced red band image points to their ground intersection points, estimating geolocation and surface parameters for this intersection, backward projection from this intersection to the infrared image, and finally generating a band-to-band registration transform using the tie points in the red and infrared images.

Mathematical description of the algorithm

A set of evenly spaced image points are selected from the red band image. Each point is then projected to its intersection with a predetermined height above the WGS84 ellipsoid. In order to make the band to band transform independent of height, a planar surface is desired. Therefore the average elevation of the region being processed is used as the intersection elevation (obtained from the AGP). This intersection is performed by scaling the unit look vector from the instrument

camera pixel to the earth ellipsoid. Once the intersection point is known, the latitude, longitude, sun zenith cosine, relative azimuth, sun distance, and surface classification are retrieved. Then the latitude and longitude with conjunction with the time of acquisition are used to calculate the infrared band image coordinates via IPI. This procedure is shown diagrammatically in Figure 19.

Once the tie points are determined, a band to band transform is generated using the same model as the terrain band to band transform described in Section 4.3.6.

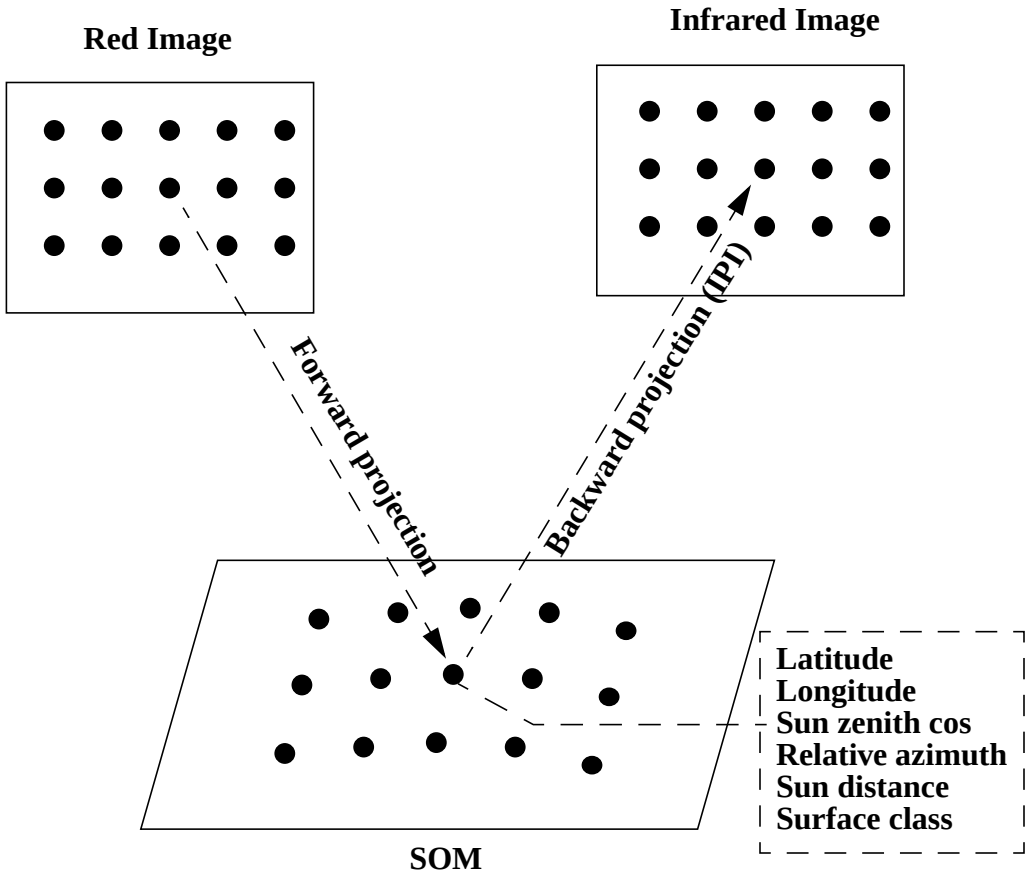

Figure 19: Diagram of process by which red band image points are geolocated and registered to their associated infrared band coordinates.

For each pixel in the red band image, the infrared radiance is retrieved using the band to band transform and bilinear interpolation. The surface parameters are retrieved from those determined for the nearest tie point. This is a simple procedure due to the regular spacing of the tie points in the red image. Estimating surface parameters in this manner is sufficient because the zenith cosine and surface class are extremely slow varying in relation to the size of the red band image, and the

relative azimuth varies by about one degree between tie points in the y axis (assuming 100 pixels in y direction between tie points) with a generous 15 degree binning scheme. Then the primary observables for land (L) and water (W) are calculated as described in [M-9]. The surface classification used in calculating the land observable is obtained by calculating the nearest land class to the earth point. This is done by finding the CSSC element for the pixel and searching all adjacent neighbors for the first land class in order of distance from the tie point geodetic coordinates (a 3x3 search window). If no land class is found within this window then it is assumed that the point is over water.

Once W and L are determined, a two step process is used to classify the pixel as cloudy or clear. The RC thresholds described in [M-9] specify a threshold T2 for the primary observable that separates clear low confidence from cloud low confidence observables. These thresholds are dependent upon surface class, sun zenith angle cosine, and relative azimuth angle. Then if $W < W_t$, where W_t is the RC threshold T2 for water classes, then flag the pixel as clear. If $W \quad W_t$, then check the land observable. If $L > L_t$, where L_t is the RC threshold T2 for the nearest land class, then flag the pixel as clear, otherwise flag the pixel as cloudy. Note that if no land class was found in the 3x3 search window and $W \quad W_t$, then flag the pixel as cloudy. A complete explanation of this two step threshold procedure is described in [4].

4.3.2.5 Blunder detection

Introduction

The transform which maps reference orbit imagery and new MISR images is based on well distributed grid tie points determined by image matching or image point intersection. Any blunder in the location of these tie points will cause the transform to deviate significantly from the true mapping. The adaptive design of the processing can reduce some of these effects. If a blunder appears and causes low accuracy in an area, the program will automatically sub-grid in the area to lower levels to avoid the error propagation of the blunder to its surrounding. Nevertheless, this processing costs many more computations. One approach to avoid this situation is to adjust image matching parameters and to make image matching as reliable as possible. However, there is no guarantee that blunders can be eliminated in the processing. Therefore, a blunder detection function which evaluates each data point by studying the statistical behavior of the least-square computation for the new to reference image transform is designed to detect and remove blunders among input tie points. The fundamental concept of this blunder detector is to recursively remove blunders using statistical behavior of the deviations of the estimated fitting values from the input measurement data set, namely, the standardized residuals and the post-estimated variance per unit weight of the least-square adjustment.

Mathematical description of the algorithm

A least square computation is a process to find the best estimate of a set of unknown parameters giving a set of observations linearly related to it.

$$v = Ax - y \tag{12}$$

Where the observation y is a set of random variables, $y \sim (Y, \sigma_0^2 P_{yy}^{-1})$. $Y=Ax$ is the real value of the observation, σ_0 is the variance per unit weight of the observation, P_{yy} is the weight matrix, and $P_{yy}^{-1} = Q_{yy}$, Q_{yy} is the cofactor matrix. x is the set of unknown parameters. A is the design matrix relating x to y. Finally, v is the residual $v=y-Y$. In our case, the unknown parameters are the coefficients of the transformation from new to reference images and the observations are the new image coordinates resulted from image point intersection (IPI), image matching (IM), and previous level image transform (IT), each having different weight in the transform. An IM point has a larger weight since it is believed to be more accurate than IPI and IT points. Our goal is to find potential blunders generated during the image matching processing. The best estimated least square solution to the above linear system by minimizing $\phi = v^T P v$ leads to a normal equation:

$$\tilde{x} = (A^T P_{yy} A)^{-1} A^T P_{yy} y = Q_{xx} C \tag{13}$$

where $Q_{xx} = (A^T P_{yy} A)^{-1}$ is the cofactor matrix of the estimated unknown parameters.

The residuals of a least square solution tell us how much difference remains between the fitted solutions and the observations. The residuals and its cofactor matrix can be represented as:

$$v = A\tilde{x} - y = (AQ_{xx}A^T P_{yy} - I)y \tag{14}$$

$$Q_{vv} = (AQ_{xx}A^T P_{yy} - I)Q_{yy}(P_{yy}A^T Q_{xx}A - I) = Q_{yy} - AQ_{xx}A^T \tag{15}$$

$$v = -(Q_{vv}P_{yy})y \tag{16}$$

Equation (16) can be directly used to find out how much the errors of one or more of the observations (Δy) influence the residuals. It can be written as $v = -(Q_{vv}P_{yy})\Delta y$. Then residual vector v relates to observation-errors or blunders Δy through both P_{yy} and Q_{vv}. The residual itself does not indicate which data point contains the error, as both the weight matrix P_{yy} of observations and the configuration of the system (by design matrix A) influence the residual value. Assuming all observations have equal weight as $P_{yy} = I$, then the values of Q_{vv} is responsible for the controllability of an observation. That is: 1) a large diagonal value of Q_{vv} translates an observation error to the corresponding residual, a small diagonal value diffuses the observation error; and 2) the off-diagonal value of Q_{vv} does the opposite, i.e., a large off-diagonal value of Q_{vv} passes an

observation error to other residual than the corresponding one. This effect is caused by the high correlation among observations.

Assume there is no gross-error in observation but only random error. The mean error σ_{y_i} of observation y_i is:

$$\sigma_{y_i} = \sigma_0 \sqrt{(Q_{yy})_{ii}} = \frac{\sigma_0}{\sqrt{p_i}} \tag{17}$$

Similarly, the accuracy of the residual v_i is:

$$\sigma_{v_i} = \sigma_0 \sqrt{(Q_{vv})_{ii}} = \sigma_{y_i} \sqrt{(Q_{vv} P_{yy})_{ii}} \tag{18}$$

Therefore, the mean error of the residuals depends not only on the observation error but also on the diagonal values of $Q_{vv}P_{yy}$. If the random errors follow a normal distribution, the residuals do the same with an expectation of 0 with a variance of σ_v^2. Obviously, the standardized residuals $\bar{v}$ follows a standardized normal-distribution with expectation 0 and variance 1.

$$\bar{v}_i = \frac{v_i}{\sigma_{v_i}} \tag{19}$$

The standardized residuals are ideal for statistical testing to detect blunders as the effect of the diagonal value of Q_{vv} is reduced. Since $\bar{v}$ follows a standardized normal distribution, the null hypothesis assumes random errors and no blunders, H_0: $E\{|\bar{v}_0|\} = 0, \sigma\{|\bar{v}_0|\} = 1$. As shown in Figure 20, if a random error has a standardized residual $\bar{v}$ larger than *k*, then we would make a wrong decision as error of the 1st kind. It means we may detect a point with random error as a blunder. The probability of making an error of the 1st kind is α. α is 1% for *k*=2.56. The alternative hypothesis is H_a: $E\{|\bar{v}_a|\} \neq 0, \sigma\{|\bar{v}_a|\} = 1|_{around E\{|\bar{v}_a|\}}$ if the data set does contain a blunder. Accepting the alternative hypothesis means we eliminate all observations whose $\bar{v}_a$ are outside the range of $\pm k$. We may not detect blunders around $E\{|\bar{v}_a|\}$ which are inside of $\pm k$ and thus make a mistake as an error of the 2nd kind with probability of 1-β. In this example, the power of the test β is 79%.

As indicated before, the observations for the MISR new to reference image transform come from three sources: IM, IPI, and IT. Each observation may have a different weight. Control grid points may not be regularly distributed over the area where the transform is covered as they can be moved due to surface obscuration and cloud obscuration. Due to these factors, the removal of an individual blunder detected according to the test to the standardized residuals may not benefit to the best fit of image transform. Therefore, a simple secondary test is added to check if the removal of a blunder does contribute to the reduction of the post-estimated variance per unit weight $\hat{\sigma}_0$, which is also called the estimated standard deviation and defined according to $\phi = v^T P v$, the

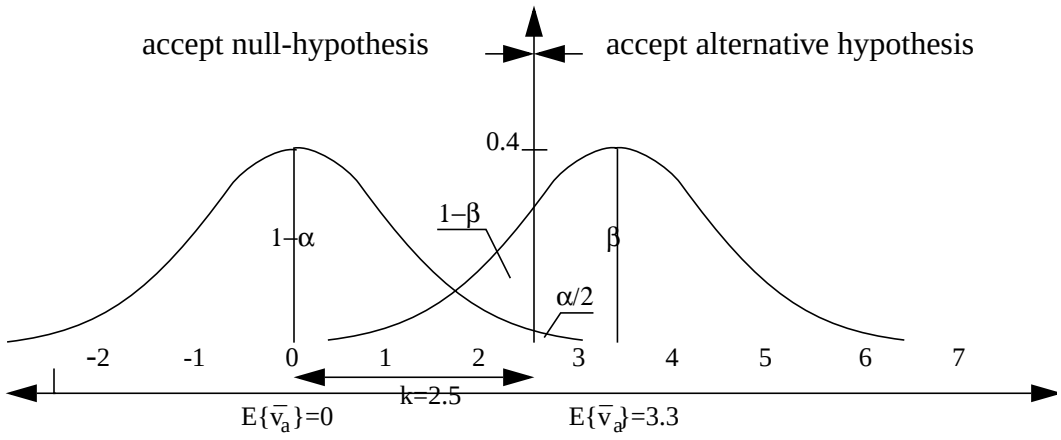

Figure 20: Statistical testing to detect a blunder in a system.

number of observation *n*, and the number of unknown parameters *m* as:

$$\hat{\sigma}_0 = \frac{v^T P v}{n - m} \tag{20}$$

The following procedures are used to detect blunders in the standard processing:

1. Compute a transform using all valid points (IPI, IT, and IM) normalized by their weight. Compute the standardized residuals $\bar{v}_i$ and the variance per unit weight $\hat{\sigma}_0$.
2. Check if max($\bar{v}_i$) is larger than a predefined blunder threshold. If so, then it is a potential blunder. Otherwise, no potential blunder is found and the rest of these steps are skipped.
.
3. Check if the number of blunders already removed has not exceeded a maximum allowable blunder number for the system and we did not successively fail in removing blunders for several iterations. If so, declare the potential blunder point as invalid. Otherwise, the detection is stopped.

4. Repeat step 1 and check if $\hat{\sigma}_{0_{i+1}} / \hat{\sigma}_{0_i}$ has dropped less then a threshold. If so, then the last removed point was indeed a blunder, and we continue testing with step 2. Otherwise, the last removed point was not a blunder, we set the point flag back to valid again and continue testing with step 2.

4.3.3 Resampling

4.3.3.1 Introduction

Once the map grid center points are located in the new MISR imagery through the process of image-to-image registration a radiance value obtained from the surrounding MISR pixel needs to be assigned to that map grid center. In addition, quality flags associated with the MISR pixels need to be included in this process so that the best estimate of the resampled radiance can be made. The quality flags will not only be used as weighting factors during resampling but will also be propagated so that quality information can be associated with the resampled radiance.

4.3.3.2 Mathematical description of the algorithm

This algorithm should be implemented on an entire grid cell region. The input elements are: a) new MISR image, b) locations of the map grid centers in the new MISR image and 3) Image Data Quality Indicators associated with the MISR pixels.

Bilinear interpolation is used as the basis while computing new radiance. An SOM grid point falling somewhere in the image data will have up to 4 surrounding points. For a given variable f that takes on values f_1, f_2, f_3 and f_4 at the surrounding points, the bilinear interpolated value is given by:

$$\langle f \rangle = (1 - a - b + ab) f_1 + a(1 - b) f_2 + b(1 - a) f_3 + ab f_4 \tag{21}$$

where a is the fractional distance $(0 \le a \le 1)$ of the interpolation point in cross-track direction and b is the fractional distance $(0 \le b \le 1)$ in the along the track direction, as shown in the Figure 21.

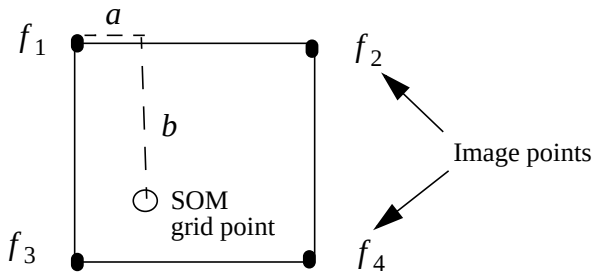

Figure 21: Bilinear interpolation

In addition to radiance values, the Image Data Quality Indicators (IDQI)need to be used for interpolation and to be propagated into Radiometric Data Quality Indicators (RDQI). The interpreta-

tion of the IDQI associated with the L1B1 Radiometric Product will take on three values: 3 = radiance is missing; 2 = radiance is available but not usable and reliable; 1 = radiance is usable, but exercise caution because one or more instrument specification is violated (e.g. signal-to-noise ratio); 0 = all specifications are met. Now, the $RDQI$ will be obtained using (21), where the f's take on the values of the $IDQI$'s of the individual image points. The obtained results will be scaled to a 2 bits value Accordingly, a sample $RDQI$ can take on values 0 to 3, where value 0 indicates the best possible radiometric quality. The four bits of the $RDQI$ should be pack along with the radiance into a 16 bit data type.

For interpolated radiance value $\langle L \rangle$, the proposed algorithm is:

$$\langle L \rangle = \frac{\langle L \cdot \overline{IDQI} \rangle}{\langle \overline{IDQI} \rangle} \tag{22}$$

where $\overline{IDQI} = 3 - IDQI$ and the f's in the numerator take on the values which are the product of the radiance at the image point and the $\overline{IDQI}$ at that image point. Thus, the resulting interpolated radiance take into account the data quality at each of the grid points as well as the distance of the SOM grid point from the individual image points. The equation is well defined for up to three unusable radiance values. If all four radiance values are unusable, $\langle \overline{IDQI} \rangle = 0$ and interpolated radiance is simply assigned fill value.

4.3.4 Image Point Intersection (IPI) algorithm

4.3.4.1 Introduction

Section 4.3.2.1 described the use of a rigorous ground-to-image projection. An image point intersection (IPI) algorithm will be used to compute the image coordinates (line, sample) of a specific ground point, given its coordinates in the Conventional Terrestrial Reference (CTR) system, and the approximate time t_0 when the point is observed by one of the nine MISR cameras. This algorithm will utilize the photogrammetric collinearity condition in order to establish the relationship between ground and image coordinates of a point.

The parameters describing the exterior orientation of the camera at the time of image acquisition are needed as input to the collinearity equations. Those parameters define the position of the camera and the orientation of its axes relative to the object space coordinate system (i.e., CTR). The MISR push-broom line-array sensor, mounted on the spacecraft, is moving through space, and each line of the retrieved image is observed at a different time. Consequently, the exterior orientation of each line is different, so that each line can be treated as a separate image with only one dimension in the direction of the array of CCD detectors. However, since the sensor is mounted on the spacecraft with known behavior relative to time we will develop an orbital version of the collinearity equations which will exploit the fact that the exterior orientation parameters of the consecutive lines are time dependent. Then our problem is to find the time at which the collinearity condition is satisfied (i.e., the time at which the point is observed). As will be shown, the image

coordinates of the observed point can be easily computed once the accurate time of the acquisition is obtained.

4.3.4.2 Mathematical description of the algorithm

This algorithm should be implemented on a point-by-point basis. The input elements are:

a) Three-dimensional ground coordinates for the point of interest. These coordinates are obtained from the Ancillary Geographic Product.
b) Approximate imaging time of the ground point.
c) Orbit navigation and attitude data obtained through the PGS toolkit.

The photogrammetric collinearity equations used in this module can be derived from the relationship between ground point position and satellite position (see Figure 22):

$$\boldsymbol{x}_g = \boldsymbol{p} + \lambda \cdot \hat{\imath} \tag{23}$$

where, $\boldsymbol{x}_g$ is the ground point of interest position vector (CTR), $\boldsymbol{p}$ is the satellite position vector (CTR), $\hat{\imath}$ is the unit vector of the ray imaging the ground point of interest (CTR), and λ is the scale factor.

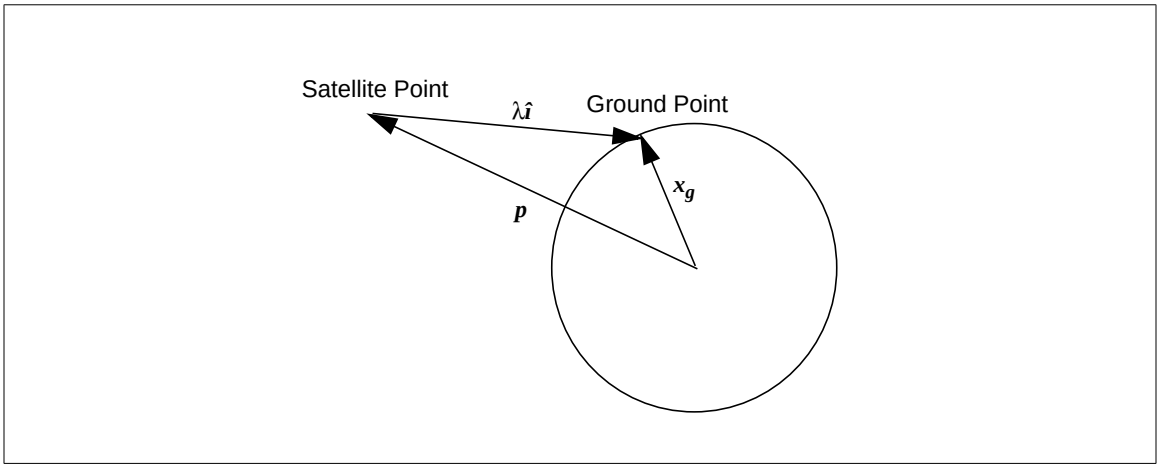

Figure 22: Relationship of ground point & satellite point

Instead of the vector $\hat{\imath}$ which is already in the CTR system we would like to relate $\boldsymbol{j}_s$, a vector in the camera system, to the object coordinate system, in our case CTR, so a number of the orthogonal rotation matrices linking different coordinate systems have to be introduced:

$$\boldsymbol{x}_g = \boldsymbol{p} + \lambda \cdot T_{co} \cdot T_{os} \cdot T_{si} \cdot \boldsymbol{j}_s \tag{24}$$

The coordinate systems and rotation matrices T_{co}, T_{os} and T_{si} are explained in Appendix A.2.

$\boldsymbol{j}_s$ is the vector in the camera system representing the ray imaging the ground point, and since our camera is a one dimensional linear array the coordinate in one direction is constant, or:

$$\boldsymbol{j}_s = \begin{bmatrix} 0 - x_p \\ y - y_p \\ -f \end{bmatrix} \tag{25}$$

where x_p and y_p are the coordinates of the camera principal point and f is the focal length of the camera, and y is the image coordinate (sample). However, in addition to x_p, y_p and f, camera constants resulting from camera calibration will be appropriately included in the right-hand side of (25) in order to account for various camera distortions.

The orthogonal matrix T_{os} is used to account for the spacecraft attitude changes which are time dependent. So, we will have attitude angles in the form:

$$\begin{aligned} \Omega(t) &= \Omega_0 + a_1 \cdot dt + a_2 \cdot dt^2 + \ldots \\ \Psi(t) &= \Psi_0 + b_1 \cdot dt + b_2 \cdot dt^2 + \ldots \\ \mathrm{K}(t) &= \mathrm{K}_0 + c_1 \cdot dt + c_2 \cdot dt^2 + \ldots \end{aligned} \tag{26}$$

where Ω_0, Ψ_0 and K_0 are the roll, pitch, and yaw bias at time t_0 and $dt = t - t_0$ is the time difference that we are going to solve for. The biases as well as the coefficients (a_1, a_2, b_1 ...) will be derived from the attitude angles and attitude rates information which is part of the spacecraft navigation data set.

Also, the rotational orthogonal matrix T_{co} between the local orbital coordinate system and the CTR system is directly dependent on the spacecraft position and velocity vectors ($\boldsymbol{p}$, $\boldsymbol{v}$) given in the CTR. Moreover, the vectors $\boldsymbol{p}$ and $\boldsymbol{v}$ are functions of time, and in order to find them at any time t given the spacecraft position and velocity ($\boldsymbol{p}_0$, $\boldsymbol{v}_0$) at time t_0 and the time difference $dt = t - t_0$, we will use Herick's non-singular solution of the elliptic two-body problem. Since this solution uses an inertial coordinate system, correction due to Earth rotation in time dt has to be applied, as follows:

$$\left[\boldsymbol{p}\ \boldsymbol{v}\right]_{CTR(t)} = \begin{bmatrix} \cos\varpi & \sin\varpi & 0 \\ -\sin\varpi & \cos\varpi & 0 \\ 0 & 0 & 1 \end{bmatrix} \times \left[\boldsymbol{p}\ \boldsymbol{v}\right]_{CTR(t_0)} \tag{27}$$

where ϖ is the angle of rotation equal to $dt \cdot \omega$, where $dt = t - t_0$ and ω is the angular velocity of the Earth.

It should be pointed out that $\boldsymbol{p}_0$ and $\boldsymbol{v}_0$ at time t_0 are originally given in a Geocentric Inertial (GCI) coordinate system of epoch J2000. In order to be used in our algorithm, they must be transformed to the CTR system. More precisely, a set of transformations to account for precession, nutation, Earth rotation, and polar motion need to be applied a priori. These transformations are explained in more detail in [20].

With reference to (24), since the rotation matrices are orthogonal, by simple manipulation the image coordinates can be expressed as a function of the camera exterior orientation and ground point coordinates:

$$\boldsymbol{j}_s = \lambda^{-1} \cdot (T_{si}{}^T \cdot T_{os}{}^T \cdot T_{co}{}^T) \cdot [\boldsymbol{x}_g - \boldsymbol{p}] \tag{28}$$

For convenience, by further multiplying on the right hand side of (28) we get:

$$\boldsymbol{j}_s = \lambda^{-1} \cdot \begin{bmatrix} u \\ v \\ w \end{bmatrix} \tag{29}$$

Dividing the first and second rows of (29) by its third row we obtain two collinearity equations as follows:

$$\begin{aligned} 0 - x_{const} &= -f \cdot \frac{u}{w} \\ y - y_{const} &= -f \cdot \frac{v}{w} \end{aligned} \tag{30}$$

The elements *u*, *v* and *w* are time dependent and the first equation of (30) will be used in a one dimensional root finding method (Newton-Raphson described in [31], for instance) to solve for the time when the ground point of interest is observed. The line coordinates are directly related to time *t* by the magnitude of the sampling interval. Then, by evaluating the second collinearity equation of (30) the sample coordinate will be found.

4.3.5 Image matching between reference and new MISR images

4.3.5.1 Introduction

An image matching technique has been chosen for use during standard processing in order to precisely locate the projection of a ground point to a new MISR image. The IPI algorithm described in Section 4.3.4 which utilizes navigational data to accomplish ground to image projection, or the set of transformation parameters described in Section 4.3.2.2, will be used first. Image content centered around those newly obtained image coordinates will be compared with the image content

from a reference image centered around the projection of the same ground point. The goal is to find the correction which will account for the unpredictable errors in navigational data or the errors in the interpolation parameters, depending upon what algorithm was used initially. This correction will then be applied to the position of the point in the new MISR image.

It is common to divide matching algorithms into two categories: feature-based and area-based. In each of these two approaches a similarity measure is obtained between two images. In feature-based matching the distinct features in both images (point, line, shape) are detected first, then the similarity between the features is measured. An area-based image matching technique considers image patches or pixel neighborhoods as primitives to be matched by measuring the similarity using pixel gray level values. The decision to use an area-based matching algorithm is based largely on two factors. First, such an algorithm has been proven to perform well (see [10]) if there is only a small perspective change between the views of the two image patches and if an assumption that there is only a shift between these two views is valid. MISR new and reference images with nominally the same viewing geometry will serve as very good input to area-based matching with regard to these requirements. Second, as was stated previously, the feature-based algorithm needs to detect a well defined feature in the area that will be matched. In our case (see Section 4.3.2.1), we will want to be able to do matching on any area of the image. Location of a feature to high accuracy, with uncertainty better than 0.2 of pixel, anywhere in an image in order to do accurate matching, with uncertainty better than 0.5 of pixel, has been demonstrated to be a difficult task (see [13]).

The goal is to achieve the requirements stated in the MISR DSSR which, at 95% confidence, are: geolocating nadir imagery with ± 275 m uncertainty in both the cross-track and down-track directions and co-registering images from nine cameras with uncertainties of ± 275 m cross-track and ± 550 m down-track (this statement of the requirements incorporates the effects of terrain relief). These requirements call for a high subpixel accuracy matching technique with uncertainty better than 0.5 of a pixel. For that reason an area-based Least Squares Correlation (LSC) method is used (see [32]). A cross-correlation technique will be used as an initial step in order to provide a good first approximation needed by LSC.

4.3.5.2 Mathematical description of the algorithm

This algorithm will be implemented on a point by point basis. The input elements to the algorithm are: a) location of the ground point in the ROI, and b) initial location of the ground point in the new MISR image.

Step 1: Cross-Correlation

At first an image patch, called a template window, in the reference image and an image patch, called a target window, in the new image are selected so that they are centered at the projections of the ground point of interest in those two images respectively. The template window is shifted pixel by pixel over the larger target window and similarity is measured using gray level values of

the common pixels. The target window is larger than the template to allow for sufficient search space. How much larger depends upon the accuracy of the method used to project the ground point to the new image. Since we used either an image point intersection or previously computed transformation parameters, the error in the point prediction is expected to be between 3 and 11 pixels depending on the camera angle and method use to get initial guess. So, if the size of the template window is equal to 9×9 the maximum size of the target window would be 20×20. As the similarity measure we will use the square of the normalized cross-correlation (see [10]) as follows:

$$C = \frac{\sigma_{12} \cdot |\sigma_{12}|}{\sigma_1^2 \cdot \sigma_2^2} \tag{31}$$

where σ_{12} is the covariance between the template window and the corresponding area in the target window, σ_1 is the variance in the template window, and σ_2 is the variance in the corresponding area in the target window.

Note that the sign of the covariance between the two windows is preserved in (31).

The mid-pixel of the target window with the largest similarity value *C* is taken as the best match and will be considered as the corrected location of the point in the new image. However, before this match is accepted, the value *C* will be tested against an absolute threshold value. Where this test fails we will not correct the point location established prior to the matching and we will not do LSC at that point.

Step 2: Least-Squares Correlation

The LSC uses target and template windows of the same size. The target window is now centered at the newly obtained point location found in the previous cross-correlation step. That location will be refined even further. In the LSC method the geometric and radiometric transformations between two image windows are estimated by minimizing certain functions between both images. Then, an estimated set of geometric transformation parameters will be applied to obtain coordinates of the point in the target given its coordinates in the template window. As commonly described in [1] and [9], an affine linear transformation is used to model the geometric relationship between the windows:

$$\begin{aligned} x'' &= F_x(x', y') = a_0 + a_1 \cdot x' + a_2 \cdot y' \\ y'' &= F_y(x', y') = a_3 + a_4 \cdot x' + a_5 \cdot y' \end{aligned} \tag{32}$$

where x' and y' are the image coordinates of the chosen point in the template window, x'' and y'' are the image coordinates of the corresponding point in the target window, and a_0, a_1,..., a_5 are the geometric transformation parameters that will be estimated.

The radiometric transformation is described by a 2-parameter linear function:

$$g' = F_r(g'') = k_0 + k_1 \cdot g'' \tag{33}$$

where:

$$\begin{aligned} g'' &= G''(x'', y'') + n''(x'', y'') \\ g' &= G'(x', y') + n'(x', y') \end{aligned} \tag{34}$$

g' and g'' represent the discrete radiance values for both template and target windows. G' and G'' are the image functions. $n'(x', y')$ and $n''(x'', y'')$ are the associated noise values. The parameters of the radiometric transformation k_0 and k_1, are not needed for the computation of the image coordinates in the target window but they will be estimated simultaneously with the parameters a_i in order to improve the accuracy of the estimation.

To solve for the parameters a_i and k_i, equation (33) needs to be linearized with respect to those parameters. This gives us:

$$\Delta g + \upsilon = \sum_{i=0}^{5} \left(g_x \cdot \frac{\partial F_x}{\partial a_i} + g_y \cdot \frac{\partial F_y}{\partial a_i} \right) \cdot da_i + \sum_{j=0}^{1} \frac{\partial F_r}{\partial k_j} \cdot dk_j \tag{35}$$

where g_x and g_y are the gradients of g' in the x and y directions, Δg is the difference of the observed radiance values ($g'' - g'$), and υ is the difference of the noise components ($n''(x'', y'') - n'(x', y')$).

Since we used the cross-correlation method previously to improve the location in the target window we will assume that there are no geometric differences between the two windows and set initial approximations of a_i and k_i as follows:

$$(a_0, a_1, a_2, a_3, a_4, a_5, k_0, k_1)^0 = (0, 1, 0, 0, 0, 1, 0, 1) \tag{36}$$

The image functions G' and G'' as well as the gradients g_x and g_y are not available directly, so they will be estimated from the observed gray level values. This estimation will apply a smoothing procedure in order to filter noise, but at the same time sufficient image texture changes must be preserved in order to solve for the unknown parameters [2].

For each pair of corresponding pixels in both windows, one equation is written. Then the Least Square technique is used to solve for the unknown parameters (see [23]). Since there are only 8 unknowns, target and template windows of size 20×20, for instance, will be large enough to produce a highly redundant set of the observational equations (35). The Least Squares solution of the

non-linear model must be iterated. The iterations are terminated when the changes in the parameters a_i between two successive iterations are sufficiently small. The last set of the a_i will be used to compute the final image coordinates of the point in the new MISR image given its coordinates in the reference image by evaluating (32).

4.3.6 Image registration of the green, blue and infrared band

4.3.6.1 Introduction

In this section the magnitude of the band to band miss-registration resulting from the specific layout of the four CCD line-array in the camera focal plane will be shown first. Then, mathematical models intended to remove this displacement will be described. An error analysis focusing on the deficiency of the simplified model will follow. Finally, implementation of band to band registration algorithm will be discussed, along with obtained test results.

4.3.6.2 Magnitude of the band to band misregistration

In order to provide imagery in four spectral bands, each MISR camera uses four CCD line arrays in a single focal plane. Figure 46 (Appendix A) illustrates displacement of these line arrays relative to detector coordinate system. Nominally, camera boresight is located half way between green and red band, and the separation between adjacent bands is 160 microns. This kind of camera design will result in band to band misregistration which is characterized by two values called line-parallax and sample-parallax. Since the lines of imagery are separated by a time interval of 40.8 ms, line-parallax is the direct result of the time difference between imaging a ground point in two different bands. Sample-parallax represent differences in the sample coordinates (i.e., in the direction across the band) of the same ground point projected to the imagery corresponding to the different bands.

The following figures show the magnitude of the line parallax and sample parallax for two different cameras. In order to compute those parallaxes we used simulated navigation data, nominal geometry of the cameras, and surface topography represented by a DEM. At first, a forward projection of the rays corresponding to band 3 (we chose it to be our reference band) is performed in order to find ground points seen at known line and sample coordinates in the imagery representing band 3. Then, a backward projection (e.g., IPI) for a band of interest (band 1 in our examples) is performed in order to find line and sample coordinates of the same ground points now projected to the imagery representing the band of interest.

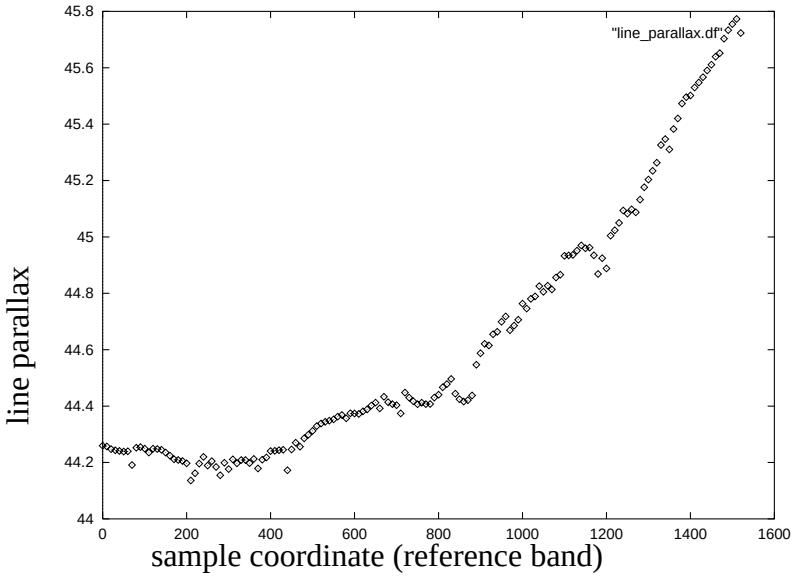

Figure 23: Line parallax, Df camera

Differences between known line and sample coordinates of band 3 and the computed line and sample coordinates of band 1 are plotted in our diagrams as the line and sample parallaxes respectively. They are plotted against sample coordinates of the reference band and only for the one line of the reference band.

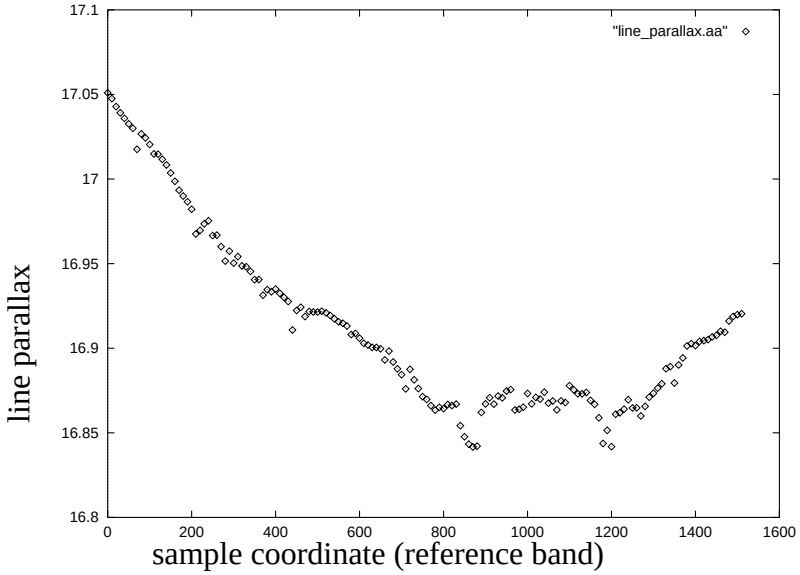

Figure 24: Line Parallax, Aa camera

It can be seen from Figure 23 and Figure 24 that line parallax is significant and is mostly a function of the camera type and some other parameters which must be taken into account if we want to remove the parallax during standard processing. It is interesting to notice how the different direction and size of pitch and roll angles associated with the for and aft cameras impact the size and distribution of the line parallax along a line (e.g., slant of the plot is the function of the roll angle).

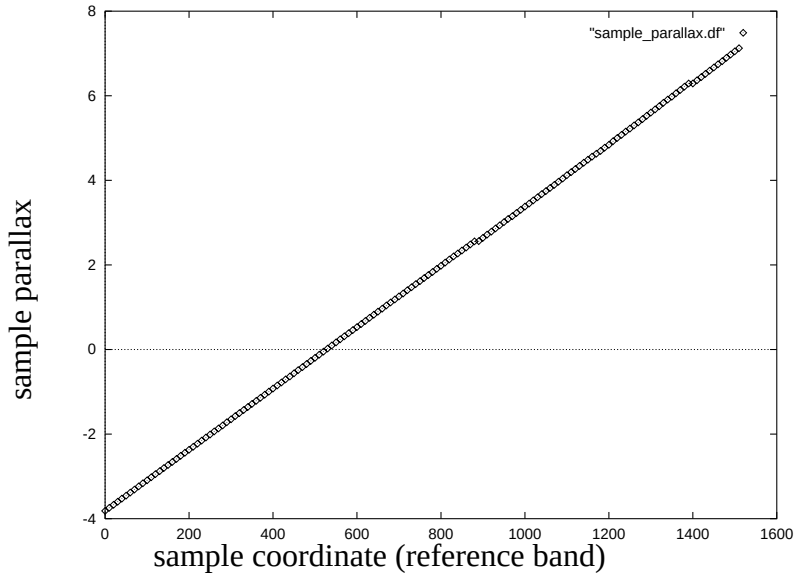

Figure 25: Sample parallax, Df Camera

Similarly, sample parallax is significant and depends on the camera type and other parameters. The goal is to remove these parallaxes with the minimum use of data storage and processing time and still satisfy geolocation and co-registration requirements. In the next section we describe our approach.

4.3.6.3 Simplified mathematical models intended to remove line and sample parallaxes

During image-to-image registration of the red band (i.e. reference band), ground points representing map grid centers are accurately (navigation and attitude errors taken into account) located in this reference band. In order to minimize data storage and processing time during band-to-band registration but still preserve accuracy of the registration the results of the red band geolocation will be used. In another word the objective is a simple model which will compute parallaxes only. Computation of the line parallax is treated independent from the computation of the sample parallax.

Line parallax

Intuitively and by looking at the previous plots we expect that line parallax depends on the camera type (e.g., camera geometry), sample coordinates, and surface topography (irregularities in the plot). At the beginning we will ignore the last two factors by computing parallax for a single ground point which is a subspacecraft point located at a fixed height H from the Earth's surface. Subsequently those factors will be included in the computation. It should be pointed out that we make following assumptions: spherical Earth, circular orbit, and no attitude change during the time corresponding to the line parallax.

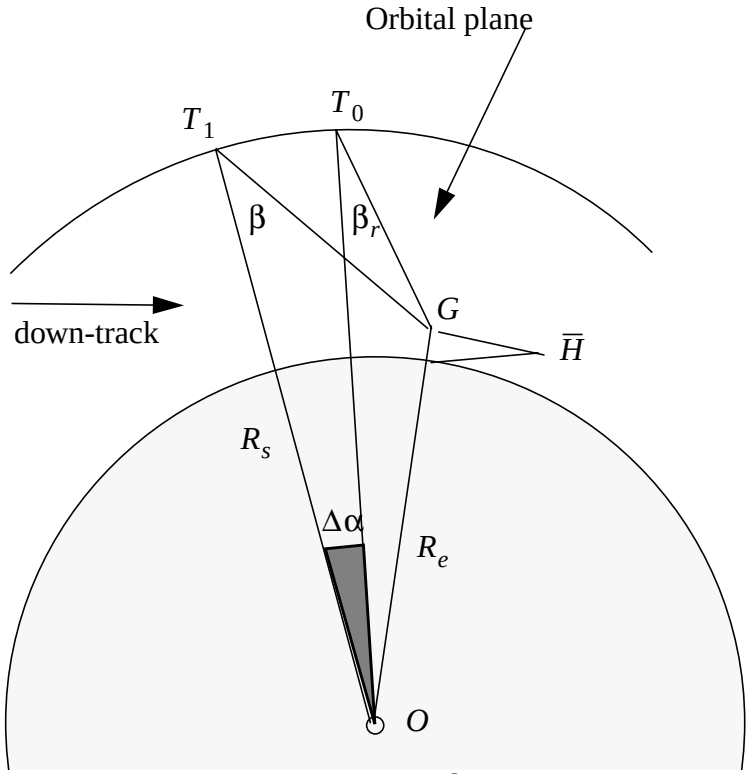

R_s - orbit radius

R_e - Earth radius

$\bar{H}$ - ground point height projected to the orbital plane

β_r - off nadir view angle reference band 3

β - off nadir view angle band of interest

Figure 26: Simplified geometry illustrating line parallax

From the Figure 26 we get that:

$$\Delta\alpha = \beta - \beta_r - \text{asin}\left(\left(\frac{R_s}{R_e + \bar{H}}\right)\sin\beta\right) + \text{asin}\left(\left(\frac{R_{sr}}{R_e + \bar{H}}\right)\sin\beta_r\right) \tag{37}$$

Through "Kepler's modified equation" (reference [12]) line parallax Δl can be related to the angle $\Delta\alpha$ through,

$$\Delta l = \frac{\sqrt{\frac{a^3}{\mu}}}{t_l}\left(\Delta\alpha - \left(1 - \frac{R_s}{a}\right)(\sin\Delta\alpha) + \frac{(r \cdot v)}{\sqrt{\mu a}}(1 - \cos\Delta\alpha)\right) \tag{38}$$

where a = orbit semi major axis, r and v are spacecraft radius and velocity vectors, μ = Earth gravitational-mass constant, and t_l = time interval between recorded lines. With the assumption that the orbit is circular, equation (38) is simple,

$$\Delta l = C_{11}\Delta\alpha + Error1 \tag{39}$$

where C_{11} is constant. By combining (39) and (37) and expanding the Taylor series with the variable $X = \frac{R_s}{R_e + H}$ we get the relation

$$\Delta l = C_{21} + C_{22}(X) + \ldots Error2 \tag{40}$$

The coefficients C_{21} and C_{22} can be estimated through a least-square fit (see Section 4.3.6.5) and then used in the computation of line parallax.

Corrected Height $\bar{H}$

The Equation (40) requires knowledge of $\bar{H}$, which is the ground height ortho-projected to the orbital plane. Figure 27 illustrates geometry which can be used if one wants to compute corrected height given the sample number and height H.

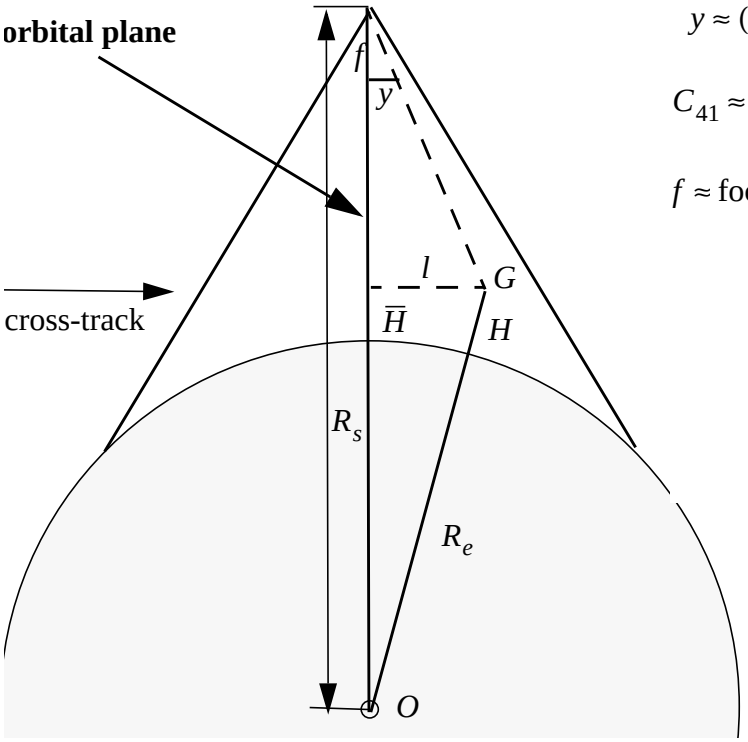

$y \approx (sample - C_{41})$

$C_{41} \approx 752.0$ (nadir cam)

$f \approx$ focal length (reference band)

Figure 27: Height correction

We start with two relations for l

$$l = \frac{y}{f}(R_s - R_e - \bar{H}), \tag{41}$$

$$l^2 = (R_e + H)^2 - (R_e + \bar{H})^2 \tag{42}$$

Combining (41) and (42) and solving the quadratic equation (smaller of the two possible solutions) we find that $\bar{H}$ is,

$$\overline{H} = \frac{\left\{\frac{y^2}{f^2}R_s - 2\sqrt{\frac{y^2}{f^2}(R_e + H + R_s{}^2) - (R_e + H)}\right\}}{\frac{y^2}{f^2} - 1} - R_e \tag{43}$$

One may consider the use of equation (43) in our production software. However, some of the relations (e.g., $y \leftrightarrow sample$) due to the roll and pitch angles are not taken into account analytically. In addition, we would like to avoid redundant processing. Therefore, we expand [43] to a Taylor series with variables height and sample coordinates and pre-estimate necessary parameters. The relation [43] now can also be used to analyze our sensitivity to various assumptions. The linearized form that may be adapted for our production looks like, (s = sample)

$$\overline{H} = C_{31} + C_{32}H + C_{33}(s - C_{41}) + C_{34}(s - C_{41})H + C_{35}(s - C_{41})^2 + C_{36}H(s - C_{41})^2 \tag{44}$$

In summary, the equation to compute the line coordinate of band $\dot{l}$ given line and sample coordinates of the reference band l, s and ground point height H looks like.

$$\dot{l} = l + C_{21} + C_{22}\left(\frac{R_s}{R_e + C_{31} + C_{32}H + C_{33}(s - C_{41}) + C_{34}(s - C_{41})H + C_{35}(s - C_{41})^2 + C_{36}H(s - C_{41})^2}\right) \tag{45}$$

(46)

Sample parallax

The sample parallax is a result of: 1) scaling between the reference band and the band of interest due to the different IFOV, 2) a shift due to a small roll angle, 3) a shift due to Earth rotation. These effects can be modeled as the linear scaling plus shift,

$$\overline{sample} = D_{11} + D_{12}sample \tag{47}$$

The coefficients D_{11}, and D_{12} can be pre-estimated through least-square fit. However, the shift due to Earth rotation varies with latitude and that variability can be important in defining the optimum length of the orbit on which one set of parameters can be applied. A simple equation is used for that purpose,

$$\Delta d = a\omega_e T_i(1.0 - \cos\lambda) \tag{48}$$

where, λ is latitude, ω_e is Earth angular velocity, and T_i is average the time difference between

two bands.

4.3.6.4 Sensitivity and errors

In the previous section we presented simplified relations which can be used as the basis for the band-to-band registration process. Before proposing a processing solution we would like to estimate the maximum size of the systematic error resulting from the deficiency of our simplified model.

The only significant source of error in regards to the computation of the sample coordinates is the spacecraft attitude error. During the period of 1.9 sec (i.e., the maximum time difference between bands for D camera) and based on the current specifications the attitude error should not result in more than 0.3 of the size of pixel in the sample direction. The Earth's rotation has insignificant impact on the accuracy of sample coordinates even when one pair of coefficients is used for 10,000 lines of image data.

The estimate of the errors in the line coordinates is a bit more complex. In this analysis we consider effects of the following systematic errors: 1) error in the height projected to the orbital plane, 2) Earth radius error, 3) Orbit radius error (total), 4) Orbit radius error (fractional, only during the time difference between bands), 5) spacecraft pitch attitude error (total), and 6) spacecraft pitch error (fractional, only during the time difference between bands). In order to compute errors we first compute the sensitivity of our model with respect to certain parameter representing the source of the systematic errors. Then we assume a size of the disparity in that parameters and multiply it by the sensitivity to get the contributing error of that parameter. The sensitivities are computed as partial derivatives considering equations (37), (38), and (43). Two additional parameters ΔR_s, and $\Delta\beta$ will represent sources of the systematic errors 4) and 6) and when included into equation (37) it becomes:

$$\Delta\alpha = \beta - (\beta + \Delta\beta) - \text{asin}\left(\left(\frac{R_s}{R_e + H}\right)\sin\beta\right) + \text{asin}\left(\left(\frac{(R_s + \Delta R_s)}{R_e + H}\right)\sin(\beta + \Delta\beta)\right) \qquad (49)$$

The Table 6 lists the sensitivities for the D and A cameras considering registration between bands 1 and 3.

Table 6: Sensitivities of the line parallax model

par/ cam	$\overline{H}$ (line / m)	R_e (line / m)	R_s (line / m)	ΔR_s (line / m)	β (line / arc-sec)	$\Delta\beta_s$ (line / arc-sec)
Af	0.000028	0.000055	0.000055	0.001650	0.000086	0.015186

Table 6: Sensitivities of the line parallax model

Df	0.000146	0.000291	0.000283	0.009392	0.001680	0.085055

Disparities in the listed parameters will depend on the processing scenario. The following two cases are relevant to accurate band-to-band registration at the end of L1B2 processing:

Case A: We assume spherical Earth and circular orbit only for the time interval representing the time difference between bands. That would mean that Earth and orbit radius are computed for each point, using navigation data, but only for the reference band with the assumption that they are the same in the other bands.

Case B: We assume spherical Earth and circular orbit for a larger period of time, corresponding to about 8000 line. That would mean that Earth and orbit radius are computed only once, using navigation data, for the point in the middle of the selected region and then applied to all points in that region.

In both cases we:

a) treat sensitivities as constants (it is correct for the domain of parameter changes)
b) take orbit radius error (total) and attitude pitch error (total) from the current specifications
d) compute Earth radius error (fractional) and orbit radius error (fractional) as the disparity between the radius and semi-major axis of the proper ellipse after a time interval
c) take attitude pitch error from the current specifications

Table 7 lists the contributing systematic errors for the two cases.

Table 7: Systematic errors

Case A:						
par/cam	$\varepsilon\overline{H}$ = 1000.0 m	εR_e = 0.0 m	εR_s = 160.0 m	ΔR_s = 0.02 m	$\varepsilon\beta$ = 150 arc-sec	$\varepsilon\Delta\beta_s$ = 4 arc-sec
Af error (line)	0.028	0.00000	0.008800	0.000033	0.012900	0.0607440
Df error (line)	0.146	0.00000	0.000000	0.000187	0.252000	0.3402200
Case B:						
par/cam	$\varepsilon\overline{H}$ = 1000.0 m	εR_e = 700.0 m	εR_s = 160.0 m	ΔR_s = 0.02 m	$\varepsilon\beta$ = 150 arc-sec	$\varepsilon\Delta\beta_s$ = 4 arc-sec
Af error (line)	0.028	0.038500	0.008800	0.000033	0.012900	0.0607440

Table 7: Systematic errors

Df error (line)	0.146	0.203700	0.04528	0.000187	0.252000	0.3402200

From Table 7 we make several conclusions:

- The major source of error is the attitude stability (pitch angle, $\varepsilon\Delta\beta_s$).
- The attitude accuracy effect ($\varepsilon\beta$) limits our capability to pre-estimate transformation coefficients only once, using nominal orbit data. Instead, we will compute them dynamically.
- The Earth effect (εR_e) limits the size of the orbit segment for which one set of coefficients can be applied.

While case A and case B are applicable to accurate band to band registration as part of the L1B2 process, a special situation may arise if the preliminary band-to-band registration is required by the clear-sky mask algorithm. In that case the predominant error source would be height error, since the height of the cloud would be unknown at this point. The sensitivities of line coordinate computations to height error for the A, B, C, and D cameras are listed in the Table 8

Table 8: Height sensitivities

camera	A	B	C	D
sensitivity (line / km)	0.028	0.039	0.068	0.146

4.3.6.5 A proposed solution

Based on the results from the previous section we have concluded that band-to-band registration is possible without additional image matching or huge data sets. Models that we would like to use are sufficiently good given the registration requirements. Errors due to linearization were also computed and found to be insignificant. Based on Earth radius variations the optimum size of the orbit segment for which one set of coefficients can be applied is chosen to be 4000 lines. A case B scenario is proposed with computation of most of the coefficients on the fly. The algorithm should flow in this order:

1. Compute height coefficient C_{41} (see Figure 27 and equation (44)) for each of the nine cameras.

The coefficients are computed by projecting the sub-spacecraft ground point back to the camera space. The sample coordinate of that point is equal C_{41} for that camera. This needs to be computed only once with the nominal orbit and camera parameters. The table below lists the coefficients for each camera.

Table 9: Coefficients C_{41}

Df	Cf	Bf	Af	An	Aa	Ba	Ca	Da
485.0	574.0	649.0	702.0	752.0	801.0	856.0	934.0	1027.0

2. Compute height coefficients $C_{31} - C_{36}$ (see equation (44))

In order to compute these coefficients we choose about 50 image points evenly distributed throughout the orbit segment. They are projected to intersect with the ellipsoid (using supplied navigation data) with the height values H being random numbers from the range of values approximately within the equal range of real surface height. These values are then projected to the orbital plane, defined by the nadir camera geometry and time, and corrected heights $\overline{H}$ are computed. The H -$\overline{H}$ pairs and associated sample number along with the coefficient C_{41} for that camera are used to estimate coefficients $C_{31} - C_{36}$ through linear least-squares fit. The table below list the coefficients for the Df and Aa camera.

Table 10: Height coefficients

	C_{31}	C_{32}	C_{33}	C_{34}	C_{35}	C_{36}
Df	-7128.4126	0.992801	-13.052430	0.000045	-0.006446	0.00007
Aa	-974.1001	1.000874	4.902949	-0.000006	-0.006126	0.00000

Some of these parameters may not need to be estimated, we can focus on that in the future.

3. Compute line coefficients C_{21} and C_{22} (see equation (40))

First steps of this computation are similar to the ones in part 2 (i.e., in order to compute these coefficients we choose about 50 image points evenly distributed throughout the orbit segment. They are projected to intersect with the ellipsoid (using supplied navigation data) with the height values being random numbers from the range of values approximately within the range of the real surface height). Then a backward projection (IPI) is applied at each point, using camera parameters describing the band that we want to register, and line parallaxes Δl are computed. Also, spacecraft and Earth radius are computed at each point. Before going to the least-square estimate of the needed coefficients we will compute corrected height at each point using coefficients esti-

mated in parts 2 and 1. The table below list the coefficients for Df and Aa camera.

Table 11: Line Coefficients

	C_{21}	C_{22}
Df	-349.24365	353.914224
Aa	-115.59179	119.21293

4. Band-to-band registration (line)

Using previously estimated coefficients (Tables 9, 10, and11) and equation (45) we will compute line parallax for the points on the SOM grid in order to register band to band. The Earth radius and spacecraft radius need to be computed only once at the mid point of the orbit segment. The height values are available only on 1.1 km resolution which is sufficient.

5. Computation of sample coefficients and sample coordinates.

The procedures in this part are very similar to the procedures in the previously described parts and no details will be described. Table 12 lists the values of the sample coefficients and Figures 30, and 31 are plots of errors in the sample coordinates throughout the selected orbit segment after registering band 1 to band 3.

Table 12: Sample Coefficients

	D_{11}	D_{12}
Df	-3.613546	1.007286
Aa	2.156851	0.997340

4.3.6.6 The test results

The Figures 28,29,30, and 31 present the results of tests which used the above-described method for the band-to-band registration. The errors shown in our test results are a reflection of our understanding of accuracy and knowledge errors associated with the supplied navigation data. A so called “nominal case” for the simulation of the supplied navigation data is used. In that case frequency of knowledge errors is highly exaggerated. That is reflected in a slightly wider spread than expected of errors in the line coordinates for camera Df. Nevertheless, our conclusion is that band-to-band registration can be done on the fly without image matching and staged data sets using the proposed method.

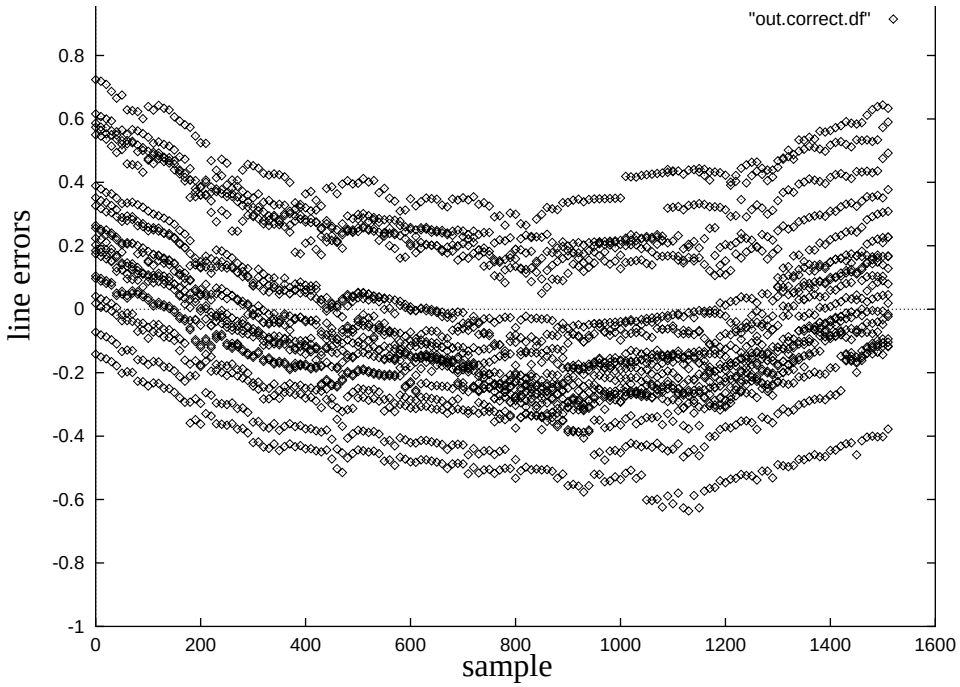

Figure 28: Errors in the line coordinates (Df, band 1)

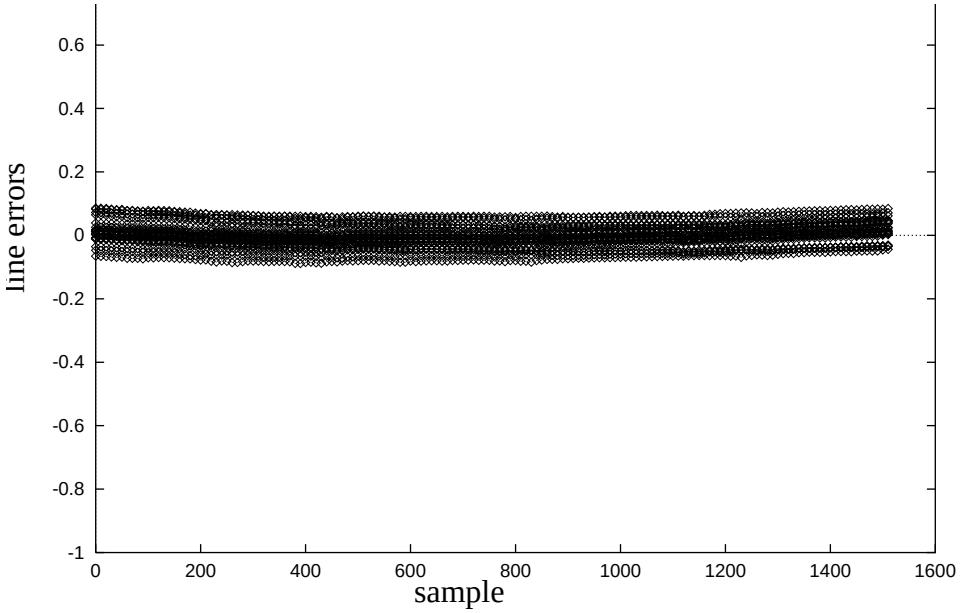

Figure 29: Error in the line coordinate (Aa, band 1)

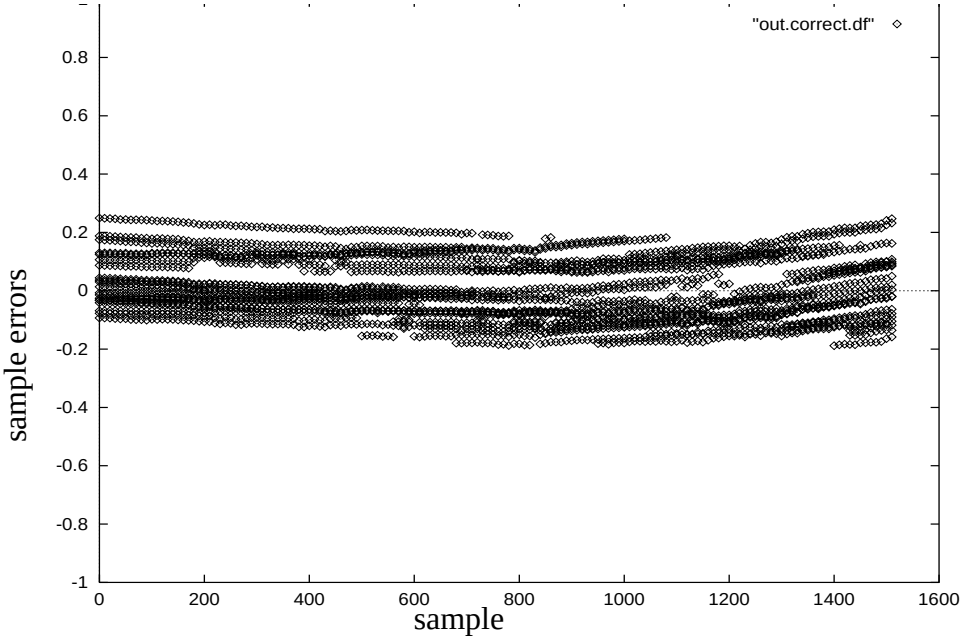

Figure 30: Errors in the sample coordinates (Df, band 1)

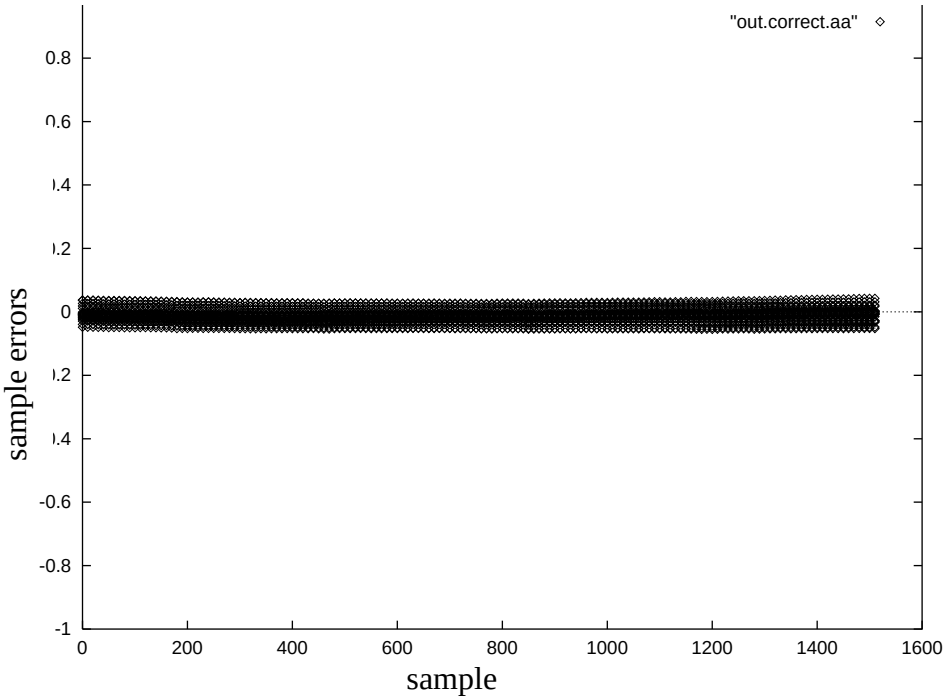

Figure 31: Errors in the sample coordinates (Aa, band 1)

5.0 ELLIPSOID-PROJECTION ALGORITHM

5.1 ALGORITHM SUMMARY

In the ellipsoid-projection algorithm, a new MISR image is projected to a predefined SOM projection, based on the reference WGS84 ellipsoid. There are two steps to the algorithm. First, we rectify the new MISR image to the surface of the ellipsoid making use of navigation data and the calibrated camera model. Second, we resample the rectified image to the predefined SOM grid by using a distance weighted average of the neighbors in the rectified image nearest a grid point.

5.2 ALGORITHM INPUTS

5.2.1 MISR data

Required input for the ellipsoid product to be obtained for MISR are summarized in Table 13. Further information on each of the inputs is provided below.

Table 13: Level 1B2 Product MISR Data Inputs

Input data	Source of data
MISR radiance imagery	MISR Level 1B1

5.2.1.1 MISR radiance imagery

The MISR radiance imagery is derived at Level 1B1 and consists of the calibrated radiances in all 36 channels of the instrument. These radiances have not had any atmospheric correction applied and include both surface and atmospheric contributions to the signal.

The process for calibrating the radiance values is described in the MISR Level 1B1 ATB. The format of the Level 1B1 product containing these radiance values is described in the MISR DPD.

5.2.2 Datasets generated at the SCF and supplied to the DAAC for staging

Datasets generated at the SCF during in-flight geometric calibration and supplied to the DAAC to be staged for standard processing are summarized in Table 4. Further information on each is provided below.

Table 14: Datasets generated at the SCF and supplied to the DAAC

Input data	Source of data
Ancillary Geographic Product	MISR In-flight geometric calibration

Table 14: Datasets generated at the SCF and supplied to the DAAC

Input data	Source of data
Calibrated Camera Model	MISR In-flight geometric calibration

5.2.2.1 Ancillary Geographic Product

The Ancillary Geographic Product (AGP) provides the Space-Oblique Mercator grid basis.

This product is described in detail in reference document [M-8].

5.2.2.2 Camera Geometric Model

This is a model of every MISR camera that allows us to determine in what direction a particular CCD element is looking. This model includes the effect of thermal variations which may cause a systematic variation of camera pointing during the course of an orbit.

This dataset is described in detail in reference document [M-10].

5.3 ALGORITHM DESCRIPTION

The projection of MISR imagery to a mathematically defined surface such as the ellipsoid is much simpler than the projection to a irregularly defined terrain surface. Therefore, this algorithm relies on the concept that there is a set of transformation parameters, which directly map the points from the ellipsoid to the MISR image. This set of transformation parameters shall be valid for a local region. In order to locate the tie points necessary to estimate this transformation the algorithm follows these steps:

1. Use the AGP to select the rectangular region which consists of map grid points. This region represent a grid cell.
2. Select a number of map grid points equally distributed throughout the grid cell and denote them to be tie points.
3. Use the IPI to locate those points in the MISR image.
4. Apply Image Coordinate Corrections (ICC) to the location of the points computed by IPI. It should be pointed out that in this step corrections with the attempt to account for errors in navigation and attitude data could not be made by using the image-matching routine. This is so because our projection surface is an imaginary ellipsoid. Therefore, ICC obtained while doing matching for the terrain projection are applied here. The description of the ICC computation is given in §5.3.2.

Once there are accurately computed image location of the tie points, the algorithm continues with the following steps:

1. Estimate transformation parameters using the paired coordinates of the tie points in the MISR

image and in the AGP map grid which is the SOM projection.
2. Use the estimated transformation and locate all of the existing map grid points into MISR image.
3. Use the resampling algorithm to obtain the new radiance value to be assigned to the map grid centers.

5.3.1 Estimation of the transformation for the ellipsoid projection

5.3.1.1 Introduction

The distortion of the SOM map projection grid projected to the MISR image is illustrated in Figure 32. Due to the analytically defined surface of the ellipsoid (absence of the topographic distortion) the transformation between image space and map projection space can be modeled focusing on the following elements: 1) the satellite navigation, 2) the camera geometry, 3) the earth rotation, and 4) the ellipsoid curvature. Figure 1 shows the DF camera image locations of four sparse

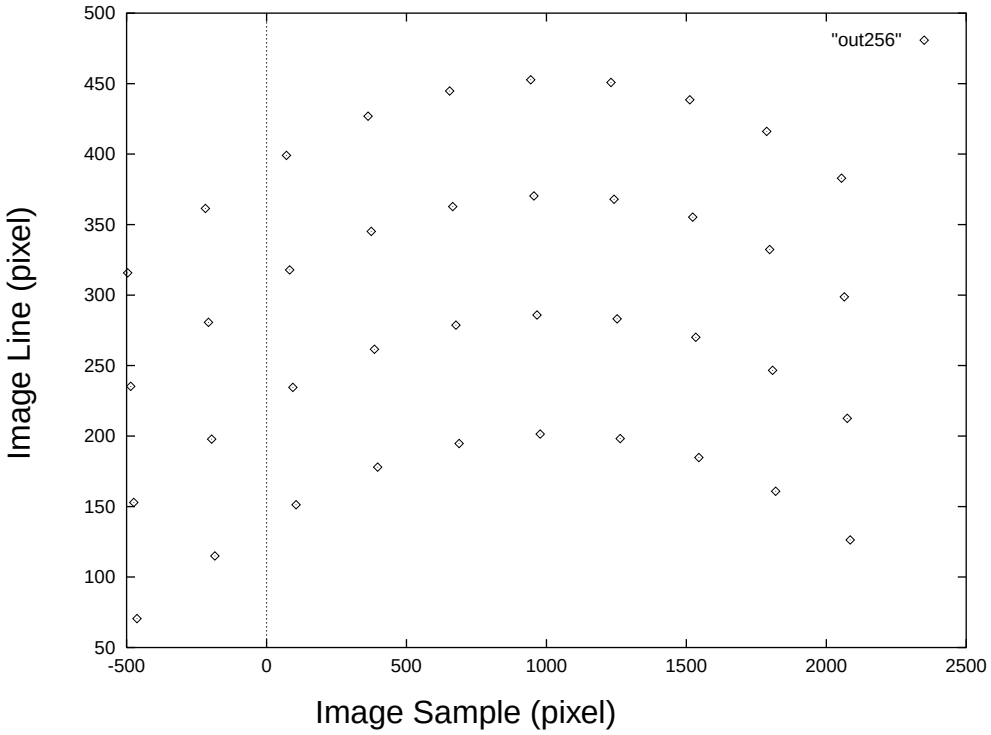

Figure 32: DF Image location of sparse SOM grid centers

SOM lines evenly distributed over an area of 256 grid lines in resolution of 275 meters. In the next section, the derivation of the transformation between image space and map projection space is given.

5.3.1.2 Mathematical description of the algorithm

For a perfect pin-hole camera and a plane surface, the mapping of any line on this plane surface to the image will also be a straight line defined by an affine transform:

$$l_{img} = c_1 + c_2 \Delta l_{som} + c_3 \Delta s_{som} \tag{50}$$

$$s_{img} = d_1 + d_2 \Delta l_{som} + d_3 \Delta s_{som} \tag{51}$$

Where l_{img} and s_{img} are image line and sample coordinates, $\Delta l_{som} = l_{som} - (l_{som})_0$ and $\Delta s_{som} = s_{som} - (s_{som})_0$ are coordinates in the plane of the SOM projection relative to a selected center location. Notice that SOM projection is treated as the projection of a plane surface.

However, in the case of ellipsoid projection, a line in SOM space is physically a curve because of ellipsoid curvature. Thus there will a non-linear mapping of this curve to the line in the image space. Figure 2 illustrates the conversion of an arc distance over a circle to a chord distance on a

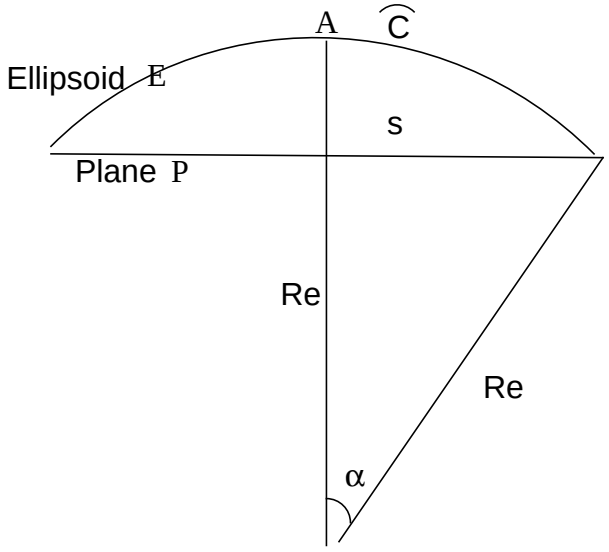

Figure 33: Relationship of line distance and arc distance

plane. Let *A* be the center position of SOM area, *C* be the arc distance over the circle representing Δs_{som} and *s* is the corresponding chord distance on the plane *P* perpendicular to the radius passing *A*, we have the following relation:

$$s = R_e \sin\frac{C}{R_e} \tag{52}$$

Therefore, the relative sample distance in Equations (50)and (51)should be substituted with (52) to correct for the curvature effect cross the swath. Due to the fact that MISR camera is not perfect pin-hole camera and the swath direction is also varying as earth rotates, we would like to expand Equation (52) to Taylor series as $s = k_1 C + k_3 C^3 + O(C^5)$. Substitute *s* into Equations (50) and (51) we then have the mapping of SOM to image space:

$$l_{img} = c_1 + c_2 \Delta l_{som} + c_3 \Delta s_{som} + c_4 \Delta s_{som}^3 \tag{53}$$

$$s_{img} = d_1 + d_2 \Delta l_{som} + d_3 \Delta s_{som} + d_4 \Delta s_{som}^3. \tag{54}$$

For a short segment of SOM swath, the ellipsoid surface is also curved in the along-track direction. We now consider this curvature effect by replacing the cylinder surface with an ellipsoid surface. The ellipsoid curvature now affects not just along the sample direction, but rather along the radial direction of a point to the center of swath, as seen in Figure 34. Therefore, we replace the

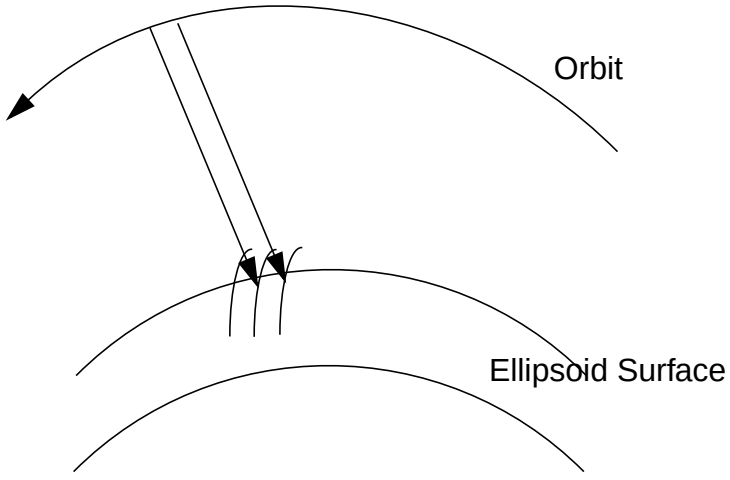

Figure 34: Mapping of multiple lines along the swath

sample term in the previous equation with the radial distances Δr, where $\Delta r = (\Delta l_{som} + \Delta s_{som})^2 = \Delta l_{som}^2 + \Delta s_{som}^2 + 2\Delta l_{som}\Delta s_{som}$. If a set of transforms apply only to a limited lines in the along-track direction, we can ignore the higher order terms of Δl_{som}. The

mapping between the image points and SOM locations is then updated with two additional terms:

$$l_{img} = c_1 + c_2\Delta l_{som} + c_3\Delta s_{som} + c_4\Delta s_{som}^2 + c_5\Delta l\Delta s + c_6\Delta s_{som}^3 \quad (55)$$

$$s_{img} = d_1 + d_2\Delta l_{som} + d_3\Delta s_{som} + d_4\Delta s_{som}^2 + d_5\Delta l\Delta s + d_6\Delta s_{som}^3 \quad (56)$$

By incorporating the curvature factor along the swath we will be able to apply a transform to a segment of swath instead of a line. Here, all the four factors in the mapping of image to ellipsoid surface are relevant as to how many additional terms should be added in the mapping transform, and how long along the swath that a set of transform coefficients can be applied. First, the ellipsoid transform is dynamically calculated on the fly to take into account the orbit perturbation and navigation errors. Its application range depends closely on the dynamic error of navigation error. We set it to be compatible with that of MISR new-to-reference transform (see §4.3.2). Second, the effect of MISR camera along track and side looking angles are included in the above transform. The effect of focal length variation should be smaller than the navigation error variation. Third, the Earth rotation causes SOM swath changing its direction which also limits the application range of the ellipsoid transform, though we found this is a relative minor factor. Finally, as elaborated above, the ellipsoid curvature is the major contributor to the higher order sample terms and the cross terms in Equations (55) and (56). By limiting the application range along the swath up to a magnitude of one grid cell, we can ignore higher order terms other than those presented in (55) and (56).

To build the ellipsoid transform, we first select a number of well distributed grid points over the predefined SOM segment where a set of ellipsoid transform coefficients applies. The IPI function is called to determine the their image locations, for the current band, which are then corrected by the Image Coordinate Corrections (ICC). The ellipsoid transform coefficients are then calculated by a least-square fitting as described by (55) and (56). They will then be used to resample the current band image radiances onto SOM grids.

5.3.2 Computation of the Image Coordinate Corrections (ICC).

5.3.2.1 Introduction

In order to compute the transformation coefficients, a set of the map grid points (ellipsoid surface) must be projected to the MISR image analytically using the Image Point Intersection (IPI) algorithm. However, the newly obtained image locations will be affected by the errors in the navigation and attitude data. An approach to deal with this problem requires the use of the results from the image-matching applied during the terrain-projection processing (see Figure 35). The results from image-matching can be transformed to a set of parameters called Image Coordinate Corrections (ICC). The ICC are then added to the results of the IPI during the ellipsoid projection. The ICC are computed on a grid cell by grid cell basis. A Kalman filter is used to update ICC from the

previous grid cell using the available number of the image matching points in the current grid cell.

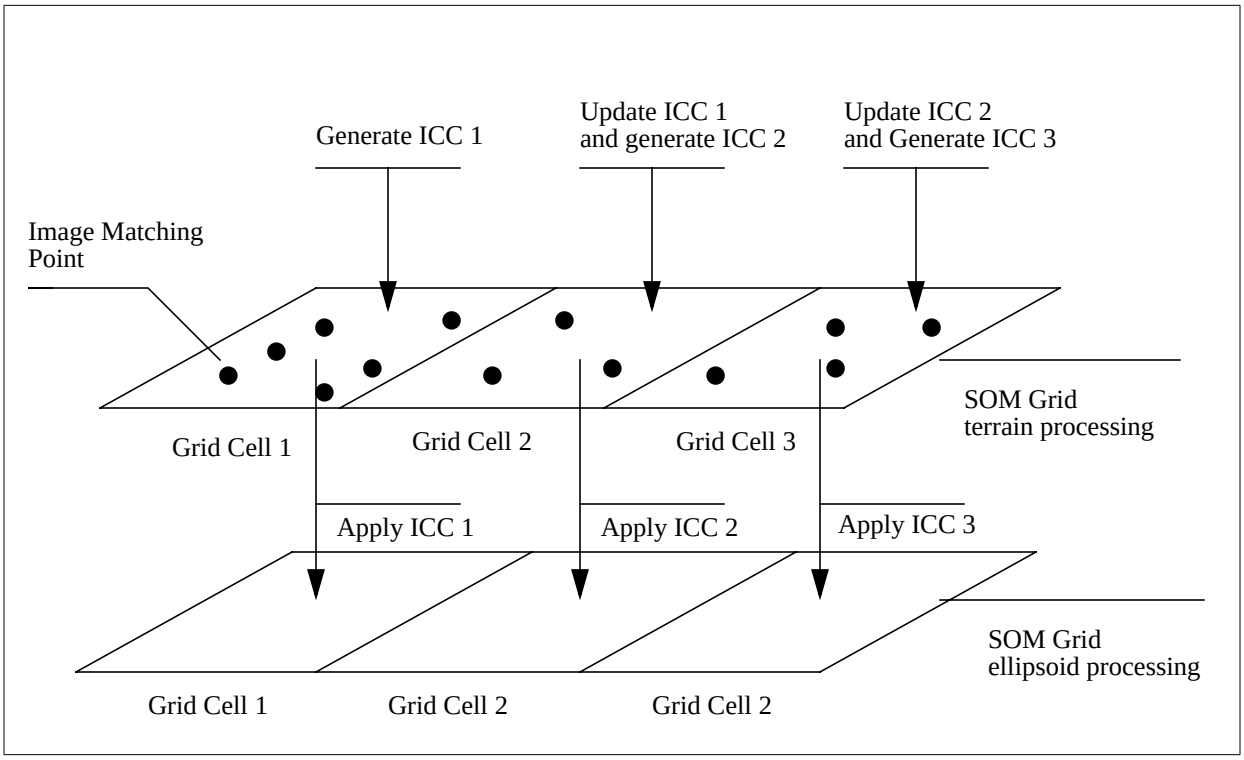

Figure 35: Relation between terrain-projection and ellipsoid-projection processing

5.3.2.2 Mathematical description

The ICC are the set of transformation parameters which relates the image points obtained by the IPI to the “corrected” image points obtained by the image matching. The transformation is of the form:

$$\begin{aligned} s_{corrected} &= k_1(s_{ipi} - s_0) + k_2 \\ l_{corrected} &= l_{ipi} + k_3(s_{ipi} - s_0) + k_4 h + k_5 \end{aligned} \tag{57}$$

where h is the terrain height, and k_1, k_2, k_3, k_4 and k_5 are ICC parameters.

As it can be seen from Figure 35 one set of ICC parameters is calculated per grid cell. It can be assumed that ICC parameters vary slowly when going from one grid cell to another. Thus, a Kalman filter is used to update parameters from the previous grid cell using the matching points in the current grid cell. This prevents parameters from changing radically from one grid cell to the next. However, availability and distribution of image matching points in the current grid cell will determine if the ICC parameters from the previous grid cell should be updated. In situations such as

when a grid cell is completely covered by clouds where no image matching is possible, a previously determined correction (i.e., ICC parameters) is used. In the case of a grid cell with partially available matching points the ICC parameters will not be updated automatically. Instead, a reliability study based on the number and distribution of image matching points and related to the blunder detection part of the algorithm (see §4.3.2.5) will be used to make a decision on the Kalman filter update. In either case: a) fully available matching points, b) partially available matching points, and c) no matching points available, a statistical estimate of the accuracy of the ICC parameters σ_{icc} must be carried out. The estimated σ_{icc} will indicate usefulness of the ICC parameters reflecting the number of the image matching points used and time passed from the last Kalman update of the parameters. The error propagation for the σ_{icc} is based on the use of a time-dependent model of attitude knowledge errors. At this time a realistic model of the attitude errors is still being investigated.

6.0 GEOMETRIC PARAMETERS ALGORITHM

6.1 ALGORITHM SUMMARY

In the geometric parameters algorithm, a set of geometric parameters is generated. More specifically these parameters are the zenith and azimuth angles of the direction to the Sun and to each of nine cameras measured relative to the Earth's ellipsoid and reported on 17.6-km SOM grid centers. In order to compute the geometric parameters, we make use of navigation data, particularly the time at which a point of interest is observed (i.e., 17.6-km center) along with the spacecraft position and velocity at the appropriate time.

6.2 ALGORITHM INPUTS

The input datasets required by the geometric parameters algorithm will be obtained from two sources. First, the SCF will prepared Ancillary Geographic Product and Camera Geometric Model which are briefly described in §3.5.1 and §4.2.2.3. The detail description of these dataset can be found in MISR reference documents [M-8] and [M-10] respectively. Other two input datasets are navigation data (see §4.2.3.1) and Earth-Sun Ephemeris provided by the SDP Toolkit functions.

6.3 ALGORITHM DESCRIPTION

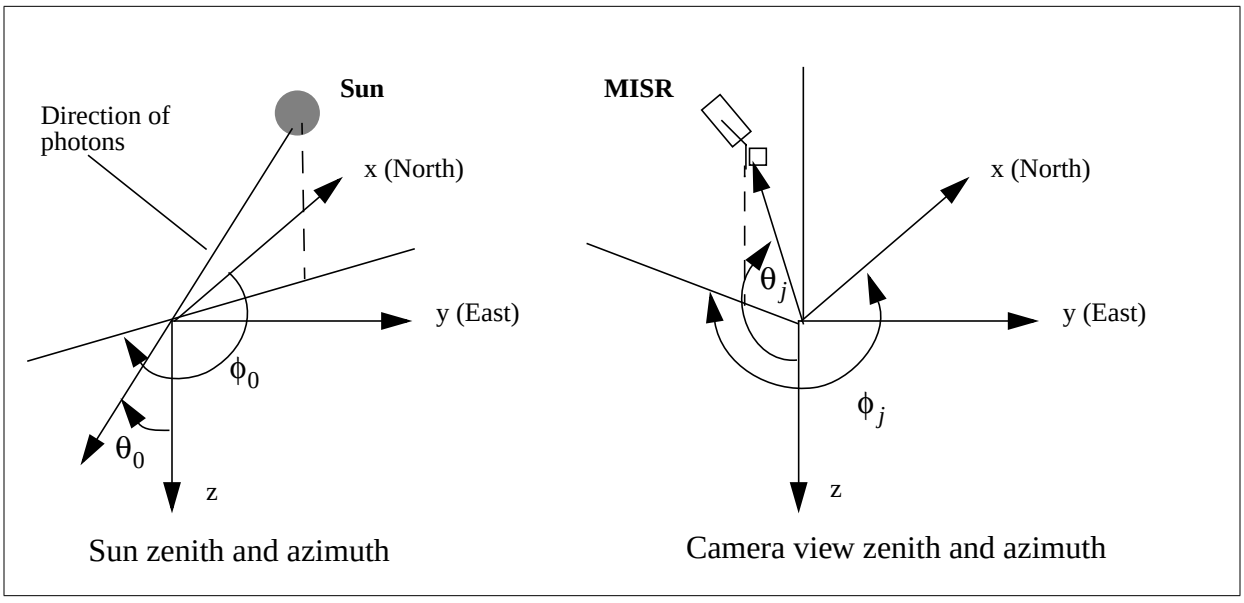

Figure 36: Geometric parameter

The Level 1B2 product will provide the zenith and azimuth angles of the directions from the Sun (θ_0 and ϕ_0, respectively) and to each of the nine cameras (θ_j and ϕ_j, respectively, for the j^{th}

camera) relative to the ellipsoid. They will be obtained and reported on 17.6-km centers which is justified by the small variations of these quantities on this scale.

The zenith angles will be computed relative to the Earth's ellipsoid-normal at the particular point of interest (i.e. 17.6-km centers), and the azimuth angles are computed relative to the local North at the same point. Consequently, at each of those 17.6-km centers a right-handed coordinate system will be defined in which the positive z-axis is aligned with the normal to the Earth's ellipsoid pointing towards the Earth, the x-axis is aligned with the great circle and points toward the North pole, and the y-axis completes the right-handed coordinate system. For convenience this coordinate system will be called the Local Normal (LN) coordinate system in the following text.

The process of obtaining geometric parameters can be divided into three steps. First, the transformation matrix T_{lc} which will take a vector defined in the Conventional Terrestrial Reference (CTR) to a LN system must be found. Second, the unit vector in the CTR system $\hat{\boldsymbol{s}}^{CTR}$ describing the direction from the Sun at time *t*, and the unit vector in the CTR system $\hat{\boldsymbol{v}}_j^{CTR}$ describing the direction toward the j$^{\mathrm{th}}$ camera at time *t* must be found. Here *t* is the time when a 17.6-km center was seen by camera *j*. Finally the transformation T_{lc} will be applied to the vectors $\hat{\boldsymbol{s}}^{CTR}$ and $\hat{\boldsymbol{v}}_j^{CTR}$ in order to have directions toward the Sun and camera expressed relative to the LN system. The elements of the resultant vectors $\hat{\boldsymbol{s}}^{LN}$ and $\hat{\boldsymbol{v}}_j^{LN}$ will be used to obtain the required zenith and azimuth angles.

6.3.1 Mathematical description of the algorithm

Step 1: Transformation between the CTR and LN systems (T_{lc})

If the φ and λ are the geodetic latitude and longitude, respectively, of a point on the Earth, then the transformation which will take a vector defined in the CTR to the LN system for that point can be represented by three sequential rotations: (see Figure 37) 1) the positive rotation around the z-axis for angle $180^o + \lambda$ 2) the negative rotation around the previously rotated y-axis for angle $90^o - \varphi$, and positive rotation around previously rotated x-axis for angle $180°$ Each of these three rotations is defined by a 3×3 orthogonal matrix, or explicitly:

$$R_z(180^o + \lambda) = \begin{bmatrix} -\cos\lambda & -\sin\lambda & 0 \\ \sin\lambda & -\cos\lambda & 0 \\ 0 & 0 & 1 \end{bmatrix}, \; R_y(90 - \varphi) = \begin{bmatrix} \sin\varphi & 0 & \cos\varphi \\ 0 & 1 & 0 \\ -\cos\varphi & 0 & \sin\varphi \end{bmatrix} \text{ and}$$

$$R_x(180°) = \begin{bmatrix} 1 & 0 & 0 \\ 0 & -1 & 0 \\ 0 & 0 & -1 \end{bmatrix} \tag{58}$$

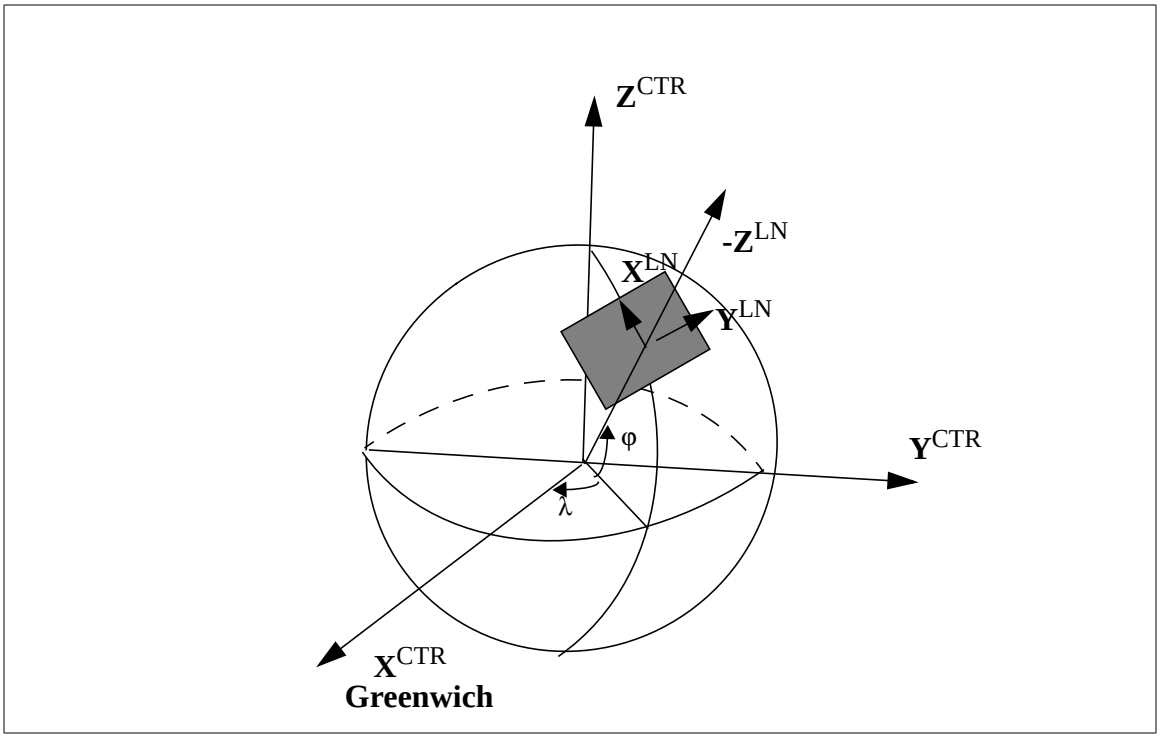

Figure 37: Relation between the CTR and LN system

The transformation T_{lc} is obtained by multiplying these two matrices as follows:

$$T_{lc} = R_x(180°) \times R_y(90^o - \varphi) \times R_z(180^o + \lambda) = \begin{bmatrix} -\cos\lambda\sin\varphi & -\sin\lambda\sin\varphi & \cos\varphi \\ -\sin\lambda & \cos\lambda & 0 \\ -\cos\lambda\cos\varphi & -\sin\lambda\cos\varphi & -\sin\varphi \end{bmatrix} \quad (59)$$

Step 2.a: Find the Sun direction unit vector in the CTR system ($\hat{\boldsymbol{s}}^{CTR}$)

The unit vector $\hat{\boldsymbol{s}}^{GCI}$ describing the direction from the Sun relative to the Geocentric Inertial Coordinate System (GCI) will be found first. Then, by applying the transformation T_{cg} (see§A.2.6) between GCI and CTR the vector $\hat{\boldsymbol{s}}^{CTR}$ will be obtained. It should be pointed out that due to the required accuracy of the geometric parameters, which is 0.1 degree (see Data Product Description document), the position of the Sun will be calculated by assuming a purely elliptical motion of the Earth; that is, the perturbations by the Moon and the planets will be neglected in this algorithm. With this assumption, the vector $\hat{\boldsymbol{s}}^{GCI}$ is defined by three angles: γ, the mean inclination of the Earth's rotation axis from normal to ecliptic, ω, the Earth's true anomaly at given time *t,* and β, the angle between the semiminor axis of the Earth's orbit and the positive x-axis of the GCI (see Figure 38 and Figure 39).

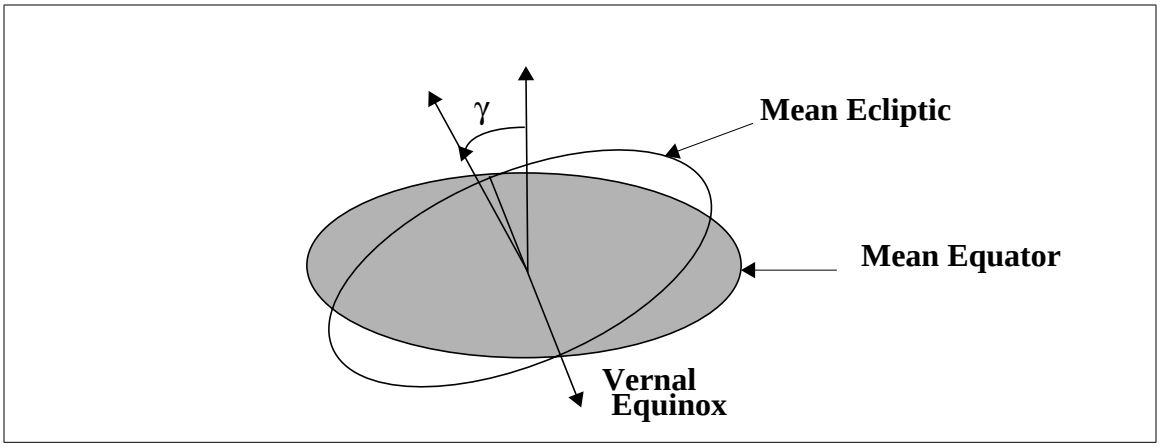

Figure 38: Inclination of the Earth's rotation axis from normal to ecliptic

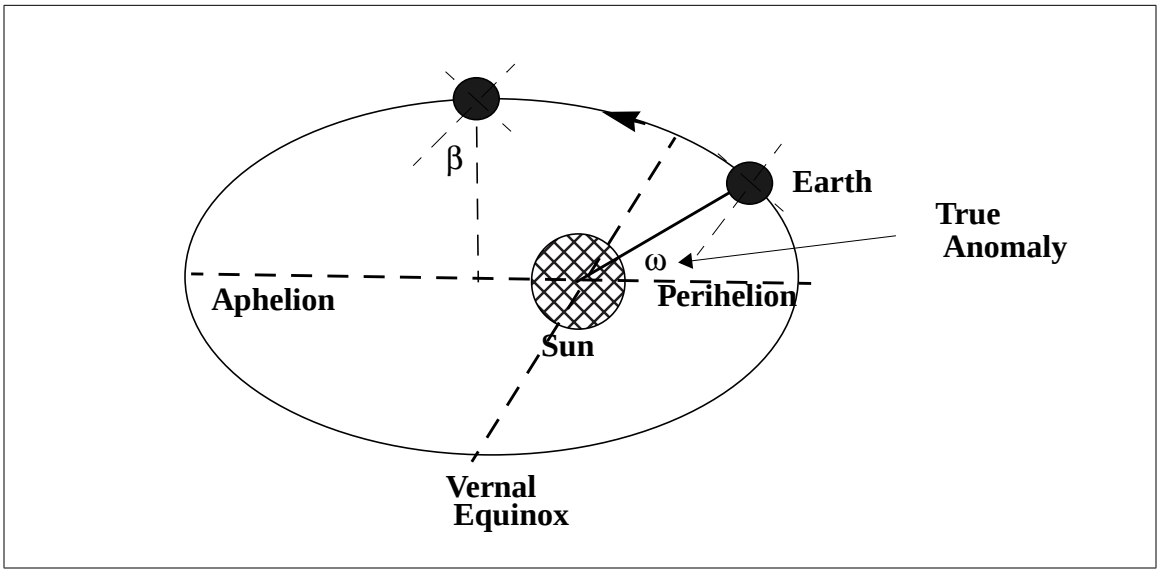

Figure 39: Annual revolution of the Earth

More explicitly:

$$\hat{\boldsymbol{s}}^{GCI} = \begin{bmatrix} -\sin(\omega+\beta) \\ \cos\gamma\cos(\omega+\beta) \\ \sin\gamma\cos(\omega+\beta) \end{bmatrix} \tag{60}$$

By neglecting the perturbations caused by the Moon and planets, angles γ and β can be treated as constant quantities. The angle ω at the given *t* time must be computed. In order to do that time t_p of the last perihelion, given in the same units as *t*, is taken as the input to the algorithm. Then, with $dt = t - t_p$ as the time that elapsed from the last perihelion, consider the Earth to be at a point G on the orbital ellipse for time *t*. The position of the Earth in its orbit is defined by the angle ω, the

true anomaly, which is measured in the direction of the motion (see Figure 40). The angle associ-

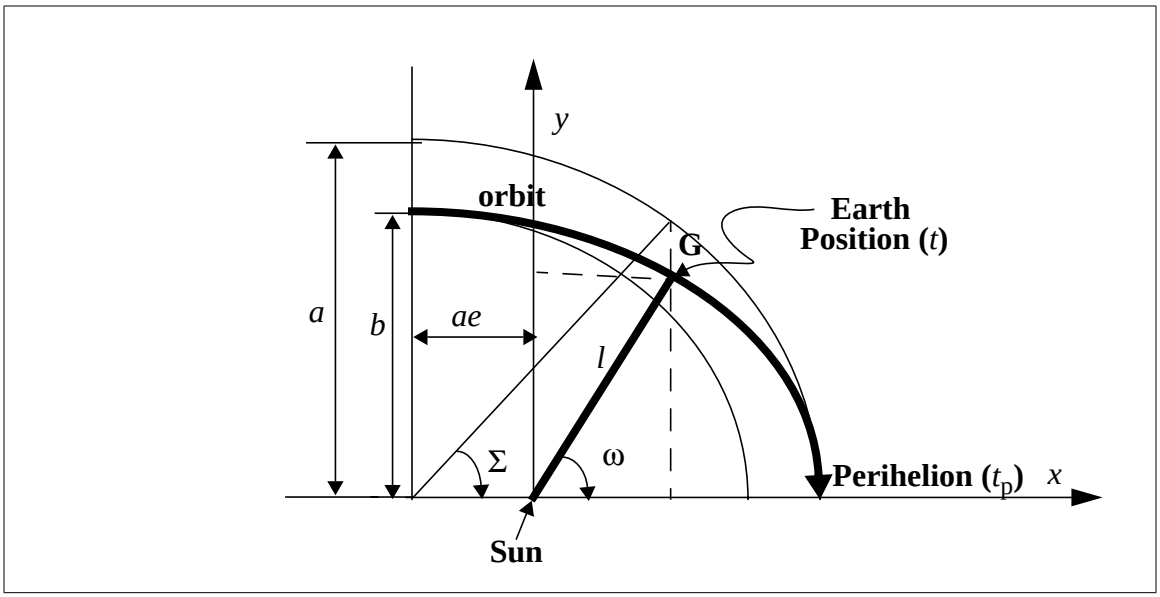

Figure 40: One-Quarter of Earth Orbit

ated with the auxiliary circle of radius *a* (i.e. semimajor axis) is called the eccentric anomaly, and is denoted by Σ. The mean anomaly is the true anomaly corresponding to the motion of an imaginary Earth of uniform angular velocity. It may be visualized as the angle that is zero at perihelion and increases uniformly at a rate of $r = 360^{o}/year$. It is denoted by μ. So, if dt and r are given in the same time scale $\mu = dt \cdot r$. The relation between the eccentric anomaly Σ and the mean anomaly is given by Kepler's equation (see [15]):

$$\mu = \Sigma - e\sin\Sigma \tag{61}$$

where *e* is the eccentricity of Earth's orbit. Equation (61) needs to be iterated in order to solve for Σ. The rectangular coordinates of the Earth in its orbit, as seen from the Figure 40, are:

$$x = l\cos\omega = a\cos\Sigma - ae \tag{62}$$

$$y = l\sin\omega = b\sin\Sigma \tag{63}$$

where *a* and *b* are Earth's orbit semimajor and semiminor axes respectively.

As was stated earlier the true anomaly ω must be computed. Its relation with the eccentric anomaly is obtained from (62) and (63) as:

$$\tan\omega = \frac{y}{x} = \frac{b\sin\Sigma}{a(\cos\Sigma - e)} \tag{64}$$

So, we find ω by taking the arctangent of (64). The constant values for angle γ, also called obliquity of the ecliptic, and angle β which is directly related to the mean longitude of perihelion, are taken from the literature [34]. Going back to Equation (60) we solve for $\hat{\boldsymbol{s}}^{GCI}$. Applying T_{cg} to $\hat{\boldsymbol{s}}^{GCI}$ we solve for $\hat{\boldsymbol{s}}^{CTR}$.

Step 2.b: Find Earth to camera *j* direction unit vector in the CTR system ($\hat{\boldsymbol{v}}_j^{CTR}$)

The section explaining the IPI (see §4.3.4) described in detail how image coordinates of the point on the Earth and in the focal plane of the camera *j* are used to define the camera to Earth look vector by applying transformations T_{si}, T_{os}, and T_{co} described in §A.2. The same procedure is used for the points of interest in this algorithm (17.6-km centers) and the vector $\boldsymbol{l}_j^{CTR}$ is obtained. The vector $\hat{\boldsymbol{v}}_j^{CTR}$ is in the opposite direction, so it is equal to the negative of the normalized vector $\boldsymbol{l}_j^{CTR}$, or:

$$\hat{\boldsymbol{v}}_j^{CTR} = -\hat{\boldsymbol{l}}_j^{CTR} \tag{65}$$

Step 3: Final computing of the geometric parameters

In step 1 the transformation T_{lc} is found. Applying T_{lc} to the vectors $\hat{\mathbf{s}}^{CTR}$ and $\hat{\boldsymbol{v}}_j^{CTR}$ defined in steps 2.a and 2.b respectively we will get the Sun direction and the Earth-to-camera direction referenced to the LN system. or:

$$\hat{\mathbf{s}}^{LN} = T_{lc} \times \hat{\mathbf{s}}^{CTR} \qquad \text{and} \qquad \hat{\boldsymbol{v}}_j^{LN} = T_{lc} \times \hat{\boldsymbol{v}}_j^{CTR} \tag{66}$$

Now, with the corrections for the proper quadrant applied to the equations (68) and (70) the zenith angle of the direction to the Sun is given by:

$$\theta_0 = \mathrm{acos}([\hat{\mathbf{s}}^{LN}]z) \tag{67}$$

The azimuth angle of the direction to the Sun is given by:

$$\phi_0 = \mathrm{atan}\left(\frac{[\hat{\mathbf{s}}^{LN}]_y}{[\hat{\mathbf{s}}^{LN}]_x}\right) \tag{68}$$

In the same fashion, the zenith angle of the view direction is given by:

$$\theta_j = 180 - (\mathrm{acos}([\hat{\boldsymbol{v}}_j^{LN}]_z)) \tag{69}$$

and the azimuth angle of the camera view direction is given by:

$$\phi_j = \operatorname{atan}\left(\frac{[\hat{\boldsymbol{v}}_j^{LN}]_y}{[\hat{\boldsymbol{v}}_j^{LN}]x}\right) \tag{70}$$

7.0 PRACTICAL CONSIDERATIONS

7.1 NUMERICAL COMPUTATION CONSIDERATIONS

Requirements on processing speed and data storage are described in the MISR Science Data Processing Sizing Estimates document. These figures are based on benchmarking carried out during the Beta software development, and will be updated as new benchmarks become available.

7.2 PROGRAMMING AND PROCEDURAL CONSIDERATIONS

Software guidelines to be followed during algorithm development are described in the MISR Algorithm Development and Validation Management Plan.

7.3 QUALITY ASSESSMENT AND DIAGNOSTICS

7.3.1 Introduction

The Quality Assessment (QA) described in this section deals with the quality of the GRP defined by its overall geometric accuracy. The primary objectives of the geometric QA are: a) determination of a Geometric Data Quality Indicator (GDQI) used in Level 2 scientific processing algorithms, and b) verification of the geometric algorithm performance throughout the mission. The most reliable and the obvious approach would be to use a human operator to interactively measure the location of check-points (i.e. points with known geographic location) distributed throughout the GRP. However, due to the large data rate and spatial extent of the GRP (i.e., world), this method is not feasible. Instead, in order to be suited to the autonomous nature of the geometric algorithm, the entire QA is divided into three parts: 1) routine, 2) interactive and 3) extensive. Also, the segment of data which corresponds to a block (defined in the AGP and is equal two grid cells as its defined in L1B2 ATB) represent a unit for the QA.

7.3.2 QA Summary

The routine assessment operation is an automatic process running with very little involvement of an analyst. It is based on the analysis of the statistical data created as the part of L1B2 standard processing. The objective of this group of assessment procedures is to continuously monitor the quality of the L1B2 Georectified Radiance Product (GRP) with an inexpensive technique. The main disadvantages are related to the limitations and confidence level of the statistics used. However, the expectation is that this assessment will indicate some of the more obvious problems with the product. In those cases more demanding and complete assessment/validation operations will be triggered. The routine assessment operation can be run on either SCF or on the DAAC.

The interactive assessment operation is a process controlled by an analyst. It is based on the visual inspection of image or graph data. The objective is to recognize bad quality data without the need for more extensive validation processing. The main limitations is that only data anomalies visible

to the human eye can be detected. However, the expectation is that this assessment is used as a filter before more demanding validation is attempted. In some cases the interactive assessment is the initial part of the extensive validation. The interactive assessment activity is either scheduled or triggered by a routine assessment and it will be a part of SCF operations.

The extensive assessment operation is a process which requires elements such as: a) analyst, b) special software and hardware, and c) external data. This operation can be looked upon as a complete validation operation focused on the geometric aspect of the GRP. The objective is to fully investigate geometric accuracy of selected segments of data and by making measurements which use provided ground truth data. The main restriction is that only limited amounts of data can be extensively validated due to the availability of external data and the resources required by the process. The extensive validation is a part of SCF operations and is either scheduled or triggered by a routine or interactive assessment.

The interactive and extensive assessment include fairly standard operations which will be described in the “In-flight Geometric Calibration Plan” (JPL D-13228) document. In the following section the algorithm behind routine assessment is described in more detail.

The Table 15 gives a breakdown of the GRP quality assessment activities.

Table 15: QA time-table overview

Time / Assessment	Continuously throughout the mission	During In-flight Calibration	Periodically (scheduled)	Occasionally (triggered)
Routine	Yes, after In-flight Calibration.			
Interactive		Yes.	Yes, two times a year.	Yes, if triggered by routine assessment or platform maneuver
Extensive			Yes, once a year.	Yes, if triggered by routine assessment or platform maneuver

7.3.3 Routine Quality Assessment

The geometric accuracy of the GRP depends two factors: 1) the accuracy and quality of the ancillary datasets (e.g., Projection Parameters, navigation data), and 2) the availability of the image

region suitable for image matching during image-to-image registration. A combined effect of these factors can be monitored through the analysis of certain statistical parameters (i.e., QA parameters) resulting from the image-to-image registration algorithm. These QA parameters can be used to either produce GDQI or to indicate possible diverging of the GRP geometric accuracy. The following is a list of the QA parameters associated with the GRP algorithm.

Table 16: GRP geometric accuracy QA parameters

	QA Parameter	Description
QA Parameters Block level		
	Number of grids cells NG	This is the number of generated grid cells used to compute local image-to-image transformation. The minimum is 2 and maximum depends on the definition of the smallest size grid cell.
	Projection Parameters Quality Indicator PPQI	This quality indicator depends on: 1) availability of ROI, 2) quality of the global DEM used for this block, and 3) results of the bundle adjustment during in-flight geometric calibration. It range from 0 to 1.
QA Parameters Grid cell level		
	Accuracy test At	This flag will indicate if the transform associated with this grid cell passed the accuracy test.
	Is it subgrided Sg	This flag will indicate if there is a generated transform of the grid cell which is one level below current one.
	Subgriding level Nsl	This number tells to which subgriding level this grid cell belongs to
	Number of potential grid points Npp	This is the number of grid points belonging to the grid cell initially selected to be used for the matching. This number is set to be 50 for first subgriding level
	Number of candidate grid points Ncp	This the number of grid points which will be used for matching after water and cloud points are discarded.
	Number of blunders Npb	This is the number of detected blunders
	Number of matched grid points Nmp	This is the number of successfully matched points.
	Average correction Nmc (line, sample)	Average of the corrections resulting from image matching.
	Standard deviation of correction Nsc (line, sample)	Standard deviation of the corrections resulting from the image matching. Meaningful only if there is sufficient number of successfully matched points Nmp.

Table 16: GRP geometric accuracy QA parameters

	QA Parameter	Description
	Standard deviation of image to image transformation Nst (line, sample)	Generated based on standard deviation of the matching points. A priori estimate is used if a point is not matched. The a priori accuracy estimate is propagated to from the previous block prior to matching. Within the block the transform propagates from the higher grid level.

Monitoring GRP geometric algorithm performances

The QA parameters listed in Table 16 will be used to monitor the performance of the geometric algorithm relative to the geometric accuracy of produced GRP. This is an automatic procedure designed to indicate parts of the L1B2 processing which may have produced GRP with significantly large spatial errors. The segments of the GRP with possible large errors will be subjected to further QA activities (i.e., interactive, extensive).

The basic idea behind the analysis of the QA parameters is to compare them to a previously established threshold set. The threshold set will first be established during the final testing phase, before launch. Once the in-flight geometric calibration is completed the threshold set will be determined using the processing over the selected region with well known ground truth. Most likely, a sample of the regions over U.S. will be used. The elements of the threshold sets are:

Ratio of blunders over number of candidate points to match (Npb/Ncp) - $\overline{Ppb}$.
Ratio of successfully matched points over number candidate points to match (Nmp/Ncp) - $\overline{Pmp}$.

Average matching correction for a particular grid cell level (line, sample) - $\overline{Nmc[2]}$.
Standard deviation of the matching corrections for a particular grid cell level (line, sample) $\overline{Nsc[2]}$

Standard deviation of image-to-image transformation for a particular grid cell level - $\overline{Nst}$.

The threshold set parameters are compared to those obtained dynamically on a grid cell per grid cell basis. The scenario of the comparison method depends on the number of candidate matching points and the accuracy of the generated transform. There are three basic cases:

1. Case A: There are no candidate matching points Ncp = 0. This grid cell can not provide any useful information. So, there will be not further analysis associated with this grid cell.
2. Case B: The accuracy test for the QA parameter At is negative and grid cell belongs to the level 2 or higher. This will indicate either a problem in algorithm or inadequate initial size of the grid. No further analysis of the QA parameters is necessary. The corresponding block of the GRP shall be investigated interactively.
3. Case C: If neither of the previous two cases are applicable then each element of the threshold set will be compared to its dynamically produced equivalent. If one of the elements fail a threshold test, then it would be necessary to perform further interactive assessment.

Determination of the GDQI

The GDQI represent one number which will describe the geometric quality of the entire GRP block. A selected method for the computation of the GDQI assume the following factors to be determinative: a) overall number of matched points, b) estimated standard deviation of the generated transform, c) percentage of area which satisfy previously determined accuracy requirement, and d) quality of the corresponding Projection Parameters. The proposed computation of the GDQI is

$$GDQI = \frac{1}{2n(\sigma_{max} - \sigma_{min})} \sum_{i=1}^{n} (\sigma_{max} - Nst)(n \cdot PPQI \cdot R_i^p \cdot R_i^a + 1) \qquad (70a)$$

where:

n represent total number of the grid cell which are not to be subgrided anymore.

R_i^p is the ratio of the matched points over the potential number of the points to be matched (Nmp/Npp) for this particular grid cell.

R_i^a is the ratio of the area occupied by this grid cell over the area of the entire block. This is defined by the level to which grid cell belongs. For instance, 0.5 for level 1, 0.25 for level 2 etc.

σ_{min} is the predicted standard deviation of the transform which has a full set of successfully matched points, i.e., goal accuracy.

σ_{max} is the predicted standard deviation of the transform which relay only on the points supplied by the navigation data.

$PPQI$ is the quality indicator for Projection Parameters having range between 0 and 1. For example $PPQI = 0$ in the when ROI is not available or global DEM is of poor quality.

The Table 17 presents GDQI example values resulting from equation (70a).

Table 17: GDQI example values

GDQI value per GRP block	Description
1	This is the maximum of (70a). This will happened if all of the potential points have been matched successfully and all of the final transforms provide accuracy which is equal or better than predicted goal accuracy. The blocks with the GDQI equal 1 are “good” relative to the accuracy requirement.
0 > 1	These values cover many different conditions. For example, not all of the potential points have been matched and/or there is a number of transform (relatively small) whit significantly large standard deviation. In general, the blocks with the GDQI in this range should be considered as “good” relative to the accuracy requirement.
0	The value of 0 reflect several different conditions. For example: A) There are no matched points throughout the block (as in the case when entire block is cloudy or no ROI available) and the block is significantly far from the last block with matching points, so that Nst equal σ_{max}. B) All of the potential points are matched but the area corresponding to the transforms with accuracy equal or better than σ_{min} is equal the area covered with the transforms with accuracy equal or worse than σ_{max}. In general, case A is more likely to happened than case B. The blocks with GDQI equal 0 should be treated as “good” assuming that accuracy of the supplied navigation data is acceptable.
-1 > 0	These values cover many different conditions. For example, not all of the potential points have been matched and/or there is a number of transform (relatively large) with significantly large standard deviation. In general, the blocks with the GDQI in this range should be considered as “bad” relative to the accuracy requirement.
-1	This is the minimum of eq. (70a). This would happened if all of the potential points have been matched successfully and all of the final transforms have standard deviation equal or larger than σ_{max}.

The Table 17 presents examples of the computed GDQI values covering its range from 1 to -1. 0 represent a ambiguous condition. It should be pointed out that GDQI computation is designed so

that results can be easily represented be one of the programing data type (e.g., signed character) with its fixed minimum and maximum value. In the case that only “good” or “bad” GDQI are required. a suggestion is to classify all positive values and zero as “good” and all negative values as “bad”. This will assume that accuracy of the supplied navigation data is sufficient to meet required geometric accuracy of the GRP. However, it may be reasonable to interpret GDQI data with a different classification scheme (e.g. depending on the camera view angle). Also, appropriate selection of σ_{min} and σ_{max} plays important role in the interpretation of GDQI values. Before the launch, these values are predicted based on the orbit error model and a estimate of matching accuracy. Once in-flight, σ_{min} and σ_{max} can be improved based on the results over selected test sites.

7.4 EXCEPTION HANDLING

The Level 1B2 software development team is also the team that undertook the algorithm prototyping. Exception handling follows as part of that work and will be detailed at a later stage. The range of alternatives for handling special cases in the algorithm itself have been covered by earlier parts of this document.

8.0 ALGORITHM TEST AND VALIDATION

8.1 INTRODUCTION

The algorithm proposed in the previous sections will be tested through all phases of the associated software development. Depending on the maturity of the algorithm and implementation software there may be some modifications of the testing procedures throughout the development life cycle. However, the areas identified as the most important for overall success of the testing are: a) simulation of the orbit navigation and attitude data, b) simulation of the MISR imagery and c) definition of the test procedures. One of the primary goals of the georectification algorithm is the removal of effects due to errors in the navigation and attitude data. Also, the proposed algorithm assumes a relative smoothness in the spacecraft perturbation. Therefore, realistic simulation of the spacecraft data is a precondition for meaningful testing. The proposed geometric algorithm deals extensively with the MISR radiance data (e.g., image matching, resampling). Therefore, images with radiometric and geometric characteristic of the future MISR image must be produced and used as the input to test procedures. The test procedures must be defined so that important segments of the entire algorithm can be tested fully independently in addition to the tests of the integrated software.

8.2 ORBIT SIMULATION

The orbit simulation is mostly focused on the following attributes of the navigation and attitude data: 1) actual behavior of the spacecraft, and b) errors in the reported data. In that regards, two sets of orbit data will be produced. One is the “actual” data, which describes what the spacecraft is actually doing. This dataset is used to generate simulated MISR imagery which is the input to the georectification software. The actual data should include realistic orbit perturbations. The second is “measured” data, which describes the reported navigation data. The measured data should include realistic navigation errors. The “measured” data are the only navigation data which will be available during the georectification processing. In order to cover the range of perturbations and errors, the simulated data will be grouped into three category: 1) best case, 2) nominal case, and 3) worst case.

8.2.1 Spacecraft position perturbations and errors

Position perturbations arise only from sources outside of the spacecraft. The perturbation sources, such as drag and higher order terms in the gravity multiple expansion, are only slowly varying. At this stage we will ignore perturbations over a single orbit, and continue using the orbit program supplied in the PGS toolkit without change. However, repeat orbits (i.e., those 233 orbit path numbers apart) can shift relative to each other by as much as 20 km in the cross track direction. This shift will be included in our orbit model.

A description of the navigation measurements is given in [11]. A brief summary is given here.The position and velocity of the spacecraft is measured at 10.24 second intervals from TONS. The

requirement is that position is measured to ±150 meters (3σ) and a velocity is measured to ±0.160 meters/second (3σ). However, the predicted position measurement errors from [7] are somewhat better (see Table 18). For the predicted velocity measurement errors, we just use the requirements.

Table 18: Predicted measurement errors

Performance Level	Predicted Accuracy (3σ)
Best case	< 50 meters
Nominal case	75 meters
Worst case	100 meters

Presumably, there is some correlation between the errors from separate TONS measurements. In our simulation we will ignore correlation and treat measurements as independent.

In between TONS measurements, the position and velocity is calculated at 0.512 second intervals by integrating force equations derived from a model. The goal stated in [11] is that the largest errors from integrating the force equation shall be less than 10% of the error from TONS measurement (15 meters). Simulations were run on the algorithm to be used, and the results are actually far better than this (0.02 meters, see [11]). We can safely ignore this source of error, and only include the errors from the TONS measurements.

8.2.1.1 Simulated spacecraft positions and velocities

We will produce position and velocity information for reference orbits by running the orbit program included in the PGS toolkit, without change. For new orbits, we will do the following:

1. Run the PGS toolkit orbit program, generating position and velocity information with 40.8 ms time spacing.

2. Add a static shift (see Table 19) to each position in a direction perpendicular to both the velocity vector and the position vector. This gives us “actual” data.

3. Select a pseudorandom number from a normal distribution with a 0 mean and σ given in Table 19. Add this to each position measurement from time 0 to (10.24s - 40.8ms) (this is 250 lines). Select another pseudorandom number with 0 mean and σ given in Table 19. Add this to the velocity measurements from time 0 to (10.24s-40.8ms). Select another two pseudorandom numbers, and add them to the position and velocity measurements from 10.24s to (20.48s-40.8ms). Continue this for the rest of the orbit data. This gives us “measured” data.

Note that we report measurements every 40.8 ms, while the information will only really be avail-

Table 19: Numbers for modeling position and velocity

Performance Level	Shift (km)	Along Track Position σ (m)	Cross Track and Radial Position σ (m)	Velocity σ (m/s)
Best case	0	15	5	0.06
Nominal case	5	25	5	0.06
Worst case	10	50	5	0.06

able every 1.024 seconds. The PGS toolkit routines are expected to interpolate data and provide navigation information at the time requested.

8.2.2 Spacecraft attitude perturbations and errors

A description of the attitude perturbations is given in [39]. A brief summary will be given here.

The attitude errors are broken into two pieces, static and dynamic (see Table 20). The dynamic

Table 20: Attitude Accuracy

	Pointing Accuracy (arc-sec, 3σ)		
	Roll	Pitch	Yaw
Static	52.5	71.4	83.9
Dynamic	17.3	17.1	13.5
Sum	69.8	88.5	97.4
Unallocated	80.2	61.5	52.6
Require-ments	150.0	150.0	150.0

piece has been modeled, and numbers for the maximum perturbations over different time scales ware determined. The results are given in Table 21.

The allocations for pointing knowledge are shown in Table 22, (see [39]).

The static errors are constant over long time scales. This long time scale is not really defined but most likely, a portion of the static errors is truly constant (e.g., calibration error in the star tracker). However, it is possible that a portion may vary from orbit to orbit (e.g., initial gravity unloading).

Table 21: MISR Jitter/Stability

Time Scale (seconds)	Maximum Perturbation (arc-sec, 3σ)		
	Roll	Pitch	Yaw
0.1	0.8	1.7	1.5
1.0	1.9	2.6	2.2
1.0 Requirement	8.0	8.0	8.0
1.8	2.2	3.0	2.6
6.0	3.3	5.2	4.7
9.0	4.2	6.5	6.1
12.5	4.6	7.1	6.4
420.0	9.7	13.1	10.6
420.0 Requirement	20.0	20.0	20.0
480.0	9.9	13.9	10.6

Table 22: Pointing navigation errors allocation

	Pointing error (arc-sec, 3σ)		
	Roll	Pitch	Yaw
Static	43.0	64.8	41.7
Dynamic	15.6	15.4	11.2
Sum	58.6	80.1	53.0
Unallocated	31.4	9.9	37.0
Requirement	90.0	90.0	90.0

The in-flight camera calibration should remove knowledge errors that are truly constant, but will not remove knowledge errors that vary from orbit to orbit.

The attitude is measured by infrequent star tracker measurements (every 30-120 seconds), with gyro measurements used to calculate attitude for times in between the star tracker measurements. This means that there is a strong correlation in the dynamic navigation errors for points in between the star tracker measurements. It is sufficient for the purpose of this simulation to treat these measurements as independent. However, once the orbit simulations are to be used when validating in-flight calibration algorithm (i.e. production of the Projection Parameters) the correlation factor must be included.

8.2.2.1 Simulate spacecraft attitude and attitude rates

The steps in modeling the attitude for both reference and new orbits are the following:

1. Generate static offsets to the roll, pitch and yaw angles. To do this, choose three pseudorandom numbers from gaussian distributions with means 0 and sigmas given in Table 23. Initialize the roll, pitch, and yaw angles to these three numbers for every orbit position.

2. Start with the long scale numbers from Table 23. Select three pseudorandom numbers from gaussian distributions with 0 mean and sigmas from Table 23. Add these numbers to the roll pitch and yaw at time 0. Repeat, for the roll pitch and yaw at time <long time scale>. For orbit information between time 0 and <long time scale>, do a linear interpolation from these two endpoints (see Figure 41). Then, add pseudorandom numbers to the point at 2x<long time scale> and interpolation between times <long time scale> and 2x<long time scale>. Continue for all points in the orbit.

3. Repeat step 2 for the medium time scale (see Figure 42). Then repeat for the short time scale.

4. For each point in the orbit, select 3 pseudorandom numbers to add as jitter. This produces the “actual” data. For an example of attitude generated by this algorithm, see Figure 43.

5. To generate static knowledge errors, select 3 pseudorandom numbers from a gaussian distribution and sigma given in Table 23. Add these numbers to every roll, pitch, and yaw.

6. For each orbit position, select 3 pseudorandom numbers with sigma given in Table 23 and add to roll, pitch, and yaw. This gives us “measured” data.

Note that the model of attitude perturbations is not perfect. It has the following problems:

1. We assume that over a given time scale the drift in attitude reaches its maximum and minimum at the endpoints of that time scale; there is no reason for this to be the case.

2. We ignore the correlations between the simulated perturbations at the different time scales. Including jitter increases the maximum perturbation over the long time scale, but we ignore this. The effect is that our model overestimates the attitude perturbations.

Table 23: Numbers for modeling attitude perturbations and errors

			Sigma for Random Distribution		
			Best Case	Nominal Case	Worst Case
Attitude Perturbations	Static	Roll	17.5	33.0	50.0
		Pitch	23.8	33.0	50.0
		Yaw	28.0	33.0	50.0
	Long Time Scale (420.0 seconds)	Roll	3.2	4.0	6.7
		Pitch	4.4	5.6	6.7
		Yaw	3.5	5.1	6.7
	Medium Time Scale (10.0 seconds)	Roll	1.5	2.25	3.0
		Pitch	2.4	3.6	4.8
		Yaw	2.1	3.2	4.2
	Short Time Scale (1.0 seconds)	Roll	0.6	1.6	2.7
		Pitch	0.9	1.6	2.7
		Yaw	0.7	1.6	2.7
	Jitter Time Scale (40.8 ms)	Roll	0.3	0.4	0.6
		Pitch	0.6	0.9	1.2
		Yaw	0.5	0.7	1.0
Attitude Errors	Static	Roll	0.0	14.3	0.0
		Pitch	0.0	21.6	0.0
		Yaw	0.0	13.9	0.0
	Dynamic	Roll	5.2	5.2	30.0
		Pitch	5.1	5.1	30.0
		Yaw	3.8	3.8	30.0

3. We have included four arbitrary time scales (Figure 41 and Figure 42). There is no particular

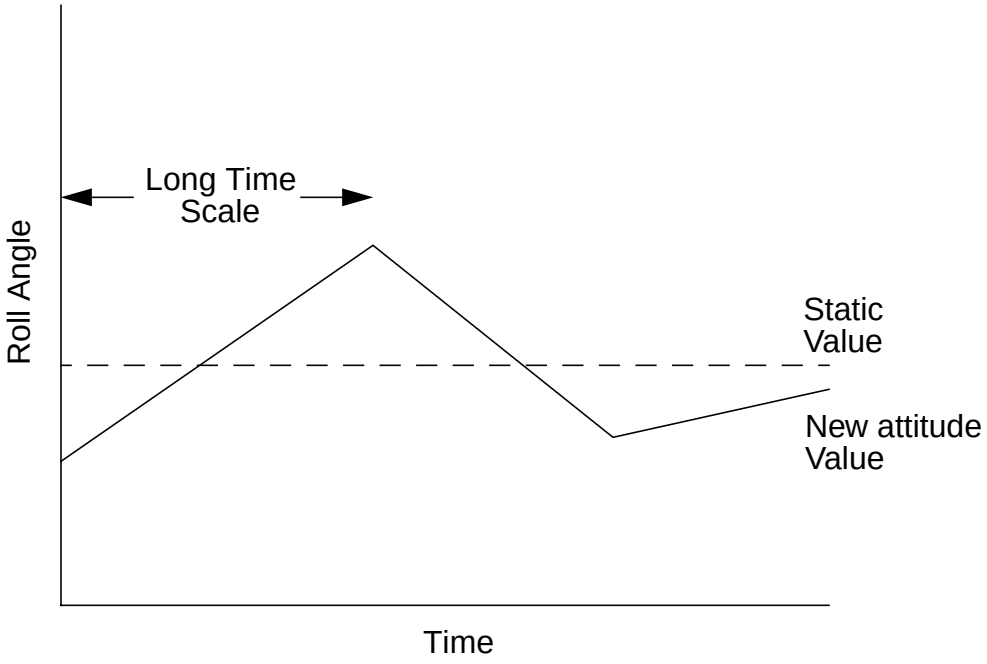

Figure 41: Attitude model, first step

reason that we did not use three or five, or pick different time scales (e.g., 2, 15, and 460 seconds).

8.3 SIMULATION OF MISR IMAGES (i.e., MISRSIM)

In order to prototype and validate elements of the geometric processing described in this document, data must be acquired which match closely the characteristics of MISR instrument data. Since currently there does not exist a push-broom instrument with the combination of extreme forward and aft views of MISR, the data must be simulated. The software written to simulate such data has been named MISRSIM. (The work described in this section was published in [21].)

A technique known as *terrain rendering* is employed to model the topographic effects of imaging the Earth's surface at extreme viewing angles. Terrain rendering is the mapping of image data onto Digital Elevation Models (DEMs) to produce a three-dimensional simulation of the actual surface. Rendering software was acquired from the Digital Image Animation Laboratory (DIAL) at NASA JPL. The DIAL has used this code very successfully to produce simulated flights over the terrain of California and the planet Venus [36]. This software uses a ray-casting algorithm, where a given view is calculated from a single point in space (or *eye point*) relative to the location of the terrain. The eye point's field of view and aspect ratio define a view-plane perpendicular to

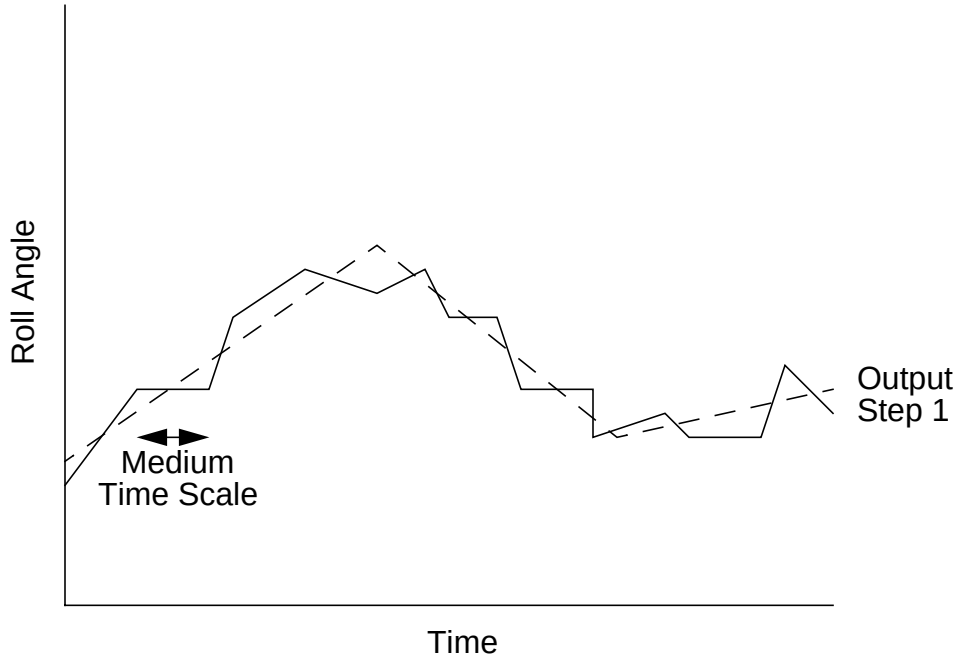

Figure 42: Attitude model, second step

the line of sight representing the image to be computed. For the DIAL software, the view-plane is a finite rectangular plane such as would be seen by a frame camera. For use in MISRSIM, the software was adapted such that the view-plane represented what was seen by a single line-array CCD.

8.3.1 MISRSIM process flow

8.3.1.1 Data Preparation

To simulate the radiance image data, Landsat Thematic Mapper (TM) scenes were used. A Universal Transverse Mercator (UTM) plate of an area of central Mexico with a map scale of 28.5 m was acquired. This image also was identified as representing an area of high relief and strong image texture. TM Band 3 (red) was separated from the data to model the MISR red channel. A DEM with 100 m postings which had already been registered to the UTM plate was resampled to the Landsat scale. Each UTM plate covers approximately 2° of longitude and 1° of latitude. This is not sufficient to cover the width of a MISR swath. In addition, 1° of latitude corresponds to a simulated orbit segment of no more than 15 seconds. In order to cover the full width and length of a swath segment corresponding to a 7 minute period, where an area is observed by all cameras, the following technique is used: First, the ascending node of the MISR orbit path is chosen such that the ground track passes through the central point of the input region. Then, a Space-Oblique Mer-

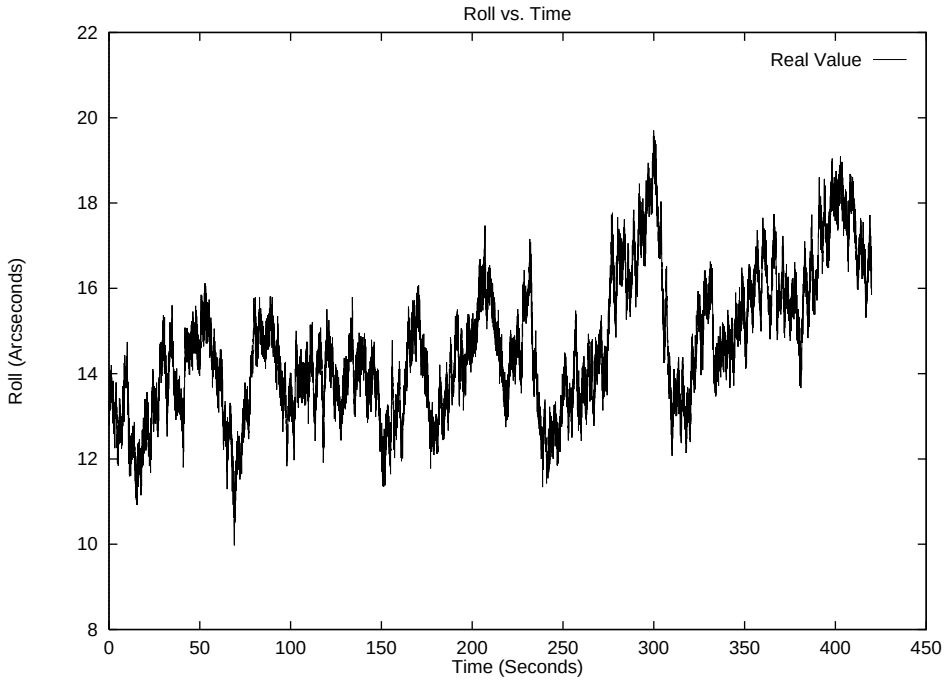

Figure 43: Accuracy and Knowledge Simulation

cator (SOM) projection associated with this orbit path is defined. The limits imposed by the size of the input are extended by reflecting the original input region in the necessary directions throughout this SOM map. The smooth transition of the ground surface is provided for by flipping the images and DEM values at the boundaries, as shown below:

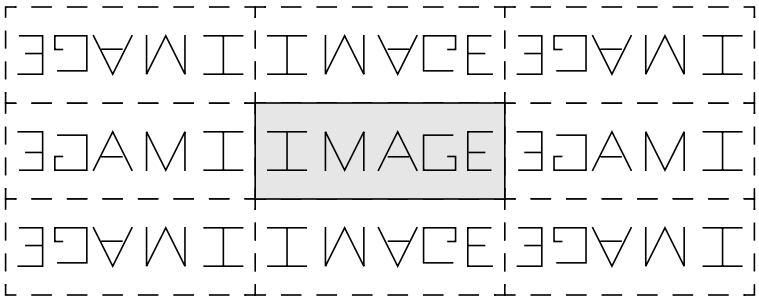

8.3.1.2 Use of the simulated orbit

The orbit simulation is described in the previous section. At each time interval of 40.8 msec, the spacecraft navigation and attitude data are used to compute the intercept of each camera's bore-sight with the Earth at sea level, which will be the center of the MISR swath once the spacecraft position and associated swath center (i.e., the beginning and end of a ray cast from a camera to the surface) are known they are transformed to geocentric cartesian coordinates (GCC). Based on

these coordinates, another coordinate system, the local renderer (LR), will be defined, which is used for implementation purposes. It has the following characteristics: The positive z-axis points from the Earth's center to the spacecraft; the positive x-axis passes through the swath center and is perpendicular to the z-axis; and the positive y-axis completes the right-handed coordinate system. The relationship between these coordinate systems is shown below in Figure 44.

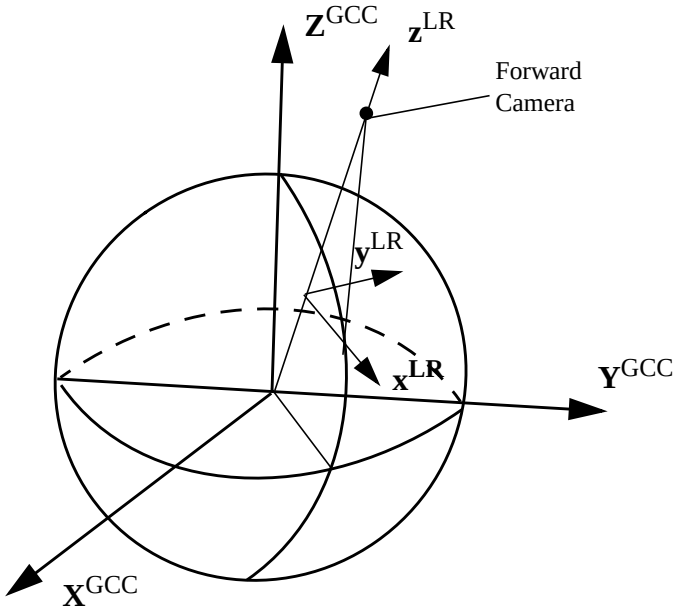

Figure 44: Relation between the GCC and LR system

During its processing the rendering code will need to know if points along a ray are above or below the DEM of the surface within a predefined tolerance. The check is performed in the following manner: The LR coordinates of each point are transformed to GCC and elevation. The GCC is transformed to the SOM projection. Next, the SOM value is propagated through the original image. Finally, the SOM is transformed to UTM allowing the DEM or radiance to be read from the original image.

Using exact formulas for these coordinate transformations would provide the best accuracy. Such an approach would be prohibitively time consuming. Therefore, the algorithm makes use of the following two approximate functions: One which takes coordinates for the LR directly to the SOM projection and associated elevation, and a second which takes coordinates from SOM and computes directly the corresponding position in the input files. Both functions are linear, requiring less computation. In addition sufficient accuracy is preserved (i.e., better than 15 m) by evaluating the pair of functions for regions no larger than 25 km square. There is a different pair of functions used for each of these regions making up the swath. Applying such a method instead of exact coordinate transformations has significantly decreased MISRSIM processing (i.e., 4-5 times) without degradation of the needed accuracy.

8.3.1.3 MISRSIM Rendering Algorithm

The following is a high level description of the MISRSIM rendering algorithm. Certain of these operations involve methods of optimization described in detail in the next section.

For a given camera, the following steps are performed:

- **For each** orbit position, loop over the following steps:
  - Calculate position of camera in GCC.
  - Calculate position of swath center in GCC.
  - Construct matrices for transformation from camera position to surface intercept in LR.
  - **For each** pixel (or subpixel) in a camera, loop over the following steps:
    - Construct ray vectors for each camera pixel (and subpixel) in LR.
    - Obtain initial range along ray.
    - Step along ray until the DEM is intersected.
    - Calculate ground spread of the intersection point.
    - Retrieve the output radiance for the pixel (or subpixel).
  - **End loop**.
  - If subpixeling is used, sum the radiances corresponding to an output camera pixel.
  - Save the range of the intersection to use for the initial range estimate of the next line.
- **End loop**.

8.3.2 MISRSIM rendering optimizations

8.3.2.1 Initial Range Calculation

Ray casting is a simple algorithm which can be optimized only in a few ways. Either the time required to step along a ray must be reduced, or the number of steps needed to intersect the surface must be reduced. The latter can be exploited by selecting a good starting point. The idea for doing this is shown in Figure 45. As shown, the ray A is parallel to ray B. This means that B will go at least as “far” as A. In other words, the distance from the intersection of B with the surface to the current orbit position, projected to the LR xy-plane, is at least the projected distance from the intersection of A to the current orbit position. That is, $\|I_B - O_B\|_{xy} \geq \|I_A - O_B\|_{xy}$. The starting point S_B is chosen such that $\|S_B - O_B\|_{xy} = \|I_A - O_B\|_{xy}$.

In reality, there is not a ray at the previous orbit position that is exactly parallel to the current ray. But there are some rays that are close to parallel. The following was used for pixel p, orbit position n, to calculate $\|S_{p,n} - O_n\|_{xy}$:

$$\min(\|I_{p,n-1} - O_n\|_{xy}, \|I_{p+1,n-1} - O_n\|_{xy}, \|I_{p-1,n} - O_B\|_{xy})$$

This works well in practice; a typical ray needs only one or two steps past the starting point to

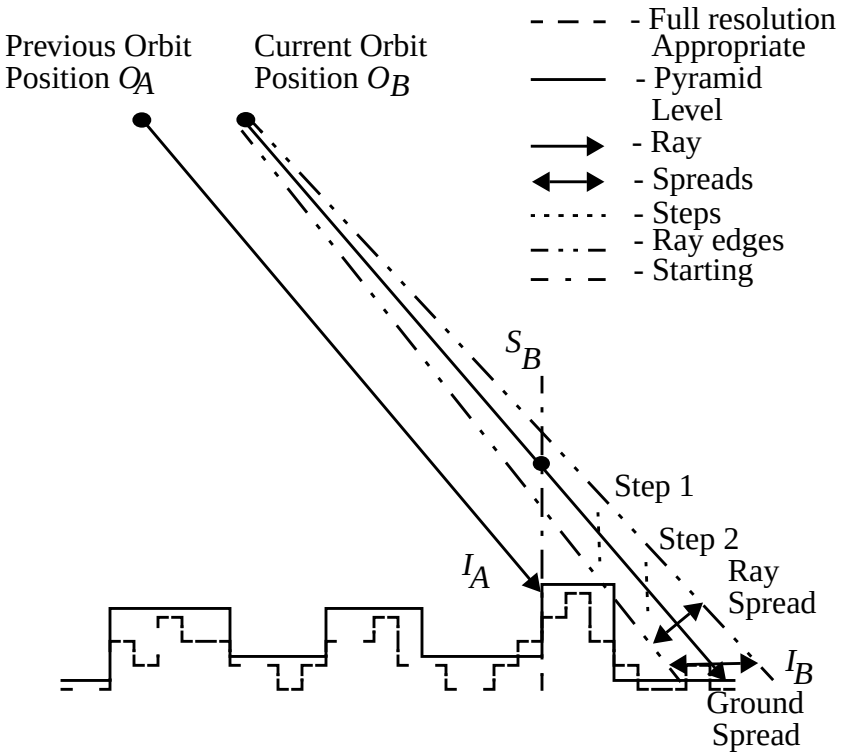

Figure 45: Ray casting

intersect the surface.

Note that this initial range calculation requires that the pixel ray intersections be calculated in a particular order. For aft looking cameras, this requires the orbit to be incremented backwards (i.e., starting with the last orbit position). In addition, pixels 1 and 1504, as well as the entire first line of pixels, cannot use this initial guess, because the intersection of surrounding pixels is not available. Instead, the initial range is determined by finding the intersection of the ray with a plane at the maximum elevation (determined previously for the particular DEM used).

8.3.2.2 Image Pyramids

An image pyramid is built as follows: Starting with an image described by I_1 with $m \times n$ pixels, a coarser description of the image, I_2, with $m/2 \times n/2$ pixels is made. This can be performed in a number of ways: e.g., straight averaging or convolution with a Gaussian and then resampling. Additional images (I_3, I_4, etc.) are built in the same way. The set $(I_1, I_2, \ldots, I_n)$ is referred to as a *n* level image pyramid. I_1 is referred to as level 1 of the pyramid, I_2 as level 2, etc.

Image pyramids are made use of in MISRSIM in two ways. In the algorithm described above, the output radiance is found by averaging over pixels, but instead of doing this explicitly, an image pyramid which contains this averaging can be used. To average over a spread *S*, the radiance value

at the pyramid level where the pixel size is *S* is used. Generally, there will be no pyramid level with a pixel size exactly *S*. Therefore, interpolation is performed between the two closest levels. The second way that image pyramids are utilized is in speeding up the calculation of the intersection of a ray with the DEM by reducing the number of steps. If the spread of a ray on the ground is 250 meters, then the output is not sensitive to features that are 10 meters in size. There is no reason that the intersection calculation needs to be more accurate than the order of the spread. A coarser DEM is then made use of when performing the intersection calculation. Because the coarser DEM has fewer pixels, the computation is reduced.

Note that the spread of a ray on the ground is not known until after the intersection is found, at which point, it is too late to use in the intersection calculation. However, a lower bound is the spread of a ray for a surface normal to the direction of the ray (see Figure 45). This spread, called the ray spread (as opposed to the ground spread), is what is used in the intersection calculation.

8.3.3 Validation of simulated data

Two methods have been used to validate the simulated data. First, images covering the same area from pairs of viewing angles were examined in a stereo viewer. Visually the topography was found to be registered with the features in the images. Second, features were identified in the simulated images, and the image coordinates of those features for all nine camera were measured. Those image coordinates provided the means to define the exterior orientation of the cameras by accessing the navigation data from the orbit program. Then, the ground coordinates of the particular feature were computed via Least-Squares adjustment with a mathematical model based on the photogrammetric collinearity condition. The differences between computed ground coordinates and the ground coordinates from the original input were examined. The resultant RMS errors (82 m horizontal) were expected due to the accuracy of the manual monoscopic measurement of the image coordinates. The conclusion is that there are no significant errors introduced by the algorithm.

8.4 TEST PROCEDURES

8.4.1 Introduction

The tests described here will focus on the validation of the code which implements georectification algorithm. The approach is first to test segments of the code which mirror certain tasks relatively independent of the overall process. These segments are the Image Point Intersection function and Image Matching function, and they will be tested individually.

Other aspects of the georectification algorithm like the transformation and resampling functions can be tested only as part of the entire process. The entire process will be tested in two modes. First, with an ideal input dataset which consists of new imagery identical to the ROI imagery and no errors in the navigation and attitude data, the investigation will focus on proper implementation of the proposed algorithm. The second mode includes realistic MISR images geometrically different than ROI and various cases of the simulated orbit. These tests attempt to validate performance

of the algorithm in regards to the accurate requirements, given our assumptions about errors in the input data (i.e., navigation and attitude data).

The test environment associated with each test consists of: a) input data, b) intermediate data, c) output data, and d) and specialized test software. The ERDAS “Imagine” GIS and image processing tool will be used extensively during testing. Further details an the specific test environments, test objectives and procedures are given in the following sections.

8.4.2 Image Point Intersection Segment

8.4.2.1 Test Goals

The function to be tested here is a backward projection from the ground to image space. For details see §4.3.4.

8.4.2.2 Test Environment

Input data sets

- Image file of the selected region.
- Spacecraft position and attitude data for the piece of the orbit passing over selected region including the best, the worst and the nominal case of the orbit data.
- AGP file of the same region.

Intermediate data sets

- Subset of 15-20 points from the AGP file.
- Modified image file. About 15-20 well-distributed synthetic targets should be placed into the original image file. Pixel values of the original image should be altered so that white cross targets appear in the simulated MISR image.

Output data

- A list of the image coordinates corresponding to the 15-20 points from the AGP file.
- Two Projection Parameters files.

Test software

- ERDAS “Imagine” applications.
- Software to modify the image file (place the targets).
- IPI driver to do “ipi” only on selected points with different user inputs.
- IPI driver to do “ipi” on all SOM grid points.
- Software to numerically compare results from the two Projection Parameter files “ppstat”.

8.4.2.3 Objectives and Procedures

Objective 1. Given the ground coordinates of a point and an initial guess of the line in the MISR image where that point is observed, this segment must compute accurate image coordinates of the given ground point.

Procedure A:
1a. Read the AGP file and select 15-20 points inside the region corresponding to the “Mexico” image.
2a. Place the white cross targets into the original image file. Use the points from the previous step as the target locations.
3a. Run MISRSIM.
4a. Run the IPI. Read the “actual” orbit data. Use the coordinates of the 15-20 points selected in step 1a as the input. Place the image coordinates of those points in a output file “ipi.list”.
5a. Display simulated MISR image. Superimpose 15-20 symbols representing the points selected in the step 1a. Use the coordinates from the “ipi.list” as the locations of the symbols.
6a. Visually investigate the locations of the each superimposed symbol with regard to the white cross targets. They should exactly overlay with the centers of the target. This will be a test of absolute accuracy. The size of the MISR pixel and the internal accuracy of the MISR-SIM are limiting factors in this test. Therefore, in procedure B we will test the relative accuracy strength of the IPI segment.
7a. Run “genpp” and produce Projection Parameters file I. Run the IPI on the entire set of the SOM grid points (e.g. from the AGP file) and produce Projection Parameters file II. Numerically compare results with the results between Projection Parameters file I and II.

Objective 2. This segment must produce image coordinate which will reflect relatively small differences (e.g. 30m) in the ground coordinates of a point.

Procedure B:
1b. Run the IPI five times changing the coordinates of the selected input points by 30m in the X and Y directions each time.
2b. Display symbols representing selected points using image coordinates from five different “ipi.list” files produced in the step 1b. Assign the different colors to the points from different “ipi.list” files. Differences in the image locations of the symbols corresponding to the same point should be proportional to the offsets introduced in the step 1b. These differences should be observed visually and numerically.

Objective 3. This segment must produce accurate image coordinates given various ranges of initial guesses.

Procedure C:
1c. Repeat 4a, 5a, and 6a several times with changing initial line guess in increments of 1000.

The output file “ipi.list” should be same unless there is a message that the initial guess is too far out.
This will test limits of the initial guess.

8.4.3 Image Matching (IM) test set

8.4.3.1 Test Goals

This test set involves the determination of the accuracy of locations of conjugate points in the new image given locations of those points in the reference image.

8.4.3.2 Test Environment

Input data

- Simulated MISR images of a couple of different land surface scenes.

Intermediate data

- “im.list” file. Set of 30 points (image line/sample coordinates) uniformly distributed throughout MISR image.
- “im.list_offset”. Offsets (3 -4 pixels) added to the points in the “im.list”

Output data

- “im.list_correct”. Corrected image coordinates excluding those which are rejected by matching.

Test software

- ERDAS “Imagine” application.
- Driver to do image matching testing only.

8.4.3.3 Objectives and Procedures

Objective 1. Given the position of a point in the reference image and an initial guess for the location of that point in the new image this should compute an accurate location of the same point in the new image.

Procedure A:
1a. Make the “im.list” and “im.list_offsets” files.
2a. Display MISR “Mexico” image in two separate windows. Display points from “im.list” in window I and points from “im.list_offset” in window II.

3a. Run IM program. Generate “im.list_correct” file. Using these coordinates display points in the window II. They should be located at the identical position as the corresponding points in the window I. Otherwise they should not be displayed at all to indicate unreliable match.
4a. Repeat 1a, 2a, and 3a for the Mexico regions with significantly different viewing geometry (e.g. the MISR Mexico images produced using different orbit files).

Objective 2. In the case that there is not enough image information to do matching this test set should respond appropriately indicating an unreliable match.

Procedure B:
1b. Observe the output from procedure A. Search for the points which are not displayed with their corrected location. Examine the image content in the vicinity of these points.

Objective 3. It must satisfy objective 1 for a user controlled range of the initial guesses.

Procedure C:
1c. Repeat 2a, 3a, and 4a changing the magnitude of the offset used to make file “im.list_offset” several times and observe the display in window II. This will test objective 3.

Objective 4. The performance of this test set should be the same (in general) regardless of the different data sets (i.e. land surface scenes) used as the input to the image matching. However, sufficient image texture is still required.

Procedure D:
1d. Repeat procedure A, B and C for different data set.

8.4.4 Grid/Subgrid Centers (G/SC) selection and registration test set

8.4.4.1 Test Goals

The purpose of this test is to demonstrate that the main georectification software (i.e GP_main) works correctly in the best possible circumstances. We supply input data that should allow GP_main to produce output that exactly matches the expected results. Any deviation from the expected results is due to approximations done in GP_main, or errors in the software.

8.4.4.2 Test Environment

Input data

- Simulated MISR image over a selected region. For this test, reference and new image will be the same.
- Ancillary Geographic Product associated with the selected region.

- Spacecraft navigation and attitude data (orbit data) associated with the selected region. In this test we use both the “actual” and “measured” (see §8.2).
- Projection Parameters file associated with reference imagery.

Intermediate data

- none

Output data

- Output from GP_main. For testing purposes, the output from the GP_main is not only geo-rectified image but also a Projection Parameters file associated with the new MISR image.
- Secondary output files: difference file, histogram file, flag file and grid description file.

Test software

- ERDAS “imagine” application.
- Software to numerically compare results from the two Projection Parameter files “ppstat”.
- Software to import raster files into ERDAS, “rastoimg”.
- Software to produce secondary output files.

8.4.4.3 Objectives and Procedures

Objective 1. Under the best possible circumstances, GP_main should generate results that exactly match the expected result. This is mainly an integration test: can we get data through the system without it breaking? Does GP_main mangle the data that it sent through the system?

Procedure A1:

1a. Use the “actual” orbit as the input, run GP_main (using clear.cloud mask). Run ppstat to compared the resulting projection parameter files to the expected results. Run software to produce secondary output file.

2a. Examine the histogram file. Theoretically there should be no difference between projection parameters in these two files. Examine the distribution of errors by looking at the differences plotted in ERDAS tools. Examine the output flag files and resampled imagery in ERDAS, making a qualitative determination if it looks “right” (e.g, no holes, no artifacts). Examine the grid description file, and look at the distribution of grid points.

Objective 2. This test is only slightly harder than the previous one. Rather than using “perfect” orbit knowledge, we include simulated errors in the navigation data supplied to GP_main. GP_main should be able to completely remove these errors. This adds image matching testing the integration test. Can we get data through system without it breaking? Does image matching cause GP_main to mangle the data?

Procedure B:

1b. Repeat 1a and 2a but use “measured” orbit rather than “actual” orbit. Results should be similar to the results of procedure A.

8.4.5 Standard Processing (STP) test set

8.4.5.1 Test Goals

Procedurally this test is very similar to one described above. However, the overall objective and character of input data is different. The goal is to test the performance of the algorithm assuming that realistic errors and conditions are present in the input data (e.g. orbit data). The primary outputs are the georectified image resampled from the new MISR image, along with Projection Parameters file that is associated with the new MISR image. The PP file is necessary in order to globally test spatial geolocation accuracy.

The main objective of the Standard Processing is to produce georectified imagery which conforms to the chosen SOM map grid. The errors in the geolocation of the specific ground features due to the several projection steps involved must be minimized. Also, radiometric errors due to the resampling must be minimized. Particularly, requirements are:

-Geolocation: A particular target must be geolocated to ± 275 m cross-track and ± 550 m along-track (with a goal of ± 275 m) relative to the true geographic position of that target. Confidence level is 95%, or for gaussian statistics, 2σ level.

-Radiometric: The interpolated radiances at the SOM grid centers should equal the value that would have been obtained had an instrument sample directly coincided with that grid point to within $\pm 3\sigma$ (68% confidence).

A full description of the requirements can be found in the reference document [M-5]. Prior to setting the test goals for the standard processing an error analysis of the entire georectification system has to be done.

The error budget for the Georectified product

The L1B2 Georectified product is the result of new to reference image registration and band to band registration. From the aspect of error budget distribution, we will consider three contributions to the total error: 1) error in the reference projection parameters, 3) band-to-band registration error, and 3) new-to-reference image registration error. An analysis used to predict the size of the error associated with the reference imagery and projection parameters is described in the reference document [M-10]. Band-to-band registration error analysis is given in §4.3.6.4. Given the requirements for the geolocation error of the L1B2 Georectified product (i.e 1.0 pixels down-track and 0.5 pixels cross-track, 1σ), and assuming that the total error represents RSS of the contributing errors, we can compute the requirement for the new to reference (red band, only) standard processing registration. The Table 24 presents the error distribution related to the various elements of the Georectified product. The column with the double borders contains the numbers used as

targets during the testing.

Table 24: Georectified product - Error budget

	Requirement for the Georectified product	Error associated with the Reference PP	Error associated with the band to band transform	Allowable error for new to reference registration	
Down-track	1.0	0.9	0.3	0.22	Min
	1.0	0.6	0.3	0.67	Max
Cross-track	0.5	0.35	0.1	0.35	Min
	0.5	0.3	0.1	0.39	Max

8.4.5.2 Test Environment

Input data

- An image template file representing ortho-rectified imagery of the selected region obtained from the source other than MISR (e.g. Landsat).
- Simulated MISR image over a selected region. Two or more shall be selected. For this test reference imagery must be produced with a different orbit file than the new image, so it is geometrically and radiometrically different than the new image.
- Ancillary Geographic Product associated with the selected region.
- Spacecraft navigation and attitude data (orbit data) associated with the selected regions. In this test we use “measured” data (see §8.2). Also, all three cases, worst, nominal and best are to be investigated.
- Projection Parameters file associated with reference imagery.

Intermediate data

- None.

Output data

- Output from GP_main: georectified imagery and Projection Parameters file associated with the new MISR image
- Secondary output files: difference file, histogram file, flag file and grid description file.

Test software

- ERDAS “imagine” application.
- Software to numerically compare results from the two Projection Parameter files “ppstat”.
- Software to import raster files into ERDAS, “rastoimg”.
- Software to produce secondary output files.

8.4.5.3 Objectives and Procedures

Objective 1. Geometric accuracy should satisfy requirements.

Procedure A:

1a. For different cases representing combinations of the various orbits regions and cameras run GP_main. Run ppstat to compare the resulting projection parameter files to the expected results.

2a. Produce secondary files. Examine the histogram file, and insure that 95% confidence error is within tolerance. Examine the distribution of errors by looking at the differences plotted in ERDAS tools. Examine the output flag files and resampled imagery in ERDAS, making a qualitative determination if it looks “right” (e.g, no holes, no artifacts). Examine the grid description file, and look at the distribution of grid points.

Objective 2. Radiometric accuracy should satisfy requirements.

Procedure B:

1b. Use the differences between output from the georectification software “GP_main”” and “image template” to estimate radiometric error.

9.0 ASSUMPTIONS AND LIMITATIONS

9.1 Assumptions

(1) It is assumed that the specific implementation of certain algorithms described in this document will involve calls to the SDP Toolkit, although at this time this is not explicitly shown. It is also assumed that, wherever possible, inherited code will be used.

(2) It is assumed that a space-based map projection will be used for the MISR image products. The algorithms described in this document assume a Space-Oblique Mercator (SOM) projection.

(3) In the pre-flight activities, a SOM grid is precalculated based upon the predicted orbit for the EOS-AM spacecraft. If the actual orbit varies greatly from this, the SOM grid will be recalculated after launch. The plans for the in-flight activities account for this possibility.

(4) During the in-flight geometric calibration phase, multiple orbits may be combined to construct MISR reference orbit imagery in order to maximize the cloud-free coverage. It is assumed that it will not be possible to produce individual orbits which are completely cloud-free during the period allocated for the in-flight activities. The algorithms for standard processing take this into account.

(5) It is assumed that World Geodetic System 1984 (WGS84) ellipsoid will be used as a reference.

(6) It is assumed that a global DEM of at least 1.1 km horizontal spacing will be available preflight for the creation of the Ancillary Geographic Product (AGP). It is also assumed that a DEM of higher horizontal resolution than MISR imagery (i.e., 100 m) will be available at the MISR SCF for the much of the land surface.

(7) During the preflight activities non-EOS geolocated imagery will be assembled for use during the in-flight geometric calibration. It is assumed that sufficient coverage for the selected orbits will be available. (As a rough estimate, this would amount to approximately 10 scenes per orbit for 10 selected orbits.)

(8) It is assumed that the spacecraft pointing knowledge meets specifications (i.e., 90 arcsec, 3σ, in each axis). If the in-flight performance proves to be better than this, the Level 1B2 processing strategy automatically compensates by performing less image matching.

(9) It is assumed that the geolocation requirements stated in the MISR DSSR will be met, in part, through spacecraft position knowledge, obtained using the TDRSS On-board Navigation System (TONS), of ± 50 m (3σ) or better in each axis.

9.2 Limitations

(1) If a DEM of higher horizontal resolution than MISR imagery (i.e., 100 m) is not available by launch, geolocation and camera-to-camera registration accuracy of Level 1B2 products will be degraded. In addition, there will be an increase in computational load at both the SCF, during the in-flight phase, and at the DAAC, during standard processing. This is due to expanded image matching requirements.

(2) During standard processing of the Level 1B2 surface-projected radiance parameters, image matching is not performed on areas of new MISR images designated as “unclassified” by the cloud detection algorithm or areas of the MISR reference orbit imagery covered by clouds. Therefore, geolocation and camera-to-camera registration accuracy in such areas is determined purely by the accuracy of the supplied spacecraft navigation data.

10.0 REFERENCES

[1] Ackermann, F., Digital Image Correlation: Performance and Potential Application in Photogrammetry, Photogrammetric Record, vol. 11(64), 1984.

[2] Castleman, K. R., Digital Image Processing, Prentice-Hall, Inc., Englewood Cliffs, N. J., 1979

[3] Colwell, R. N., editor, Manual of Remote Sensing, Second Edition, vol. I, American Society of Photogrammetry, Falls Church, Virginia, 1983.

[4] Di Girolamo, L. and Davies R., The Image Navigation Cloud Mask for the Multiangle Imaging Spectroradiometer, Journal of Atmospheric and Oceanic Technology, Vol. 12(6), December 1995.

[5] Diner, D. J., Atmospheric Refraction, Interoffice Memorandum, MISR DFM #212, 1992.

[6] Fogel, D. N. and Tinney, L. R., “Image Registration Using Multiquadric Functions”, Final Project Report, Remote Sensing Research Unit, Dept. of Geography, University of California, Santa Barbara, May 1994.

[7] T.J. Ford, “Navigations Input to Pointing/Orbit Study”, EOS-GN&C-280, 6/22/93.

[8] Golub, G. and Van Loan, C., Matrix Computations Second Edition, John Hopkins University Press, Baltimore and London, 1989.

[9] Gruen, A. W. and Baltsavias, E. P., High Precision Image Matching for Digital Terrain Model Generation, International Archives of Photogrammetry, vol. 25, no. 3, 1986.

[10] Hannah, M. J., Digital Stereo Image Matching Techniques, ISPRS 16th Congress, Commission III, Kyoto, Japan, 1988.

[11] J.R. Herberg, “Navigation System Real-Time Interface Algorithm”, EOS-DN-GN&C-053, 4/26/93.

[12] Herrick, S,. Astrodynamics, Van Nostrand Reinhold, New York, 1971.

[13] Forstner, W., On the Geometric Precision of Digital Correlation, ISPRS Int. Arch. of Photogrammetry, vol. XXIV, Commission III, Helsinki, 1980.

[14] Jovanovic, V., L1 Geometric Calibration ATB” , JPL D-13399, DRAFT January 29, 1996.

[15] Kaula, W., Theory of Satellite Geodesy: Application of Satellites to Geodesy, Blaisdell, 1966.

[16] Korechoff, R.P., “Analysis of MISR Camera Geolocation and Registration Requirements,” Interoffice Memorandum, MISR DFM #207 and OSA DFM #93-27, 1993.

[17] _____, “Analysis of third breadboard CAT test,” Interoffice Memorandum, MISR DFM #368, March 2, 1994.

[18] _____, “CAT algorithm description,” Interoffice Memorandum, MISR DFM #373, March 7, 1994.

[19] _____, “MISR camera model,” Interoffice Memorandum, MISR DFM #392, April 8, 1994.

[20] Leick, A., GPS Satellite Surveying, John Wiley & Sons, New York, 1990.

[21] Lewicki, S. A., Smyth, M. M., Jovanovic, V. M., and Hansen, E. G., “A Simulation of EOS MISR Data and Geometric Processing for the Prototyping of the MISR Ground Data System”, IGARSS Proceedings, vol (3), 1994.

[22] NOAA-EPA Global Ecosystems Database Project: Global Ecosystem Database Version 1.0 User’s Guide, Documentaion, Reprints, and Digital Data on CD-ROM. U.S. DOC/NOAA National Geophysical Data Center, Boulder, CO. 1992

[23] Mikhail, E. M., Observations and Least Square, Harper & Row, New York, 1976.

[24] Moffit, F. H. and Mikhail, E. M., Photogrammetry, Third Edition, Harper & Row, New York, 1980.

[25] P. Mookerjee, “EOS-AM Attitude Determination”, *General Electric Astro Space Division, Memo No.: EOS-DN-GNC-034*, April 20, 1992

[26] Otto, G. P. and Chau, T. K. W., A “Region-Growing” Algorithm for Matching of Terrain Images, Image and Vision Computing, vol (7), 1989.

[27] Paderes, F. C., Mikhail, E. M., and Fagerman, J. A., Batch and On-Line Evaluation of Stereo Spot Imagery, ASPRS Proceedings, vol. (3), 1989.

[28] Paderes, F. C., and Mikhail, E. M., Registration/Rectification of Remotely Sensed Data, Final Technical Report for NASA contract number 9-16664, School of Civil Engineering, Purdue University, West Lafayette, Indiana, April 1986.

[29] Page, C. C., “Computer Solution and Perturbation Analysis of Generalized Least Squares Problems”, Math. Comp. 33, 171-84, 1979.

[30] Page, C. C., “Fast Numerically Stable Computations for Generalized Linear Least Squares Problems”, SIAM J. Num. Anal. 16, 165-71

[31] Paul, M. K., A Note on the Computation of Geodetic (Cartesian) Coordinates, Bull. Geod. 108, p. 135, 1973.

[32] Pertl, A., Digital Image Correlation with the Analytical Plotter Planicomp C 100, ISPRS 15th Congress, Commission III, Rio de Janeiro, 1984.

[33] Press, W. H. et. al., Numerical Recipes in C: The Art of Scientific Computing, Cambridge University Press, Cambridge, 1988.

[34] Seidelmann, K. P., editor, Explanatory Supplement to the Astronomical Almanac, University Science Books, Mill Valley, California, 1992

[35] Snyder, J. P., Map Projection - A Working Manual, United States Geological Survey Professional Paper 1395, U. S. Government Printing Office, Washington, 1987.

[36] Stanfill, D.F., “Using Image Pyramids for the Visualization of Large Terrain Data Sets.” International Journal of Imaging Systems and Technology, Vol. 3 (1991): 157-166.

[37] Vanicek P. and Krakiwsky E. J., Geodesy: The Concept, Elsevier Science Publishers B. V., The Netherlands, 1986.

[38] Wertz, J., ed., Spacecraft Attitude Determination and Control, D. Reidel Publishing Company, Boston, 1978.

[39] EOS-AM Spacecraft Pointing Study Spacecraft PDR Update, Executive Summary”, 8/31/93.

APPENDIX A: COORDINATE TRANSFORMATIONS

A.1 DEFINITIONS OF COORDINATE SYSTEMS

A.1.1 Detector Coordinate System

Figure 46 shows the placement of an arbitrary camera focal plane relative to a coordinate system called the detector coordinate system (DCS). The DCS x axis is defined to be perpendicular to the long axis of the detector arrays. The y axis is parallel to the long axis and is positive in the westward direction during a descending pass. The z axis is the cross product of x with y forming a right-handed coordinate system. As shown in Figure 46, the z axis intercepts the focal plane at the center of band 3. The figure also shows that the focal plane is located at z = -f where f is the effective focal length of the particular camera.

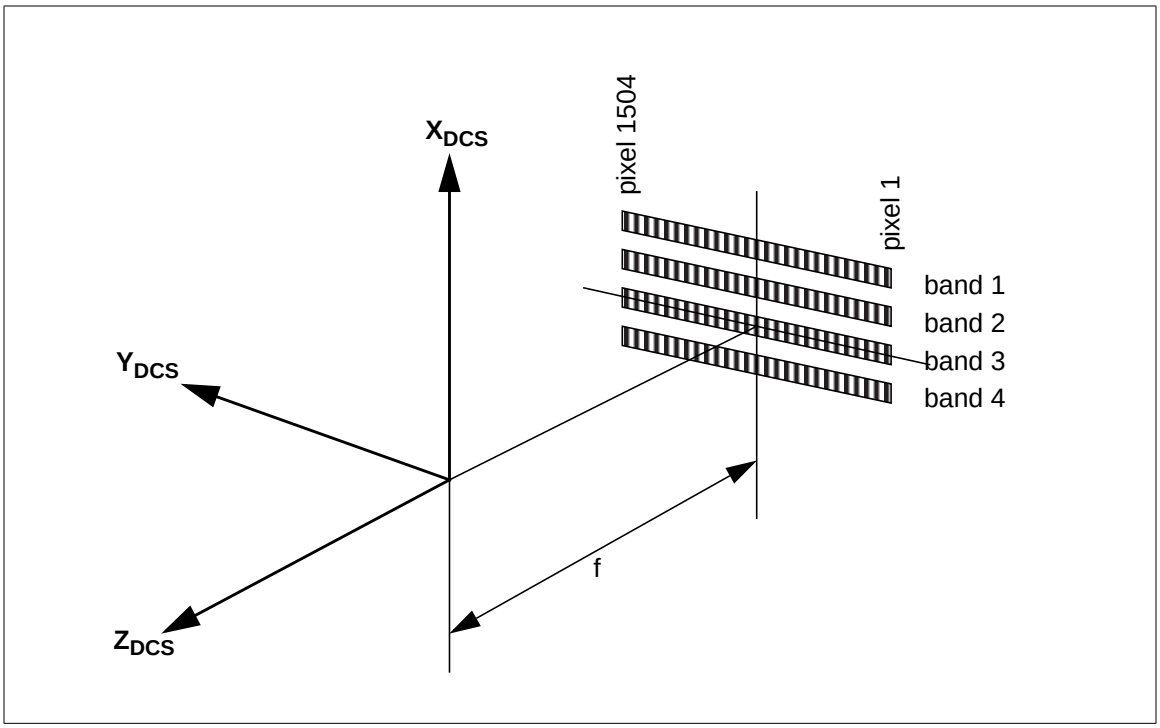

Figure 46: Definition of the Detector Coordinate System

A.1.2 Camera Coordinate System

In the camera coordinate system (CCS), the z axis is the mechanical symmetry axis of the camera barrel. The y axis is parallel to the long symmetry axis of the detector arrays and is positive in the westward direction during a descending pass of the satellite. The x axis is the cross product of the y axis and the z axis forming a right-handed coordinate system. Under ideal circumstances, the CCS is identical with the DCS. Due to fabrication and alignment errors, the DCS and CCS may

differ by small-angle rotations.

Physically, the plane formed by the intersection of the x and y axes is the interface between the camera and the optical bench, where the x axis is defined as passing through the center of the interface flange and the center of the pin and where the y axis is defined as lying in the plane of the locating pads perpendicular to the x axis. The z axis is then perpendicular to the lens barrel front flange.

A.1.3 Instrument Coordinate System

The instrument coordinate system (ICS) is a right-handed instrument coordinate system fixed relative to the MISR instrument with respect to reference surfaces (optical cubes) whose normals define the coordinate system. The pointing of each camera boresight (barrel mechanical axis) is defined in this coordinate system by two angles as shown in Figure 47. Each axis is nominally aligned with the corresponding axis of the spacecraft coordinate system defined below, and any differences will be the result of instrument mounting errors.

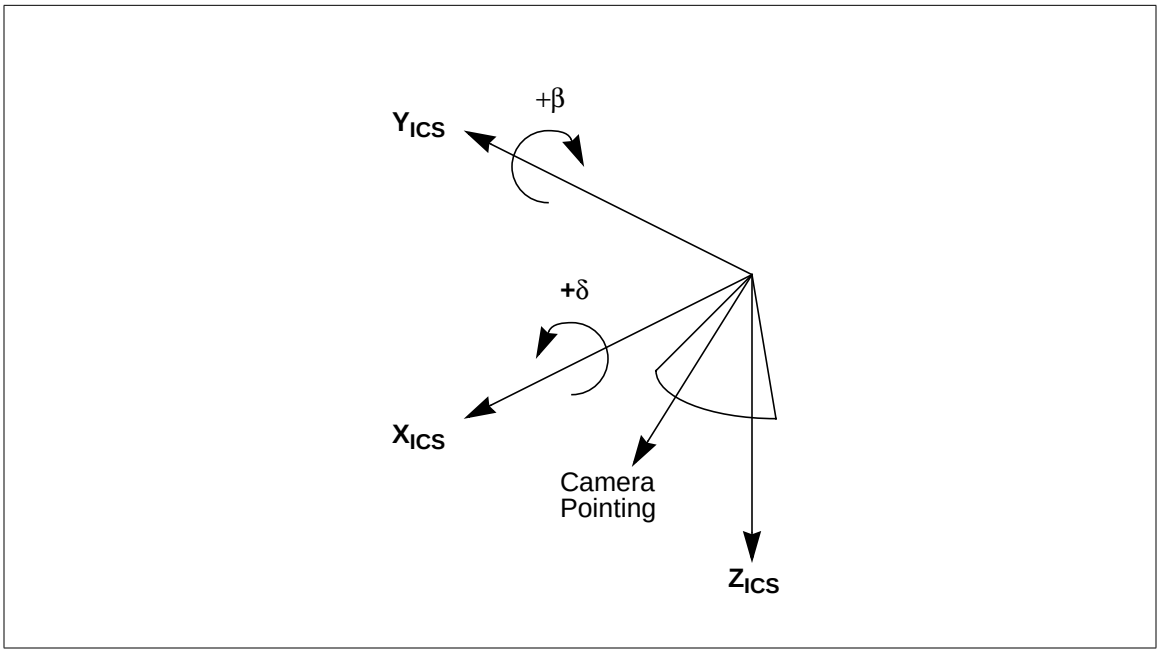

Figure 47: Definition of the Instrument Coordinate System

A.1.4 Spacecraft Coordinate System

The spacecraft coordinate system (SCS) and the ICS are nominally aligned except for a translation of the origin to the EOS spacecraft's center of mass. Misalignments between the ICS and SCS are due to fabrication errors or thermal effects. The SCS axes are fixed in relation to the spacecraft body. The relationship with the orbital coordinate system defined below is reflected through the attitude angles roll, pitch, and yaw. If those angles are all zero the two systems are identical.

A.1.5 Orbital Coordinate System

The orbital coordinate system (OCS) is a right-handed coordinate system with its origin at the spacecraft's center of mass (same as the SCS). The z axis is aligned with the spacecraft-to-Earth pointing vector. The y axis is defined by the cross product of the z axis and the EOS spacecraft velocity vector, and points toward the anti-Sun side of the spacecraft. The x axis is defined by the cross product of the y axis and the z axis. It points in the general direction of the spacecraft velocity vector, but is not necessarily instantaneously aligned with it due to Earth oblateness and eccentricity of the orbit. The rotations which transform the SCS into the OCS are defined by the attitude angles roll, pitch, and yaw.

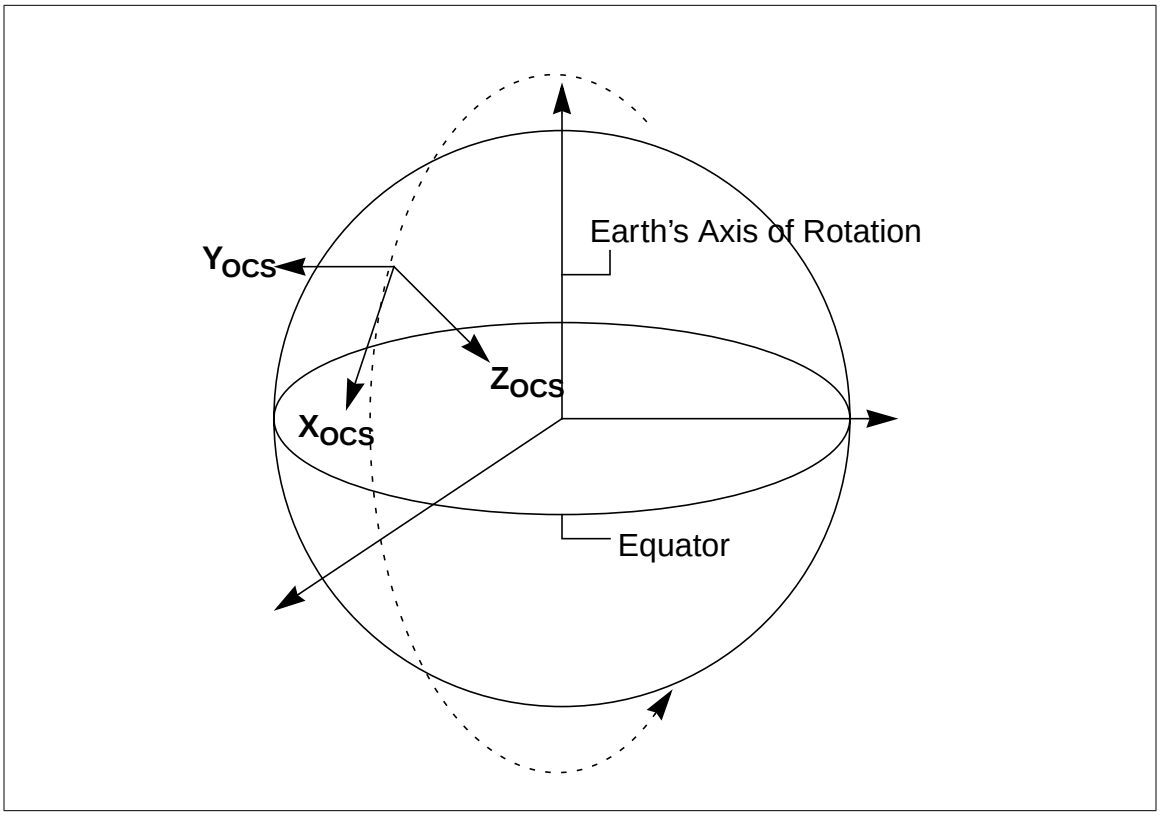

Figure 48: Definition of the Orbital Coordinate System

A.1.6 Geocentric Inertial Coordinate System

The geocentric inertial (GCI) coordinate system is a right-handed coordinate system defined to describe directions in an Earth-centered but not Earth-fixed frame. That is, the axes are defined with respect to directions in space and not with respect to locations on the Earth. The spacecraft position and velocity vectors are referenced to this coordinate system. The positive z axis is parallel to the Earth's rotation axis in the direction of the mean north celestial pole of epoch J2000.0 and the positive x axis points to the mean vernal equinox of epoch J2000.0. The y axis is the cross product of the z axis and the x axis.

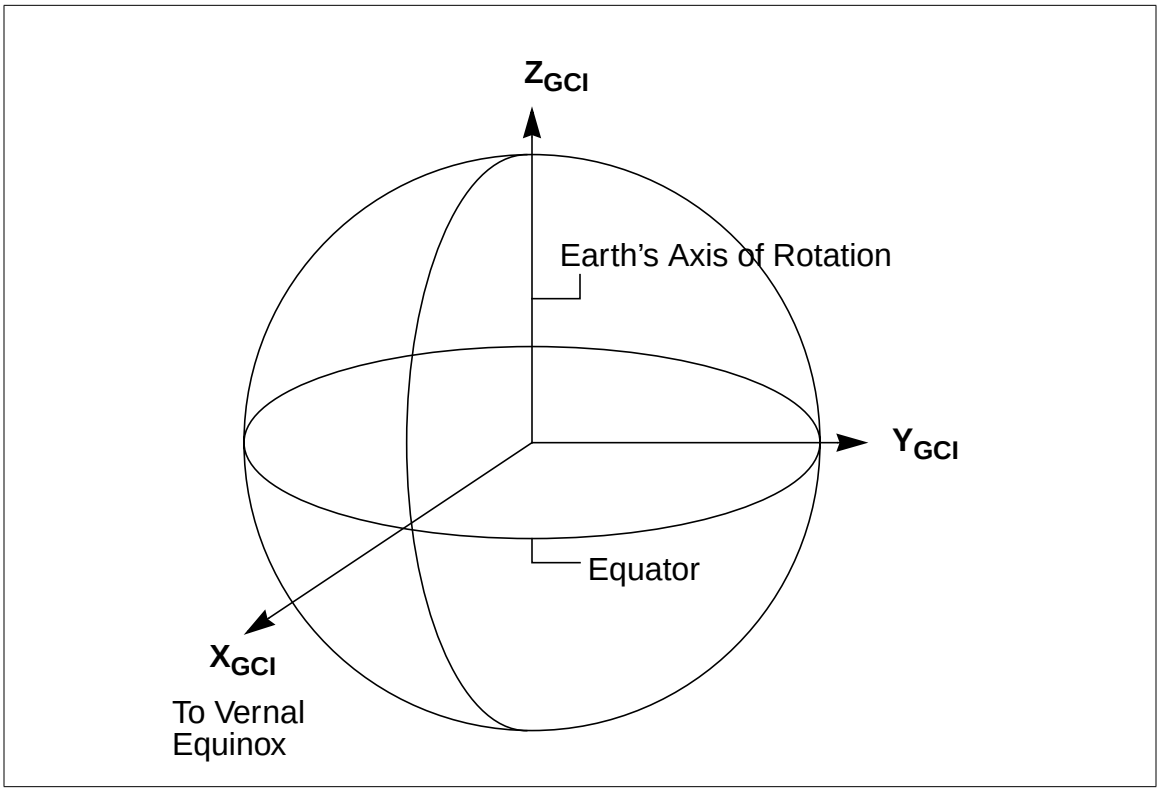

Figure 49: Definition of the Geocentric Inertial Coordinate System

A.1.7 Conventional Terrestrial Reference Coordinate System

The Conventional Terrestrial Reference (CTR) coordinate system is Earth fixed with its origin at the center of mass of the Earth. The coordinate system has been defined by the Bureau International de l'Heure (BIH), and it is the same as the U. S. Department of Defense World Geodetic System 1984 (WGS84) geocentric reference system. This coordinate system is defined in detail in reference [20]. The transformation from GCI to CTR accounts for precession, nutation, Earth rotation, and polar motion.

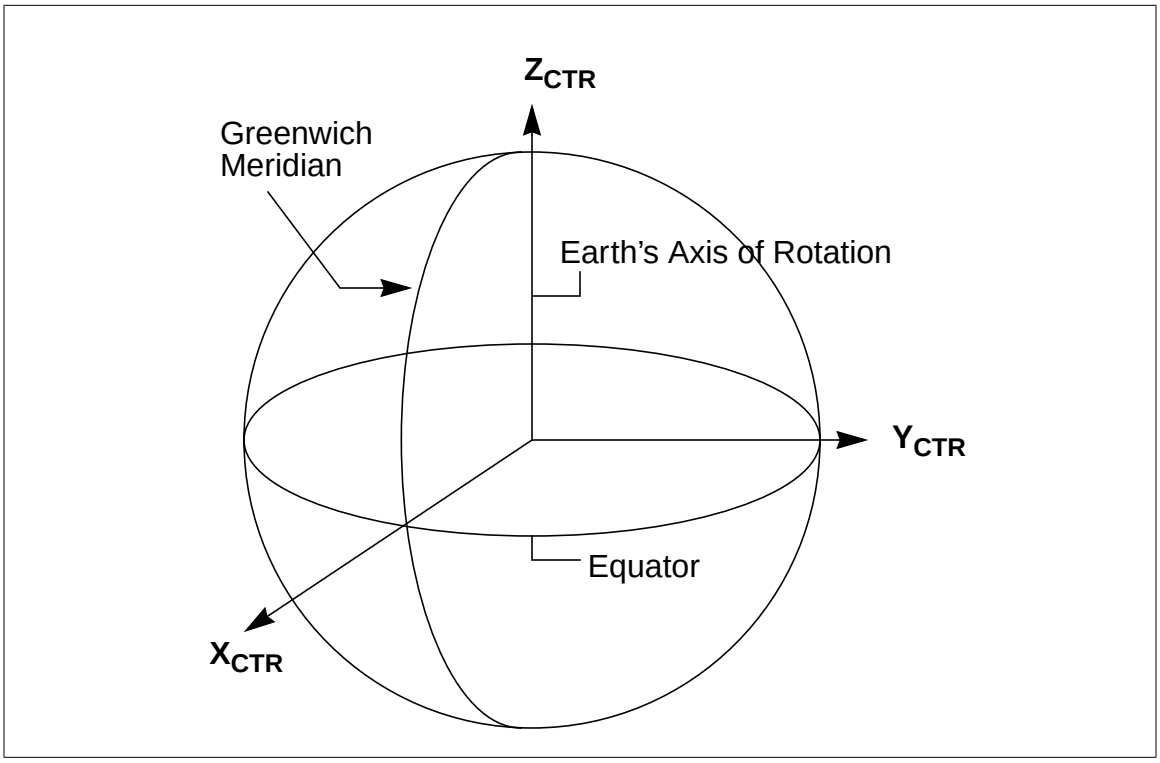

Figure 50:

A.1.8 Geodetic Coordinate System

The geodetic coordinate system is based on the WGS84 reference ellipsoid with coordinates expressed in latitude, longitude, and height above the reference Earth ellipsoid. Latitude and longitude are respectively the angle between the ellipsoid normal and its projection onto the equator, and the angle between the local meridian and Greenwich meridian, respectively.

A.2 DESCRIPTION OF COORDINATE TRANSFORMATIONS

A.2.1 DCS to CCS (Detector to Camera)

Under ideal circumstances, the CCS is identical with the DCS. Due to fabrication and alignment errors, the DCS and CCS may differ by small-angle rotations. The transformation between DCS and CCS given by:

$$T_{cd} = \begin{bmatrix} 1 & -\varepsilon & \psi \\ \varepsilon & 1 & -\theta \\ -\psi & \theta & 1 \end{bmatrix} \tag{71}$$

The angles θ, ψ, and ε are rotations around the DCS x, y, and z axes respectively. The transformation assumes that the axes are fixed. The order of rotation does not matter because the angles are small. The angle ε accounts for rotations of the detector array around the optical system axis of symmetry. The angles ψ and θ reflect any misalignment between the boresights of the optics and the barrel.

A.2.2 CCS to ICS (Camera to Instrument)

Each camera boresight is defined with respect to the MISR instrument by two angles, δ and β, which are positive rotations around the instrument x and y axes respectively. The transformation between CCS and ICS is given in Eq. (72). Equation (72) is obtained by first applying a rotation of δ around the x-axis and then a rotation of β around the y-axis. The MISR IFR lists the nominal values of δ and β for each camera.

$$T_{ic} = \begin{bmatrix} \cos\beta & \sin\beta\sin\delta & \sin\beta\cos\delta \\ 0 & \cos\delta & -\sin\delta \\ -\sin\beta & \cos\beta\sin\delta & \cos\beta\cos\delta \end{bmatrix} \tag{72}$$

A.2.3 ICS to SCS (Instrument to Spacecraft)

Nominally ICS and SCS are aligned. However, due to possible instrument mounting errors there may be some discrepancies between these two systems. The discrepancies will be found during pre-flight camera calibration and will be reported as the roll, pitch and yaw angles. With appropriate notation for those angles the transformation matrix from the instrument to the spacecraft T_{si} is defined in the same way as the transformation T_{os} shown in (73). The rotation angles will be defined as ω_x, ω_y, ω_z respectively.

A.2.4 SCS to OCS (Spacecraft to Orbital)

The spacecraft to orbital transformation is used to rotate a vector in SCS to OCS in order to account for attitude deviations. Explicitly if the Ω, Ψ and K are roll, pitch and yaw respectively, and the rotations are performed in that order, then:

$$T_{os} = \begin{bmatrix} \cos\Psi\cos K & \sin\Omega\sin\Psi\cos K + \cos\Omega\sin K & -\cos\Omega\sin\Psi\cos K + \sin\Omega\cos K \\ -\cos\Psi\sin K & -\sin\Omega\sin\Psi\sin K + \cos\Omega\cos K & \cos\Omega\sin\Psi\sin K + \sin\Omega\cos K \\ \sin\Psi & -\sin\Omega\cos\Psi & \cos\Omega\cos\Psi \end{bmatrix} \tag{73}$$

A.2.5 OCS to GCI or CTR (Orbital to Geocentric)

The transformation matrix to convert from OCS to either geocentric coordinate system (GCI or CTR) can be constructed by using the spacecraft position vector $\boldsymbol{p}$ and velocity vector $\boldsymbol{v}$. By the

definition of the orbital coordinate system we can express its axes in either geocentric coordinate system as follows

$$\begin{aligned} \hat{\boldsymbol{z}} &= \frac{-\boldsymbol{p}}{\|\boldsymbol{p}\|} \\ \hat{\boldsymbol{y}} &= \frac{\hat{\boldsymbol{z}} \times \boldsymbol{v}}{\|\hat{\boldsymbol{z}} \times \boldsymbol{v}\|} \\ \hat{\boldsymbol{x}} &= \hat{\boldsymbol{y}} \times \hat{\boldsymbol{z}} \end{aligned} \tag{74}$$

Then the transformation matrix is:

$$T_{co} = \left[\hat{\boldsymbol{x}}\ \hat{\boldsymbol{y}}\ \hat{\boldsymbol{z}}\right] \tag{75}$$

This transformation will be between the Orbital Coordinate System and GCI if the vectors ***p*** and ***v*** are given relative to GCI. Likewise, if ***p*** and ***v*** are given relative to the CTR the transformation will be between Orbital and CTR systems.

A.2.6 GCI to CTR

The transformation from GCI to CTR coordinates is a time varying rotation due primarily to Earth rotation but also contains more slowing varying terms for precession, nutation, and polar motion. The GCI to CTR rotation matrix T_{cg} can be expressed as a composite of these transformations. Each transformation is described in detail in [20].

A.2.7 Geodetic Coordinates

The relationship between CTR and geodetic coordinates can be expressed in the direct form:

$$\begin{aligned} X &= (N+h)\cos(lat)\cos(lon) \\ Y &= (N+h)\cos(lat)\sin(lon) \\ Z &= (N(1-\varepsilon^2)+h)\sin(lat) \end{aligned} \tag{76}$$

where:

X,Y,Z are the CTR coordinates.

lat,lon,h are the geodetic coordinates.

N is the ellipsoid radius of curvature in the prime vertical.

ε is the ellipsoid eccentricity.

The inverse operation can be solved by iteration or in closed form (see [37], p. 325).

A.3 MAP PROJECTIONS

A.3.1 Space-Oblique Mercator (SOM)

The SOM system is a space-based map projection, based on the Oblique Mercator projection, where the reference meridian nominally follows the spacecraft ground track. It provides a mapping from latitude/longitude to a coordinate system that is approximately aligned with the MISR swath.

For the transformation to the SOM map projection, which is quite complex, the reader is referred to reference [35]. This transformation occurs during in-flight calibration to establish the projection parameters which take the reference orbit imagery to the predefined SOM grid.